Self-organization of composite model catalysts:

vanadium and nickel oxides on Rh(111)

Von der Naturwissenschaftlichen Fakultät

der Gottfried Willhelm Leibniz Universität Hannover

zur Erlangung des Grades

Doktor der Naturwissenschaften

Dr. rer. nat.

genehmigte Dissertation

von

Dipl.-Chem. Florian Lovis

geboren am 27.09.1978 in Bremen

2011

Referent: Prof. Dr. Ronald Imbihl

Koreferent: Prof. Dr. Herbert Pfnür

Tag der Promotion: 18.01.2011

Abstract

Two "inverted" model catalyst systems (inverted with respect to the usual structure of a supported catalyst with metal particles on an oxide support) were studied: $Rh(111)/VO_x$ and $Rh(111)/Ni/NiO$ were exposed to $H_2 + O_2$ reaction conditions at $10^{-7} - 10^{-4}$ mbar and $500 - 700°C$. The reaction dynamics were followed *in situ* by photoemission electron microscopy (PEEM) and low energy electron microscopy (LEEM). Additional chemical and structural information was gathered employing area-selected x-ray photoelectron spectroscopy (μ-XPS) and low energy electron diffraction (μ-LEED).

For sub-monolayer films of VO_x on $Rh(111)$ one finds several transformations of the catalyst surface via reaction fronts, as the system adapts to changing ratios of the reactant gases. Under reductive conditions, i.e. at high reaction rates, the vanadium oxide condenses into mesoscopic stripe patterns on the $Rh(111)$ surface. The patterns are termed quasi-stationary, since they exhibit coarsening: the length scale grows according to a power-law dependence on time. The initial length scale of the stripe patterns depends on the total pressure via a power law, high pressures generating short length scales. Pattern formation is discussed within the concepts of *reactive phase separation* and *spinodal decomposition*: the main driving forces are presumably the strongly attractive interaction between V and O, and the phase boundary energy which arises at boundary lines between VO_x islands and the bare rhodium surface. Two novel VO_x monolayer structures on $Rh(111)$, exhibiting (2×2) and *split*-(2×2) diffraction patterns, respectively, are reported. The structures appear to be stable exclusively under reaction conditions. The (2×2)-structure is identified as a V^{3+}-oxide by means of XPS. Anisotropic surface diffusion of the (2×2)-oxide is shown to play a decisive role in pattern morphogenesis. This oxide exhibits remarkable mobility on the $Rh(111)$ substrate.

Deposition of nickel on $Rh(111)$ and subsequent exposition to the $H_2 + O_2$ reaction leads to a complex surface composition. Nickel is partially incorporated into the surface region of $Rh(111)$ forming an alloy, and partially present on top of the surface in form of 3-dimensional oxide particles. An inverted model catalyst $Rh(111)/Ni/NiO$ is obtained. It exhibits spatiotemporal pattern formation under reaction conditions, i.e. target patterns and rotating spiral waves can be observed in PEEM, and oscillating

reaction rates can be measured mass spectrometrically. The size of the NiO particles is shown to depend on the total pressure; probably this is also true for the fraction of nickel bound as NiO on top of the surface. Presumably these oxide particles act as a dynamical Ni storage capacity, allowing the surface alloy underneath to adjust its nickel content to particular reaction conditions.

Kurzzusammenfassung

Zwei „inverse" Modell-Katalysator-Systeme (invers bezüglich der gewöhnlichen Struktur geträgerter Katalysatoren, mit Metall-Partikeln auf oxidischen Trägern) wurden untersucht: Rh(111)/VO$_x$ und Rh(111)/Ni/NiO wurden der H$_2$ + O$_2$-Reaktion ausgesetzt, bei $10^{-7} - 10^{-4}$ mbar und $500 - 700$°C. Die Reaktionsdynamik wurde mit Photoemissions-Elektronenmikroskopie (PEEM) und Niederenergie-Elektronen-mikroskopie (LEEM) *in situ* verfolgt. Zusätzliche chemische und strukturelle Informationen wurden gesammelt, in auf einen Mikrometerfokus begrenzen Messungen mit Röntgen-Photoelektronenspektroskopie (μ-XPS) und Niederenergie-Elektronen-beugung (μ-LEED).

Im Falle von Sub-Monolagenfilmen von VO$_x$ auf Rh(111) findet man eine Reihe von Umwandlungen der Katalysator-Oberfläche durch Reaktionsfronten bei der Anpassung des Systems an sich ändernde Partialdrücke der Reaktanten. Unter reduzierenden Bedingungen, d. h. bei hohen Reaktionsraten, kondensiert das Vanadiumoxid zu mesoskopischen Streifenmustern. Diese Muster werden als quasi-stationär bezeichnet, da sie sich im Laufe der Zeit verändern: ihre Längenskala wächst, einem Potenzgesetz folgend, mit der Zeit. Die Musterbildung wird diskutiert im Rahmen der Konzepte *reaktive Phasentrennung* und *spinoidale Entmischung*: die wesentlichen Triebkräfte sind wahrscheinlich die starken attraktiven Wechselwirkungen zwischen V und O, und die Energie der Phasengrenzen zwischen VO$_x$-Inseln und unbedeckter Rhodiumoberfläche. Zwei neuartige VO$_x$-Monolagenstrukturen, die (2×2)- bzw. *split*-(2×2)-Beugungsmuster aufweisen, können beobachtet werden. Die Strukturen scheinen nur unter Reaktionsbedingungen stabil zu sein. Die (2×2)-Struktur wird mit XPS als V^{3+}-Oxid identifiziert. Es wird gezeigt, dass anisotrope Oberflächendiffusion des (2×2)-Oxids eine entscheidende Rolle bei der Morphogenese der Steifenmuster spielt. Die hohe Mobilität dieses Oxids auf der Rh(111)-Oberfläche ist bemerkenswert.

Wenn Nickel auf Rh(111) abgeschieden und anschließend der H$_2$ + O$_2$-Reaktion ausgesetzt wird, führt dies zu einer komplexen Oberflächenzusammensetzung. Das Nickel wird teilweise in die Rh(111)-Oberflächenregion inkorporiert und bildet eine Legierung; der andere Teil befindet sich auf der Oberfläche in Form von 3-dimensionalen NiO-Partikeln. Man erhält einen inversen Modell-Katalysator Rh(111)/Ni/NiO. Dieser weist raum-zeitliche Musterbildung unter Reaktions-

bedingungen auf, d. h., es können Zielscheibenmuster und rotierende Spiralwellen mit PEEM beobachtet werden. Oszillierende Reaktionsraten können massenspektrometrisch erfasst werden. Es wird gezeigt, dass die Größe der NiO-Partikel vom Totaldruck abhängt; dies gilt wahrscheinlich auch für den Anteil des Nickels, welcher in Form von NiO auf der Oberfläche gebunden ist. Vermutlich fungieren diese Oxidpartikel als dynamische Ni-Speicherkapazität, die es der darunter liegenden Oberflächenlegierung erlaubt, ihren Nickelgehalt den jeweiligen Reaktionsbedingungen anzupassen.

Schlüsselwörter: inverser Modellkatalysator · Rhodium · Vanadiumoxid · Nickeloxid · PEEM · LEEM · Selbstorganisation · stationäre Muster · reaktive Phasentrennung · spinoidale Entmischung · chemische Wellenmuster · Ratenoszillationen

Table of content

Abbreviations and symbols

a	Lattice constant
A, B, C	Components of the $Ni2p_{3/2}$-XP spectra
AES	Auger electron spectroscopy
b	Effective atom size
BE	Binding energy
c	Surface concentration
CA	Contrast aperture
CL	Collimator lens
CMA	Cylindrical mirror analyzer
d	Distance
D	Diffusion coefficient
DP	Dispersive plane
e	Elementary charge
E	Energy
E_B	Binding energy
F	Local reaction kinetics term
FOV	Field of view
FWHM	Full width at half maximum
h	Planck´s constant
I	Intensity
IL	Intermediate lens
k	Wave number
k_r	Reaction rate constant
LEED	Low energy electron diffraction
LEEM	Low energy electron microscopy
LG	Lorentzian-Gaussian
M	Molar mass
MCP	Microchannel plate
MEM	Mirror electron microscopy
MLE	Monolayer equivalent
n	Diffraction order

N	Number of atoms or electrons
O_{ad}	Adsorbed atomic oxygen
p	Pressure or partial pressure
PL	Projector lens
QMS	Quadrupole mass spectrometer
STM	Scanning tunneling microscopy
T	Temperature
t	Time
TL	Transfer lens
TMP	Turbomolecular pump
UHV	Ultra-high vacuum
v	Velocity
V	Volume
XPS	X-ray photoemission spectroscopy
*	Adsorption site
α	Scaling law exponent
β	Asymmetry parameter
γ	Contact angle
δ	Angle enclosed by surface normal and photon polarization
θ	Angle enclosed by photoemission direction and surface normal
Θ	Coverage
λ	Wavelength or attenuation length
ν	Frequency
ξ	Experimental parameters
ρ	Density
σ	Angle independent photoionization cross section
φ	Diffraction angle
Φ	Work function
χ	Photoionization cross section
I, II, III, IV	States of the system $Rh(111)/VO_x$
$\sqrt{7}$	$(\sqrt{7} \times \sqrt{7})R19.1°$
$\sqrt{13}$	$(\sqrt{13} \times \sqrt{13})R13.8°$

1. Basic concepts

1.1. Introduction

Catalysis is used since ancient times for the production of alcohol and was first described scientifically around 1800 AD [1]. Nowadays it is involved in most applications of the chemical industry [2]. Heterogeneous catalysis, i.e. the acceleration of gas- or liquid phase reactions by solid surfaces, plays a major role in industrial large scale reactions and waste gas processing.

The understanding of the topic is still inadequate, considering its significance. Heterogeneous catalysts are usually still designed based on empirical data rather than on first principles [2], though major scientific effort has been directed towards that prospect. Since the 1960's surface scientists are investigating the underlying processes, e.g. adsorption/desorption or structural transformations, by studying simplified model systems, following an approach of Langmuir [1]. Although remarkable objectives have been achieved (e.g. [1]), the strategy suffers in most cases from a problem known as the *pressure and material gap* [3].

The term refers to problems extrapolating the results of model studies to real catalysis systems. The *pressure gap* arises because model studies are usually conducted at pressures $< 10^{-3}$ mbar, while industrial catalysis is performed at pressures $> 10^3$ mbar. Low pressure conditions provide a couple of advantages: a high level of purity can be realized, experiments are strictly isothermal due to low conversion rates, and, most of all, analysis techniques based on free electrons are available, which play a unique role in probing surfaces [4].

Most real catalysts are composed of metallic nanoparticles on oxidic support materials, and are therefore different from the single crystals frequently used in surface science (*material gap*). To address the question of how the presence of oxides affects metallic catalytic surfaces, the concept of *inverted model catalysts* was introduced [5]: oxidic particles or sub-monolayer films are deposited on metal single crystals. This way the metal-oxide phase boundaries can be investigated. In such studies promotional effects of the oxide were found, e.g. for hydrogenation reactions on rhodium in presence of various oxides [6, 7], or for CO oxidation on Pd(111) decorated with vanadium oxide [8, 9].

The focus of this study lies on self-organization processes occurring on inverted model catalyst surfaces under reaction conditions. The vacuum chambers used for the experiments are always operated as continuous flow reactors [2], i.e. the reactant gasses are resupplied permanently while the resulting gas mixture is pumped off. Although stationary states can be reached under such conditions, the reaction is kept far off the thermodynamical equilibrium. Self-organization, the formation of dissipative structures, is a common phenomenon in non-equilibrium systems [10].

Dissipative structures can occur in time (oscillations), space (stationary patterns), or both (propagating waves). All three phenomena have been observed in non-equilibrium chemical reactions, first in the liquid phase. Oscillations and chemical wave propagation occur, for example, in the famous Belousov-Zhabotinsky reaction [11]. Stationary patterns, named *Turing*-structures according to their prediction by Turing [12], can be observed in the so-called CIMA reaction [13].

In heterogeneous catalysis rate oscillations were first observed 1970 for the oxidation of CO over platinum [14]. Starting from there, intense research activity led to the discovery, description and understanding of various systems featuring dissipative structures [15−18]. The most versatile system is Pt(110)/CO + O_2, where all three types are observed: oscillations and many types of chemical waves (see section 1.3) [1, 15−18], as well as stationary Turing-type patterns [18, 19]. Another type of stationary structures was first discovered for the $H_2 + O_2$ reaction on a potassium-promoted Rh(110) surface [20] and assigned to a phenomenon called *reactive phase separation* (see section 1.4).

Two different inverted model catalyst systems are subject of the present study, both prepared on Rh(111) supports. Rhodium crystallizes in a face-centered cubic structure (lattice constant: 3.8 Å [4]). For such metals the crystallographic face denoted (111) in the Miller notation (see [4]) corresponds to a plain arrangement of hexagonally close-packed atoms, i.e. each Rh atom is surrounded by six next neighbors at equal distances of 2.7 Å. The Rh(111) surface does not exhibit adsorption-induced reconstructions, but always retains the described atomic arrangement.

Rhodium is a classical noble metal catalyst, mostly applied for NO_x reduction in exhaust gases, e.g. in the automotive catalytic converter [21]. It is also part of catalysts for ammonia oxidation (Ostwald process) and hydrogenation/hydroformylation reactions [22]. Rhodium exhibits high activity catalyzing the $H_2 + O_2$ reaction [23].

The major part of the present work (chapter 3) deals with the behavior of vanadium oxide (VO_x) on the Rh(111) surface when exposed to the $H_2 + O_2$ reaction. Vanadium oxides are not inert, since vanadium easily changes its oxidation state [22]. The main applications of VO_x as an active catalyst are the SO_2 oxidation for sulfuric acid production [24] and the NO_x reduction with ammonia (selective catalytic reduction, SCR) [25]. It can further be used for several selective oxidation reactions in organic chemistry [25]. VO_x in principle catalyses the $H_2 + O_2$ reaction [26], but as shown in section 3.3, it is much less active than noble metals under low pressure conditions.

Mostly sub-monolayer films of VO_x on Rh(111) are investigated here, which can be regarded as inverted model catalysts. The catalysts are characterized *in-situ* by photoemission electron microscopy (PEEM, see section 2.7) as spatially resolving technique. The sample system is found to react drastically to the application of reaction conditions: the surface adjusts to varying conditions by transformations trough reaction fronts (see section 1.3), and the formation of mesoscopic, (quasi-) stationary patterns is observed as a consequence of self-organization.

Those changes of the Rh(111)/VO_x catalyst are investigated in detail. The pattern formation is identified as redistribution of VO_x on the Rh(111) surface; the mesoscale morphology of the patterns is followed with PEEM. For further characterization of the phenomena more advanced methods are applied: low energy electron microscopy (LEEM, see section 2.8) and area-selected electron diffraction (μ-LEED, see sections 2.4, 2.8) make it possible to follow structural and morphological changes on a smaller scale. To gather chemical information, core-level photoemission spectroscopy (XPS, see section 2.6) is used; at the electron-storage ring *Elettra* synchrotron radiation is employed to acquire spatially resolved data. From the results of the different methods a detailed picture of the catalysts behavior under reaction conditions is drawn.

A second inverted model catalyst exposed to the $H_2 + O_2$ reaction is investigated: instead of VO_x, nickel oxide (NiO) particles are present on a Rh(111)/Ni surface (see chapter 4).

Nickel is known to be an effective hydrogenation catalyst (*Raney*-nickel) [22], while it can hardly be used for oxidation reactions: one needs to work extremely oxygen-deficient to prevent the formation of a passivating NiO layer [27].

Under reaction conditions a stationary nickel distribution is reached: a fraction of the metal is located on top of the surface in form of NiO particles, while the other

fraction is incorporated in the near-surface region of the metallic substrate as an alloy. The system hence belongs to the class of bimetallic catalysts, which attracted a lot of attention in the past, due to the prospect of tailoring their properties [28].

Behavior and composition of the composite catalyst are characterized *in situ* with PEEM, LEEM and XPS. Various self-organization phenomena are recognized: different types of chemical waves are observed, and rate oscillations are detected. Furthermore, the Rh(111)/Ni/NiO system is quite complex due to its additional degrees of freedom: nickel can be redistributed laterally and also perpendicular to the surface, depending on the reaction conditions.

1.2 Surface reactions

An equation for a heterogeneously catalyzed reaction is usually written in a very convenient way. CO oxidation is considered as a very simple example:

$$2CO(g) \, + \, O_2(g) \; \xrightarrow{\;\;Pt(111)\;\;} \; 2CO_2(g) \tag{1-1}$$
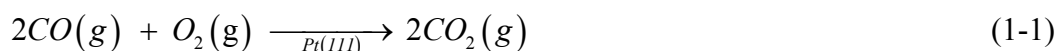
The catalysis by Pt(111) is simply indicated under the reaction arrow. Several elementary steps are summed up in equation (1-1). Such reactions almost always proceed according to a Langmuir-Hinshelwood mechanism, which means that every reactant molecule has to be adsorbed before it can react [2]. For equation (1-1) this implies the following steps [29]:

$$CO(g) \, + \, * \; \rightleftharpoons \; CO(ad) \tag{1-2}$$

$$O_2(g) \, + \, 2* \; \rightleftharpoons \; 2O(ad) \tag{1-3}$$

$$O(ad) \, + \, CO(ad) \; \rightarrow \; CO_2(g) \, + \, 2* \tag{1-4}$$

with * denoting a vacant adsorption site. The double-arrow indicates an adsorption/desorption equilibrium. Since adsorption is in general exothermic, the equilibrium shifts to desorption at higher temperatures; considering only equation (1-2), a low temperature would favor high coverages and thus high reaction probabilities and rates. But the situation is more complex: oxygen adsorbs dissociatively (see equation
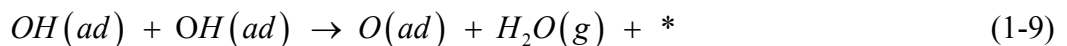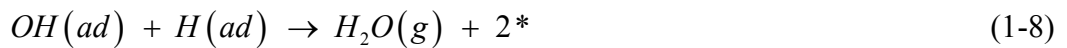
1-3), which has important consequences. For adsorption the O−O bond has to be broken, so it is an activated process and thus slow at low temperatures.

The second consequence of dissociative adsorption is induced by the requirement of two adjacent free adsorption sites. High CO coverages effectively prevent oxygen adsorption by site-blocking; the catalyst is poisoned. On the other hand even a saturated oxygen overlayer on Pt(111) exhibits vacant adsorption sites [30] and still allows CO adsorption (and hence reaction). This introduces the phenomenon of *bistability* [31], which is explained in detail in the next section. Just the consequences have to be mentioned here: under reaction conditions the system exists in one of two stationary states, in an active one (O-covered), or a poisoned one (CO-covered). The reaction conditions are to be chosen appropriately to produce CO_2, which is a weakly adsorbing molecule and immediately leaves the surface at elevated temperatures (see equation (1-4)) [29].

The central reaction in this study is water formation from the elements, catalyzed by Rh(111):

$$2H_2(g) + O_2(g) \xrightarrow{Rh(111)} 2H_2O(g) \tag{1-5}$$
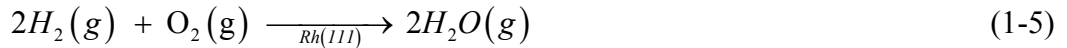
Compared to equation (1-1) it is more complex, but exhibits the same features: bistability with an active and a poisoned state [23], and immediate desorption of the product [32]. The mechanism is not yet understood in every detail [33], however, the essential elementary steps are:

$$O_2(g) + 2* \rightleftharpoons 2O(ad) \tag{1-3}$$

$$H_2(g) + 2* \rightleftharpoons 2H(ad) \tag{1-6}$$

$$O(ad) + H(ad) \rightleftharpoons OH(ad) + * \tag{1-7}$$

$$OH(ad) + H(ad) \rightarrow H_2O(g) + 2* \tag{1-8}$$

$$OH(ad) + OH(ad) \rightarrow O(ad) + H_2O(g) + * \tag{1-9}$$

The most significant difference to CO oxidation lies in equation (1-6). H_2 adsorbs dissociatively in contrast to CO (see equation (1-2)), but at elevated temperatures desorption dominates [34]. Hence hydrogen atoms reside on the surface just for short times, and dense adsorption layers cannot build up. This affects the *bistability*: at high

oxygen coverages the dissociative hydrogen adsorption is prevented, and the catalyst is therefore in a poisoned stationary state. The latter is destabilized by high hydrogen partial pressures and changes into an active stationary state with low overall coverage, only featuring small surface concentrations of O, H and OH.

Water molecules are formed as indicated in the equations (1-8) and (1-9); it is not clear which one of both is the main pathway on Rh(111). For Pt(111) it is believed to be (1-8) [35], but that might be different for rhodium and even depend on the particular reaction conditions.

1.3 Chemical waves

A heterogeneously catalyzed reaction is a reaction-diffusion system and can be described by a set of differential equations [18], one for each surface species i:

$$\frac{\partial c_i}{\partial t} = F_i\left(\xi, c_a, c_b, ..., c_k\right) + D_i \nabla^2 c_i \tag{1-10}$$

with the local surface concentrations c_i. The expression F_i represents the local reaction kinetics depending on the experimental parameters ξ (e.g. temperature and partial pressures), and is followed by a diffusion term with the diffusion constant D_i (assuming Fick's law to be valid). In case of self-organizing systems at least one F_i is a nonlinear function, representing an auto-catalytic or inhibitory step. This gives rise to the term *nonlinear dynamics* for the field of research.

In the following description of a simple model for nonlinear behaviour, spatial homogeneity is assumed; the diffusion term of equation (1-10) hence equals zero. A system containing two species u and v with variable concentrations can be described by:

$$\frac{\partial c_u}{\partial t} = F_u\left(\xi, c_u, c_v\right), \qquad \frac{\partial c_v}{\partial t} = F_v\left(\xi, c_u, c_v\right) \tag{1-11}$$

If the system is in a stationary state, the concentrations do not change with time. To find solutions for stationary states one consequently sets the time derivatives equal to zero, and hence $F_u = 0$ and $F_v = 0$. The solutions of these individual equations are called the *nullclines* of the system.

For graphical representation of such problems one usually chooses the *phase space*, spanned by axes denoting the concentrations c_i at constant ξ. The state of the system at a particular time is represented by a point in phase space, and since concentrations are variable in general, such a point can move with time, drawing a *trajectory*.

The intersections of the nullclines in phase space are called fixed points. The corresponding states can be stable or unstable with respect to a perturbation. If at a fixed point the variables are slightly changed, the system either returns to the fixed point (stable), or the perturbation grows (unstable). Stable fixed points represent the experimentally observable stationary states of the system. To illustrate the situation in figure 1.1 nullclines are chosen, corresponding to a hypothetical reaction system. The nullcline of F_u is a third-degree polynomial, representing a non-linear reaction step; the one of F_v is a straight line, which can intersect in four different ways. This simple system is known as the FitzHugh-Nagumo model [18].
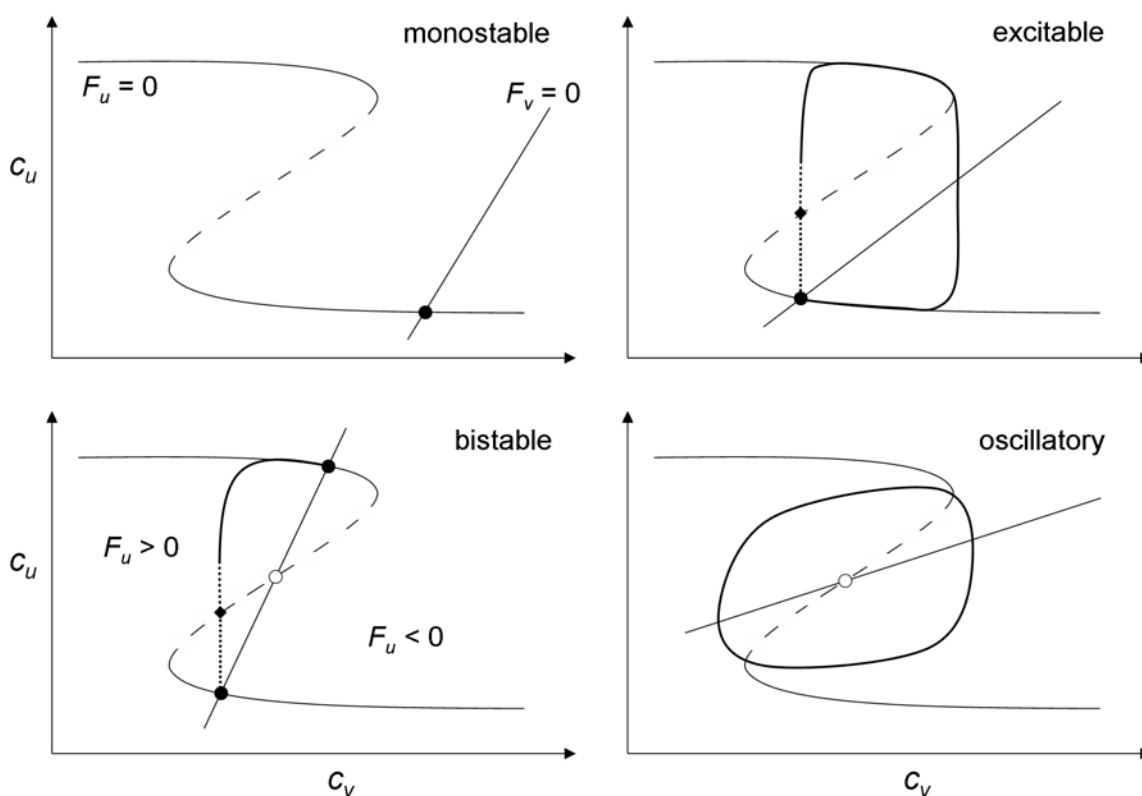

Figure 1.1: Schematic representation of four exemplary solutions of the FitzHugh-Nagumo model. The thin solid lines are the nullclines; the dashed part is the separatrix. The thick solid lines are trajectories, with the dotted parts representing external excitations. Fixed points are drawn as ● (stable) or ○ (unstable), ♦ stands for a threshold value.

The simplest solution of the model is *monostable*. There is just one nullcline intersection, far off the S-shaped region. Hence the system exhibits just one stable state which attracts every trajectory within the phase space. A stable fixed point is an *attractor*.

Due to the non-linearity of the F_u nullcline there can be more then one intersection, as in the case of *bistability*. Two of the three fixed points are found to be stable, while the third one is unstable. The system can never reside at an unstable fixed point, because it is unstable even against infinitesimal perturbations. So the internal noise of a real system is sufficient to drive it away; trajectories are repelled.

A bistable system usually occupies one of its two stable states. It relaxes quickly from small perturbations, returning to the stable fixed point. But if one concentration is changed beyond a certain threshold value, as indicated in figure 1.1 (dotted line), the trajectory will be attracted by the other stationary state and reside there until another perturbation occurs.

The threshold is, in this case, determined by the dashed part of the F_u nullcline. This dashed line separates the regions belonging to the two attractors, and is therefore called a *separatrix*. This part of the nullcline repels trajectories: above the separatrix $F_u > 0$, so c_u will grow according to equation (1-11), driving the trajectory upwards. Below the separatrix the trajectory will be driven downwards.

In case of an *excitable* system there is just one nullcline intersection, but in contrast to monostability it is close to the separatrix. If the latter is crossed by a perturbation (called excitation in this case), the trajectory is driven further upwards and has to travel a long way trough phase space in order to return to the stationary state. Now the system can be excited again. Whether the trajectory follows the F_u nullcline as indicated in figure 1.1, or travels a deviating way, depends on the details of F_u and F_v.

The fourth possibility is a single intersection yielding an unstable fixed point, which does hence not attract trajectories. They travel on a loop around the fixed point instead, so concentrations change periodically; *oscillatory* behavior is observed. The loop is called a *limit cycle* and represents another type of attractor. As stated above for the excitable system, trajectories do not necessarily travel along the F_u nullcline, as indicated in figure 1.1 for the oscillatory case.

In the spatially homogeneous system described by equation (1-11), concentrations consequently change in a spatially homogeneous way. This is usually not

the case in real systems where the diffusion terms do not vanish. Extending the FitzHugh-Nagumo model to describe a catalytic surface, the latter can be regarded as an array of small, homogeneous compartments which are coupled by diffusion of at least one species. Mediated by this coupling, perturbations can spread laterally; the phenomenon is known as chemical wave propagation.

If a stationary state of a bistable surface reaction is sufficiently strong perturbed, the surface is transformed into the other stationary state. In real systems this transformation process is usually initiated at mesoscopic surface inhomogeneities (defects) with deviating adsorption properties. Here a critical threshold concentration, e.g. of c_u, can build up. u can then diffuse into the surrounding surface compartments and perturb those, exceeding the separatrix, as illustrated in figure 1.1 (c). The perturbed compartments are hence transformed into the new stationary state, featuring a large concentration of u; the species increases auto-catalytically. Further vicinal surface compartments are perturbed and transformed via diffusional coupling by u: the perturbation propagates about the whole surface, transforming it into the new stationary state. This is called a *reaction front*.

The velocity v of front propagation depends on the diffusion constant of the diffusing species *i* and the reaction rate [15]:

$$\text{v} \sim \sqrt{D_i \cdot k_r} \tag{1-12}$$

with k_r as an effective rate constant summarizing the whole reaction. At constant conditions the front travels with constant velocity and profile until the complete surface is transformed. Experimentally, reaction fronts are often triggered by changing the reaction conditions ξ, and by fine-tuning ξ the velocity can be controlled. The reaction front can even be stopped or reversed.

In an excitable system perturbations propagate like described above for bistability. The main difference is that the system returns to the original stationary state (see figure 1.1 (b)). In contrast to a reaction front, the surface remains unchanged after the chemical wave has passed. Such a wave is called a *pulse*.

Figure 1.2 illustrates how perturbations propagate through a reaction-diffusion system, in case of bistability or excitability, respectively. A reaction front is characterized by a steep increase of one surface concentration, transforming one stationary state into another. For a pulse the profiles of both species are indicated. *u*

increases quickly in a concentration step initiating the pulse, and is therefore referred to as *activator*. v is called *inhibitor*, because c_v increases slowly at high c_u up to a critical value, which causes c_u to decrease rapidly. Both concentrations return to their stationary values then, and the pulse has passed. For pulses following one another, one speaks of *pulse trains*. In oscillatory systems a similar picture is found.
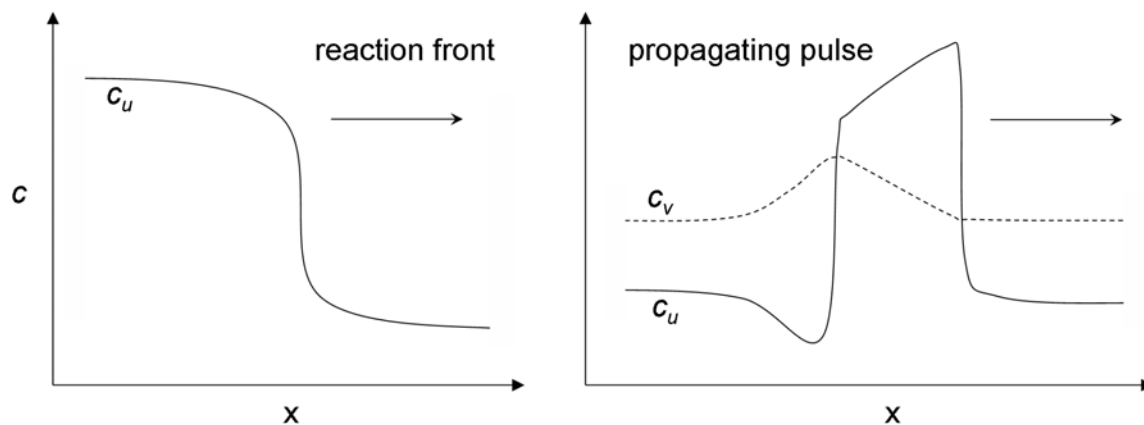

Figure 1.2: 1-dimensional concentration profiles of chemical waves versus the spatial coordinate. The propagation direction is indicated by an arrow. In case of the pulse profiles for activator u and inhibitor v are given.

The excitation of an excitable system can be realized, e.g. by a laser pulse which locally heats the surface and desorbs some inhibitor. On an isotropic surface a circular pulse is triggered then. However, in most experiments mesoscopic surface defects cause the excitation. A defect has usually different adsorption properties compared to the surrounding surface, which might lead to enrichment of the activator species until excitation occurs. Since the activator will accumulate again, triggering pulses periodically, a *target pattern* is formed by circular pulses traveling away from the defect. The latter is termed *pacemaker* in this case. Also *rotating spiral waves* can be pinned by defects, i.e. a spiral wave rotates around a core, with a rotational period determined by the properties of the defect. Target patterns and rotating spiral waves are characteristic for excitable and for oscillatory surface reactions [1, 15−18]. Therefore it can be difficult to distinguish between oscillatory and excitable behavior experimentally; the decisive criterion is the fixed eigenfrequency of oscillatory systems, while in the excitable case the properties of pacemakers determine the frequencies.

1.4 Stationary patterns

As already mentioned in section 1.1, stationary patterns can form in an activator-inhibitor system as a result of a Turing-instability of the spatially homogeneous state. Turing structures are caused by strongly deviating diffusivities, i.e. the inhibitor diffuses much faster than the activator [18].

Although strong differences in diffusivity occur quite often in surface chemistry, just one example for a Turing structure is known so far [19]. Another class of stationary structures seems to be more common on surfaces, which has been termed *reactive phase separation*. In contrast to Turing structures, strong energetic interactions between adsorbates are the main driving force. The phenomenon is of crucial interest for the present study, and therefore a short review shall be given in the following.

Reactive phase separation in catalysis was first observed studying the $H_2 + O_2$ reaction on a microstructured, bimetallic Rh(110)/Pt surface [36]; the stationary structures were termed "Turing-like patterns". It was already suspected and later demonstrated [37] that potassium contamination had caused the effect, which consequently also occurs on a K-promoted Rh(110) surface exposed to the $H_2 + O_2$ reaction [20]. Potassium concentration patterns were generated starting from a surface homogeneously covered with K and O; addition of hydrogen initiates reduction fronts which "pick up" potassium and transport it until colliding with other fronts [20, 38]. In the collision zones islands are formed, which consist of coadsorbed K and O, while the rest of the surface is depleted of potassium [39]. The patterns formed this way are irregular and of a large length scale (~1 mm); starting from reducing conditions instead leads to spontaneous formation of more regular structures on a smaller, intrinsic length scale (~50 μm) [40], as shown in figure 1.3.

It could be shown by kinetic simulations [40, 41] that the pattern formation is driven by the energetic interactions of K and O. Macroscopic phase separation, i.e. the formation of large K + O islands, would occur anyway due to the chemical affinity of those elements. The presence of the reaction just accelerates the process and introduces a mesoscopic length scale.

The basic requirements for reactive phase separation in heterogeneous catalysis are quite loose. The catalyst has to be at least binary, with one of its components exhibiting a strong energetic interaction with one of the reactants; in addition one of the

components has to be mobile. It has been shown theoretically that patterns can form, regardless if the energetic interactions are attractive or repulsive, or if the interacting component is a promoter, a poison, or inactive [42].
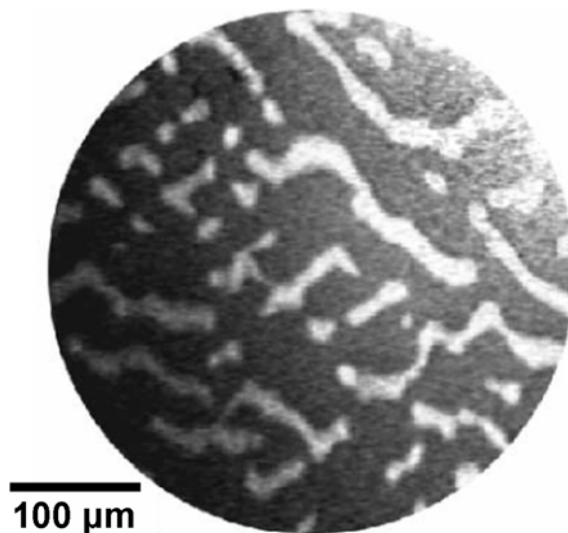

Figure 1.3: PEEM image of stationary concentration patterns on Rh(110) under $H_2 + O_2$ reaction conditions. The bright structures are composed of coadsorbed potassium and oxygen, while the dark area is depleted of both elements. The temperature is $\sim 300°C$, the pressure is about $5 \cdot 10^{-7}$ mbar. Reproduced with permission from [40].

The phenomenon should hence be widely spread. It was found indeed in a number of systems, first in closely related ones: cesium behaves very similar to potassium, in Rh(110)/Cs/$H_2 + O_2$ and Rh(110)/Cs/K/$H_2 + O_2$ [43]. Exchanging oxygen for nitric oxide, the system Rh(110)/K/$H_2 + NO$ also exhibits stationary patterns [44]; since this system is excitable (with or without K), potassium is transported with O-rich pulses, so spatiotemporal K + O patterns are found [44−46].

The observation of stationary concentration patterns of gold in the system Rh(110)/Au/$H_2 + O_2$ [47, 48] is an example where the mobile catalyst component (Au) is not a promoter, but just blocks adsorption sites; it also does not interact energetically with the reactants. In this case the chemical affinity of Rh(110) towards oxygen drives the redistribution of gold. Pattern formation also occurs if palladium is added, with an Au + Pd enriched phase separating from Rh(110)-O [49, 50]. Various types of structures are formed, i.e. large/small or round/elongated islands, or lamellae, depending on coverage and temperature. For Rh(110)/Au/Pd/$H_2 + O_2$ the length scale of lamellar structures depends on the total pressure via a power law, so the morphology can be controlled [49].

The studies mentioned above demonstrate that reactive phase separation can significantly modify bimetallic catalysts. The present work introduces new examples for such self-organization phenomena, showing that also composites of metals and oxides, as models for real catalysts, are affected in complex ways.

1.5 References

[1]   G. Ertl, *Reaktionen an Oberflächen: vom Atomaren zum Komplexen*, Angew. Chem. 120 (2008), 3578;

        G. Ertl, *Reactions at Surfaces: From Atoms to Complexity*, Angew. Chem. Int. Ed. 47 (2008), 3524.

[2]   I. Chorkendorff, J. W. Niemantsverdriet, *Concepts of Modern Catalysis and Kinetics*, Wiley-VCH, Weinheim 2003.

[3]   R. Imbihl, R. J. Behm, R. Schlögl, *Bridging the pressure and material gap in heterogeneous catalysis*, Phys. Chem. Chem. Phys. 9 (2007), 3459.

[4]   G. Ertl, J. Küppers, *Low Energy Electrons and Surface Chemistry*, VCH, Weinheim 1985.

[5]   G.-M. Schwab, *Electronics of Supported Catalysts*, Adv. Catal. 27 (1987), 1.

[6]   A. B. Boffa, C. Lin, A. T. Bell, G. A. Somorjai, *Lewis acidity as an explanation for oxide promotion of metals: implications of its importance and limits for catalytic reactions*, Catal. Lett. 27 (1994), 243.

[7]   W. Reichl, K. Hayek, *Vanadium Oxide Overlayers on Rhodium: Influence of the Reduction Temperature on the Composition and on the Promoting Effect in CO Hydrogenation*, J. Catal. 208 (2002), 422.

[8]   M. Sock, S. Surnev, M. G. Ramsey, F. P. Netzer, *Adsorption and reaction of CO on vanadium oxide–Pd(111) "inverse" model catalysts: an HREELS study*, Top. Catal. 14 (2001), 15.

[9]   J. Schoiswohl, S. Eck, M. G. Ramsey, J. N. Andersen, S. Surnev, F. P. Netzer, *Vanadium oxide nanostructures on Rh(111): Promotion effect of CO adsorption and oxidation*, Surf. Sci. 580 (2005), 122.

[10]   G. Nicolis, I. Prigogine, *Self-Organization in Nonequilibrium Systems*, Wiley, New York 1977.

[11]   A. M. Zhabotinsky, *A history of chemical oscillations and waves*, Chaos 1 (1991), 379.

[12]   A. Turing, *The Chemical Basis of Morphogenesis*, Philos. Trans. R. Soc. B 237 (1952), 37.

[13]   V. Castets, E. Dulos, J. Boissonade, P. De Kepper, *Experimental Evidence of a Sustained Standing Turing-Type Nonequilibrium Chemical Pattern*, Phys. Rev. Lett. 64 (1990), 2953.

[14]   P. Hugo, *Stabilität und Zeitverhalten von Durchfluß-Kreislauf-Reaktoren*, Ber. Bunsenges. Phys. Chem. 74 (1970), 121.

[15]   R. Imbihl, *Oscillatory Reactions on Single Crystal Surfaces*, Prog. Surf. Sci. 44 (1993), 185.

[16]   F. Schüth, B. E. Henry, L. D. Schmidt, *Oscillatory Reactions in Heterogeneous Catalysis*, Adv. Catal. 39 (1993), 51.

[17]   R. Imbihl, G. Ertl, *Oscillatory Kinetics in Heterogeneous Catalysis*, Chem. Rev. 95 (1995), 697.

[18]   R. Imbihl, *Nonlinear dynamics on catalytic surfaces*, Catal. Today 105 (2005), 206.

[19]   J. Falta, R. Imbihl, M. Henzler, *Spatial Pattern Formation in a Catalytic Surface Reaction: The Facetting of Pt(110) in CO+O_2*, Phys. Rev. Lett. 64 (1990), 1409.

[20]   H. Marbach, S. Günther, B. Luerßen, L. Gregoratti, M. Kiskinova, R. Imbihl, *Selforganization of alkali metal on a catalytic metal surface*, Catal. Lett. 83 (2002), 161.

[21]   K.C. Taylor, *Nitric Oxide Catalysis in Automotive Exhaust Systems*, Catal. Rev. Sci. Eng. 35 (1993), 457.

[22]   A. F. Hollemann, E. Wiberg, N. Wiberg, *Lehrbuch der Anorganischen Chemie*, Verlag deGruyter, Berlin 1995.

[23]   A. Schaak, R. Imbihl, *Bistability and formation of low work function areas in the O_2 + H_2 reaction on a Rh(111) surface*, J. Chem. Phys. 113 (2001), 9822.

[24]   M. M. Dojčinović, S. V. Mentus, *The kinetics and mechanism of the catalytic oxidation of sulphur dioxide*, J. Serb. Chem. Soc. 53 (1988), 117.

[25]   G. C. Bond, S. F. Tahir, *Vanadium oxide monolayer catalysts: Preparation, characterization and catalytic activity*, Appl. Catal. 71 (1991), 1.

[26]   K. Mori, M. Miura, A. Miyamoto, Y. Murakami, *Catalytic Reactions on Well-Characterized Vanadium Oxide Catalysts. 3. Oxidation of Hydrogen*, J. Phys. Chem. 88 (1984), 5232.

[27]   K. A. Dadayan, G. K. Boreskov, V. I. Savchenko, E. M. Sadovskaya, G. S. Yablonskii, *Oxidation of Hydrogen on Nickel(110)*, Kinet. Catal. 20 (1979), 654.

[28]   C. T. Campbell, *Bimetallic Surface Chemistry*, Annu. Rev. Phys. Chern. 41 (1990), 775.

[29]   M. Ehsasi, M. Matloch, O. Frank, J. H. Block, K. Christmann, F. S. Rys, W. Hirschwald, *Steady and nonsteady rates of reaction in a heterogeneously catalysed reaction: Oxidation of CO on platinum, experiments and simulations*, J. Chem. Phys. 91 (1989), 4949.

[30]   J. L. Gland, *Molecular and Atomic Adsorption of Oxygen on the Pt(111) and Pt(S)-12(111)×(111) Surfaces*, Surf. Sci. 93 (1980), 487.

[31]   M. Berdau, G. G. Yelenin, A. Karpowicz, M. Ehsasi, K. Christmann, J. H. Block, *Macroscopic and mesoscopic characterization of a bistable reaction system: CO oxidation on Pt(111) surface*, J. Chem. Phys. 110 (1999), 11551.

[32]   A. Beniya, K. Mukai, Y. Yamashita, J. Yoshinobu, *Coverage-dependent sticking probability and desorption kinetics of water molecules on Rh(111)*, J. Chem. Phys. 129 (2008), 016101.

[33]   D. F. Padowitz, S. J. Sibener, *Kinetics of hydrogen oxidation to water on the Rh(111) surface using multiple source modulated molecular beam techniques*, Surf. Sci. 254 (1991), 125.

[34]   J. T. Yates Jr., P. A. Thiel, W. H. Weinberg, *The Chemisorption of Hydrogen on Rh(111)*, Surf. Sci. 84 (1979), 427.

[35]   A. B. Anton, D. C. Cadogan, *The mechanism and kinetics of water formation on Pt(111)*, Surf. Sci. 239 (1990), L548.

[36]   E. Schütz, F. Esch, S. Günther, A. Schaak, M. Marsi, M. Kiskinova, R. Imbihl, *Bimetallic catalysts as dissipative structures: stationary concentration patterns in the O_2 + H_2 reaction on a composite Rh(110)/Pt surface*, Catal. Lett. 63 (1999), 13.

[37] S. Günther, H. Marbach, R. Hoyer, R. Imbihl, L. Gregoratti, A. Barinov, M. Kiskinova, *On the origin of stationary concentration patterns in the H_2+O_2 reaction on a microstructured Rh(110)/Pt surface with potassium*, J. Chem. Phys. 117 (2002), 2923.

[38] H. Marbach, M. Hinz, S. Günther, L. Gregoratti, M. Kiskinova, R. Imbihl, *Mass transport of alkali metal in reaction fronts on a catalytic metal surface*, Chem. Phys. Lett. 364 (2002), 207.

[39] H. Marbach, S. Günther, T. Neubrand, R. Hoyer, L. Gregoratti, M. Kiskinova, R. Imbihl, *Photoelectron Spectromicroscopy of Potassium Redistribution in the $O_2 + H_2$ Reaction on Rh(110)*, J. Phys. Chem. B 108 (2004), 15182.

[40] Y. De Decker, H. Marbach, M. Hinz, S. Günther, M. Kiskinova, A. S. Mikhailov, R. Imbihl, *Promoter-Induced Reactive Phase Separation in Surface Reactions*, Phys. Rev. Lett. 92 (2004), 198305.

[41] M. Hinz, S. Günther, H. Marbach, R Imbihl, *Mathematical Modelling of Reactive Phase Separation in the System Rh(110)/K/O_2 + H_2*, Phys. Rev. B 108 (2004), 14620.

[42] Y. De Decker, A. S. Mikhailov, *Promoter-Induced Nonlinear Pattern Formation in Surface Chemical Reactions*, J. Phys. Chem. B 108 (2004), 14759.

[43] H. Marbach, *Der Einfluss von Alkalimetallen auf musterbildende Reaktionen auf einer Rh(110) Oberfläche*, Thesis (2002), Hannover.

[44] L. Hong, M. Hesse, R. Imbihl, *Patterns in the NO + H_2 Reaction on Rh(110) Modified by Coadsorbed Potassium*, J. Phys. Chem. C 113 (2009), 4174.

[45] H. Marbach, S. Günther, T. Neubrand, R. Imbihl, *Mass transport of alkali metal with pulses: catalytic NO reduction with hydrogen on Rh(1 1 0)/K*, Chem. Phys. Lett. 395 (2004), 64.

[46] L. Hong, H. Uecker, M. Hinz, L. Qiao, I. G. Kevrekidis, S. Günther, T. O. Mentes, A. Locatelli, R. Imbihl, *Mass transport of alkali metal with pulses in a surface reaction*, Phys. Rev. E. 78 (2008), 055203.

[47] A. Locatelli, S. Heun, M. Kiskinova, *Direct observation of reaction-induced lateral redistribution of sub-monolayers of Au deposited on a Rh(1 1 0) surface*, Surf. Sci. 566-568 (2004), 1130.

[48] A. Locatelli, C. Sbraccia, S. Heun, S. Baroni, M. Kiskinova, *Energetically Driven Reorganization of a Modified Catalytic Surface under Reaction Conditions*, J. Am. Chem. Soc. 127 (2005), 2351.

[49] A. Locatelli, T. O. Mentes, L. Aballe, A. Mikhailov, M. Kiskinova, *Formation of Regular Surface-Supported Mesostructures with Periodicity Controlled by Chemical Reaction Rate*, J. Phys. Chem. B 110 (2006), 19108.

[50] A. Locatelli, L. Aballe, T. O. Mentes, F. Z. Guo, M. Kiskinova, *A spectro-microscopic study of the reactive phase separation of Au + Pd and O on Rh(110)*, Surf. Sci. 601 (2007), 4663.

2. Instruments and methods

2.1 The ultra-high vacuum (UHV) chamber

Most of the experiments were conducted in a standard 80 L UHV chamber (Varian). A 360 L/s turbomolecular pump (Leybold-Heraeus Turbovac 360) serves as main pump. An ion getter pump (Varian VacIon, 80 L/s) and a titanium sublimation pump (Varian) are available in addition. Each time after venting the chamber it was baked, typically at 130°C for 30 h, while being pumped; by this procedure atmospheric contaminants are minimized. After the bake-out, base pressures of $2 \cdot 10^{-10}$ mbar or lower were reached, the residual gas consisting of H_2, H_2O, CO and CO_2 with detectable traces of O_2, NO and hydrocarbons. The total pressure was measured with an uncalibrated Bayard-Alpert type ion gauge (Varian); the readout was taken directly for O_2, while it was multiplied by a factor of 2 for H_2 to take the instruments lower sensitivity towards hydrogen into account (see manual).

The sample manipulator allows only small movements in the z-direction and thus just one working level, which is schematically displayed in figure 2.1. The manipulator features five degrees of freedom: in addition to linear movements along the spatial directions (x, y, z), the face of the sample (perpendicular to the drawing plane of figure 2.1) can be aligned using two angular movement options. Since being mounted on an L-type construction, the sample can be rotated on a circle around the z-axis (dashed line in figure 2.1) and tilted against z.

Utilizing these options, the face of the sample can be adjusted to the surrounding instruments for surface preparation and analysis. For sample cleaning an ion gun was mounted (Leybold-Heraeus IQE 10/35), allowing ion bombardment at 0.5 to 5 keV. Vanadium was deposited using a home-built electron beam evaporator with integrated flux monitor; the metal was evaporated from the tip of a high purity rod (> 99.8 %, Goodfellow). To monitor the vanadium coverage and detect possible contaminants an Auger spectrometer (Omicron CMA 150) was used, consisting of a cylindrical mirror analyzer (CMA) with an integrated electron gun. A 4-grid LEED optics (VSI ErLEED 3000 D) served for structural characterization of the sample. The main method of this work is to follow the surface dynamics *in situ*, which was performed using a home-built photoemission electron microscope (PEEM), developed by Engel [1]. The sample was
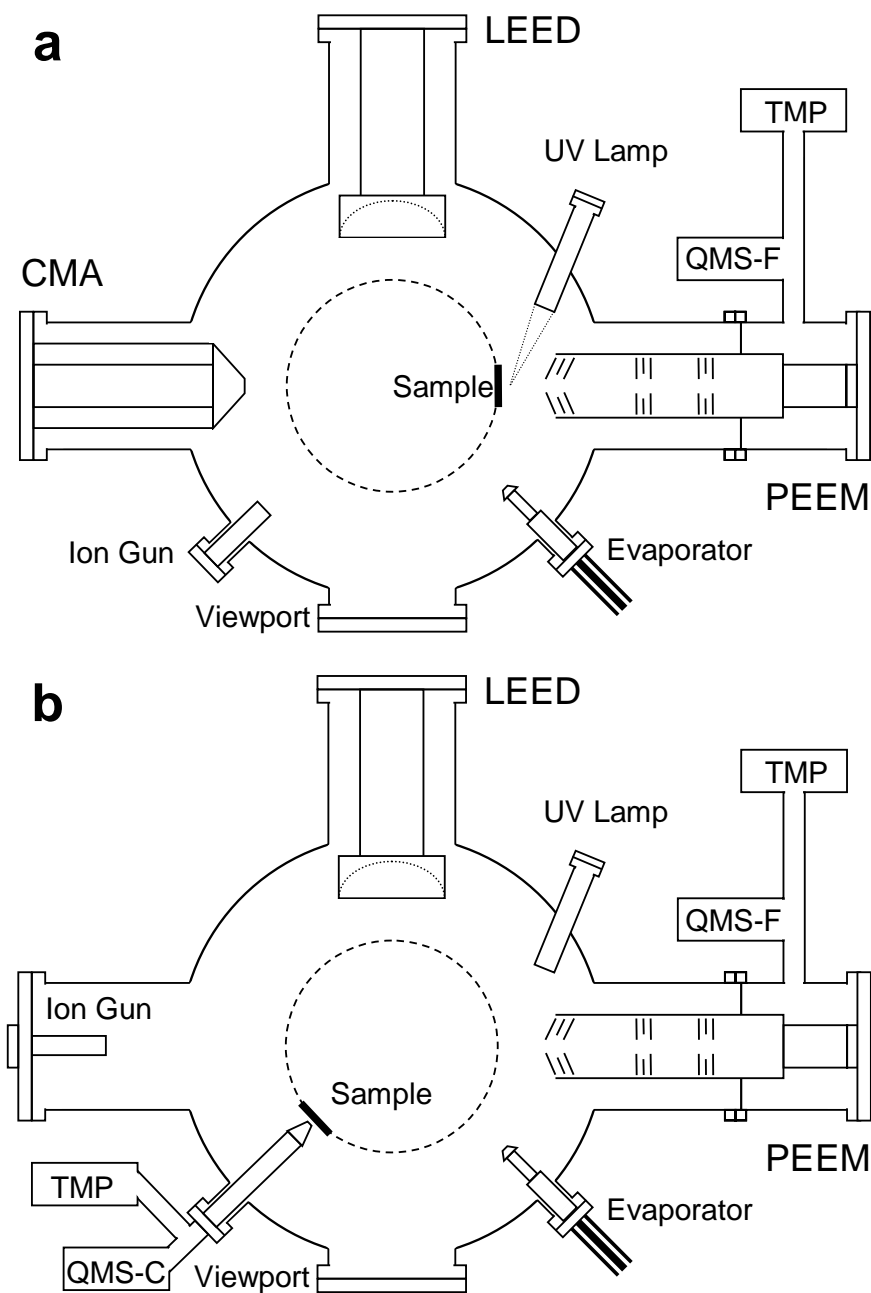
Figure 2.1: (a) Original chamber setup allowing PEEM, LEED and Auger spectroscopy. The sample is in PEEM position. (b) Rearranged chamber setup for rate measurement with the sample in the correspondent position.

illuminated by a D_2 discharge lamp; the instrument itself was differentially pumped by a turbomolecular pump (TMP, Pfeiffer TMU 261 P, 230 L/s) to allow working pressures up to 10^{-3} mbar. As illustrated in figure 2.1, behind the PEEM a quadrupole mass spectrometer with faraday cup detector (QMS-F, Pfeiffer QMA 200) was mounted to analyze the gas stream pumped off the chamber through the PEEM orifice. The intention behind this arrangement was, in addition to overcome the lack of space on the working

level, to perform rate measurements synchronously with PEEM. This turned out to be hardly feasible, because the specimen cannot be positioned close enough to the PEEM orifice for effective background discrimination. To perform rate measurements, the original chamber setup displayed in figure 2.1 (a) had to be modified.

At some point of the experiments the chamber was rearranged according to figure 2.1 (b). The Auger spectrometer was removed to gain space and replaced by the ion gun. In its original location an additional quadrupole mass spectrometer (Hiden Analytical RC RGA HALO 201) with a channeltron electron multiplier (QMS-C) was mounted on a proper cone. The sample could approach the orifice very closely (< 1 mm), being positioned in line of sight with the QMS ion source; an additional TMP (Pfeiffer TMU 071 P, 60 L/s) provided differential pumping.

The gasses were supplied via a gas line connected to the main chamber. They were dosed through sapphire-sealed variable leak valves (Varian) by manual operation. Hydrogen 5.0 and Argon 5.0 were taken out of minicans (Messer-Griesheim, 12 bar, 1 L); contaminants were mass spectrometrically detected to be < 1 ‰. Oxygen 5.6 was taken out of a regular steel gas bottle (Linde); the measured impurity was < 5 ‰.

2.2 Sample mounting and preparation

Two different Rh(111) samples were used in the experiments. Both were produced by MaTecK and prepared according to standard procedures: crystallization by zone melting (purity > 99.99 %), x-ray orientation and spark erosion cutting (miscut < 2°) and polishing with diamond paste (roughness < 0.03 μm).

Figure 2.2 shows a photograph of the mounted sample. It is held by two tantalum wires (0.25 mm) welted to the rim; the wires themselves are welted to two stainless steel rods. These are held by copper blocks also carrying an electron bombardment heater (behind the sample). These parts always move as one unit attached to the manipulator.

The sample was usually heated resistively by a current up to 10 A conducted through the tantalum wires; a sample temperature of 750°C could be achieved this way. If higher temperatures were required, additional electron bombardment provided enough power to reach 1200°C. For the good heat conductance of rhodium, the sample temperature was assumed to be homogeneous at all times; it was measured by a K-type thermocouple welted to the rim of the sample (wires attached to the top side, figure 2.2).

Temperature readout was performed by a PID-controller coupled to the power supply for resistive heating; this setup allowed constant temperatures ($\Delta T < 1$ K) over long times.
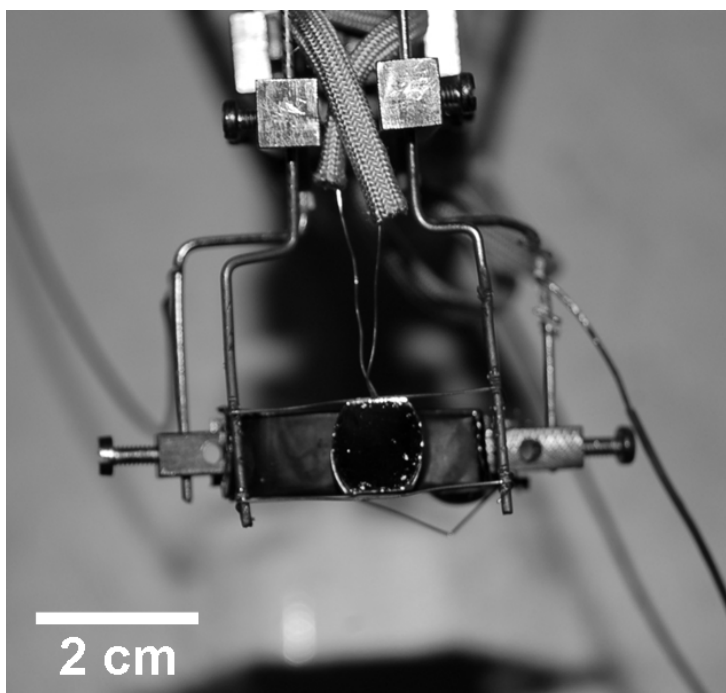

Figure 2.2: Rh(111)-crystal mounted on the sample holder. The thermocouple is welted to the rim; behind the sample an electron bombardment heater is visible.

The roughness remaining from the polishing process could be reduced to atomic dimensions by repeated application of a cleaning cycle, which was also used to remove vanadium and nickel thin films between the experiments. First the sample was bombarded with argon ions (sputtering) at 1 keV ion energy for 90 min at 500°C; the Ar-pressure of about $3 \cdot 10^{-5}$ mbar resulted in an ion current of ~ 2 μA measured on the sample. The second step was annealing the sample, heating it up to 1100°C and keeping it above 1000°C for about 1 min. Then the sample was oxidized for 20 min at 750°C and $2 \cdot 10^{-6}$ mbar oxygen, followed by another annealing step as described before. After this treatment the sample usually showed a clear fcc-(111) diffraction pattern in LEED and a clean Auger spectrum (see figures 2.5 (c) and 2.6). It has to be noted that, while most of the common contaminants (Si, S, Fe, Ca, Na) can be excluded by Auger electron spectroscopy, carbon can not. The rhodium signal at 256 eV (Rh_{256}) exhibits a significant shoulder around 270 eV, which is where the only carbon signal C_{271} is located (see figure 2.6) [2]. Thus the presence of small amounts of carbon in the experiments cannot be excluded.

For a well-prepared low-index single crystal surface one might expect an atomically flat surface, but that is only true on very small length scales. Figure 2.3 shows a LEEM image (low energy electron microscopy, see section 2.8) of the clean surface with all its features: there are flat terraces hundreds of nm wide, as well as heavily stepped areas (step bunches, dark grey lines) and defects of various sizes (black).
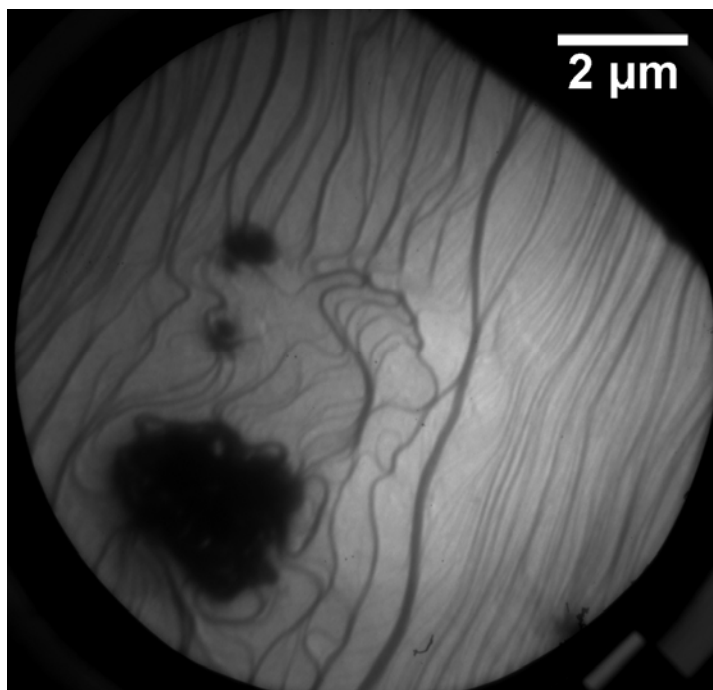

Figure 2.3: Exemplary LEEM image of the clean surface, showing flat terraces (homogeneously bright), supposedly single atomic steps (faint grey lines), step bunches (darker grey lines) and defects (black). Recorded at 42 eV incidence energy.

2.3 Vanadium deposition

Vanadium was deposited using a home-build electron beam evaporator. The metal evaporates from the tip of a 2 mm thick rod (Goodfellow, purity > 99.8 %) on +1500 V bias potential, while a grounded ring-filament supplies electrons. In addition to neutral vanadium atoms and clusters, the vapor contains an ionized fraction utilized to monitor the vanadium flux: a probe electrode between V-rod and sample registers an ion current proportional to the flux, and multiplication with the deposition time gives a measure for the vanadium dosage.

The VO_x coverage was calibrated with an Auger electron spectroscopy (AES, see section 2.5) experiment. At 400°C sample temperature and $2 \cdot 10^{-7}$ mbar O_2 reactive

evaporation occurs; since the Rh(111)-surface is covered by adsorbed oxygen under these conditions, impinging V particles are readily oxidized to vanadium oxide. The growth behavior is well known for such conditions [3, 4]: with increasing dosage 2-dimensional islands grow and coalesce to a wetting layer, before 3D-crystallites are formed on top (Stranski-Krastanov growth mode). Such behaviour is reflected in the Auger spectra. While below the full wetting coverage more and more area gets covered, the V signal intensity increases steeply with the growing dosage, because all vanadium resides in the topmost layer and is detected with full efficiency. If vanadium is, in contrast to that, deposited on top of a wetting layer, it screens the vanadium in the wetting layer from full efficient detection. Therefore, the V signal intensity increases less steep with the dosage beyond the wetting coverage. This effect has often been exploited for monolayer calibration [5].

A calibration graph recorded under the conditions denoted above (400°C, $2 \cdot 10^{-7}$ mbar O_2) is displayed in figure 2.4; vanadium was added in small increments and each time an Auger spectrum was measured. The expected change of slope indicating the monolayer dosage is clearly defined at 1560 nA·s. Since the vanadium flux is constant (± 1 %) after warming up the evaporator, the deposition time for any desired coverage can easily be calculated. Usually ion currents around 1 nA were chosen, which results in deposition times up to 30 min per monolayer. For all the experiments presented in this work vanadium was deposited like described here.
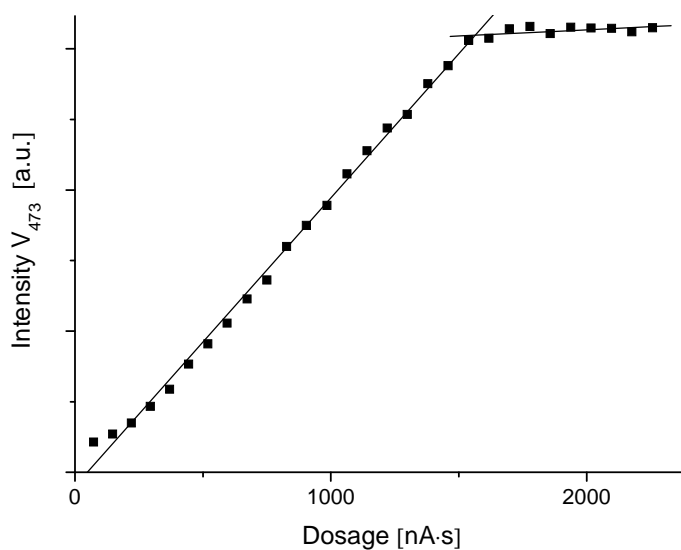

Figure 2.4: AES calibration curve for vanadium evaporation at 400°C and $2 \cdot 10^{-7}$ mbar O_2; the straight lines are fitted to the experimental data. The slope change at 1560 nA·s is supposed to indicate the wetting coverage. The electric current results from an ionized fraction of the evaporated vanadium and was measured by a picoampere meter (Keithley).

The AES coverage calibration was used throughout all PEEM and mass spectrometer experiments and also in a publication [6]. The calibration graphs were reproducible and apparently clearly defined, and beam damage could not be detected with AES. However, during a following beamtime at the *Elettra* synchrotron light source it was recognized that beam damage affects most VO_x structures massively within seconds, i.e. on a time scale too fast for AES. It turned out that the Auger spectroscopic calibration had been corrupted by beam damage, resulting in an underestimation of the surface V-content by a factor of about 2. Therefore, the coverages finally given in this thesis were estimated directly from microscopic images; details are explained in section 3.5 (discussion following figure 3.13). Absolute coverages Θ_V are denoted in monolayer equivalents (MLE), which corresponds to V atoms per Rh(111) atom.

2.4 Low energy electron diffraction (LEED)

The system Rh(111)/VO_x exhibits a large structural diversity (see section 3.1) [3, 4, 7]; the individual structures can be identified by LEED. Low energy electrons (30 – 300 eV) have wavelengths between 1 and 4 Å and are hence diffracted by atomic lattices. They penetrate only a few atomic layers, which makes them a surface-sensitive probe for structures. Since LEED is a standard method, just a brief description is given here; more detailed information can be found e.g. in [8].
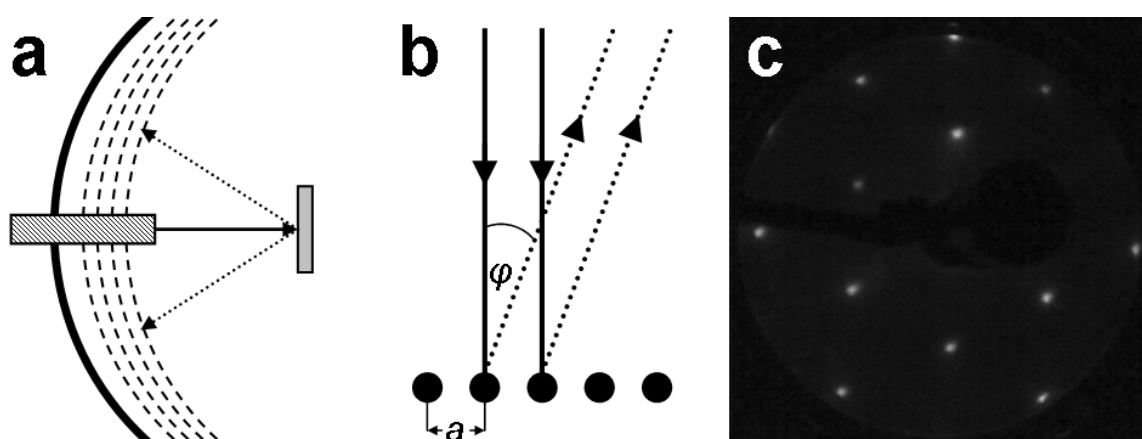

Figure 2.5: (a) Sketch of a 4-grid LEED optics with electron gun (shaded), screen (thick black line), grids (dashed), sample (grey), incident (arrow) and diffracted (dotted arrows) electron beam. (b) Diffraction in one dimension with diffraction angle φ and lattice constant a. (c) Diffraction pattern of Rh(111) at 140 eV; the photograph has been taken from behind the screen, the electron gun is visible in the center.

A typical LEED apparatus is constructed rather simply, as shown in figure 2.5 (a). An electron gun points towards the center of a hemispheric luminescent screen where the specimen is located. The screen is biased with about +5 kV to accelerate the electrons sufficiently to excite luminescence. Inelastically scattered electrons are discriminated by up to four retarding grids.

One can formulate a simple theoretical treatment in analogy to the Bragg treatment of x-ray diffraction by 3-dimensional lattices. Figure 2.5 (b) shows a sketch illustrating the scattering of an electron wave at a 1-dimensional periodic lattice, with *a* being the periodic distance between the scatterers (lattice constant) and φ the angle between incident and scattered electrons. Constructive interference occurs if the path difference of waves scattered at adjacent centers is a multiple of the wavelength, $n \cdot \lambda$:

$$a \cdot \sin\varphi = n \cdot \lambda \tag{2-1}$$

Extending this to two dimensions, one gets an array of scatterers which can be considered as a set of parallel rows with directions [*hk*] (Miller notation, [9, 8]) and equal distances d_{hk}. For that case, equation (2-1) becomes

$$d_{hk} \cdot \sin\varphi = n \cdot \lambda \quad \Rightarrow \quad \sin\varphi = \frac{n \cdot \lambda}{d_{hk}} \tag{2-2}$$

which yields the diffraction angle; the diffraction direction is perpendicular to [*hk*]. A single crystal surface can be constructed from different sets of parallel rows, each of them giving a diffracted beam. The geometry of a simple elementary cell can be deduced from the positions of a few beams, since the diffraction pattern is a representation of the reciprocal lattice, e.g. for Rh(111) in figure 2.5 (c). As in x-ray diffraction, evaluation of the intensities can give information about atomic positions within the elementary cell, but this rather complicated method was not applied within this work.

Since overlayers can be identified quickly by LEED, they are often denoted according to their structures. One example for such a notation frequently mentioned in chapter 3 is the $(\sqrt{7} \times \sqrt{7})R19.1°$-$VO_x$ overlayer on Rh(111): the notation indicates that both lattice constants are elongated by a factor of $\sqrt{7}$ with respect to the substrate and that the elementary cell is rotated by 19.1°, also with respect to the substrate. With chemical information attached, e.g. (2×1)-O for a chemisorbed oxygen overlayer on Rh(111), the so-called Wood notation is sufficient for most cases.

2.5 Auger electron spectroscopy (AES)

AES is the simplest method for surface-sensitive detection of the chemical composition. It was used to calibrate vanadium deposition rates (see section 2.3), and to check the surface for contaminants and identify those if necessary. As a standard technique it is also described here in brief; for detailed information see [8].
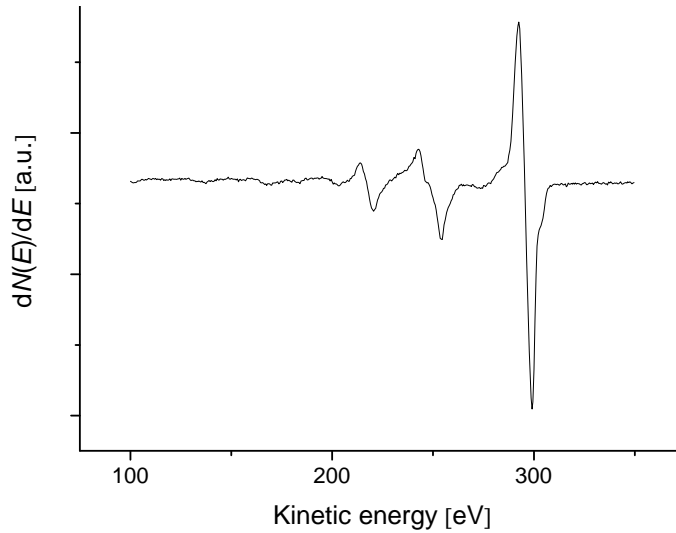

Figure 2.6: Partial Auger spectrum of clean Rh(111), representing the MNN-transitions due to initial excitation of the M-shell and relaxation/emission from the valence band. The derivative of the electron distribution $N(E)$ is plotted versus the kinetic energy of the electrons.

If an electron beam with an energy of a few keV impinges on a solid, core shell ionization will occur. The generated excited states relax either by emission of x-ray photons or via the so-called Auger process: an electron from a higher level fills the core hole, and the released energy is transferred radiationless to an outer electron which gets ejected. This so-called Auger-electron has a kinetic energy of

$$E_{kin} = E_{B1} - E_{B2} - \left(E_{B3} + \Phi\right) \tag{2-3}$$

with E_{B1} denoting the electronic binding energy of the electron initially expelled by the incident (primary) electron, E_{B2} that of the electron filling the core hole, and E_{B3} is the binding energy of the finally ejected one; since binding energies refer to the Fermi level E_F, also the work function Φ has to be taken into account. As can be seen from equation (2-3), the kinetic energy of the Auger electrons does not depend on the primary beam energy, but is characteristic for the transition. The corresponding peak in the spectrum, or a set of peaks for heavier elements, indicates the presence of an element on the

surface. At low coverages the intensity is proportional to the surface concentration (see section 2.3).

Since the Auger peaks are small compared to the secondary electron background, advanced instrumentation is required for sensitive detection. The typical setup used here consists of a cylindrical mirror analyzer with a channeltron detector and a coaxial electron gun; the sensitivity is further increased by lock-in amplification [8]. This way the derivative of the actual spectrum $N(E)$ is obtained electronically, as can be seen in figure 2.6, where a partial spectrum of clean rhodium is presented as an example. The detection limit is about 0.1 % of a monolayer.

2.6 X-ray photoelectron spectroscopy (XPS)

During additional measurements at the synchrotron light source *Elettra* in Trieste/Italy, XPS was available for surface-sensitive analysis of the chemical composition. This method is described here briefly; for detailed information the reader is once again referred to [8]. Being a core-level spectroscopy like AES, the main advantage of XPS is the chemical shift of the binding energies, which in principal allows the determination of oxidation states.

The technique is based on the photoelectrical effect: x-radiation is focused on the sample, either from an x-ray tube or a synchrotron light source. Excitation occurs to all electronic levels energetically accessible to the primary beam. In the surface region photoelectrons can leave the solid without further interaction and thus have kinetic energies defined by

$$E_{kin} = h\nu - \left(E_B + \Phi \right) \qquad (2.4)$$

with h being Planck´s constant and ν the photon frequency. As in equation (2-3) the electronic binding energy E_B refers to E_F, so Φ is included.

The usual instrumentation is, besides an x-ray source, a concentric hemispherical electron analyzer with a channeltron detector to count photoelectrons. Here the energy filter of a LEEM apparatus (see section 2.8) and its imaging detector were used, so the light intensity is plotted against E_B, yielding a spectrum. An example from a Rh(111)/Ni/NiO composite surface is presented in figure 2.7; the partial spectrum

containing the photoelectrons emitted from the $2p_{3/2}$ core level of nickel is displayed. Like in most XP-spectra the peaks corresponding to different states exhibit significant overlap, which is the reason why the spectrum is *fitted*: evaluation usually involves the decomposition of the spectrum into components. First a secondary electron background is defined according to Shirley's method [10], and then peaks (components) are added. The spectrum in figure 2.7 could be fitted with three peaks: one for metallic Ni, and two for NiO (from right to left).
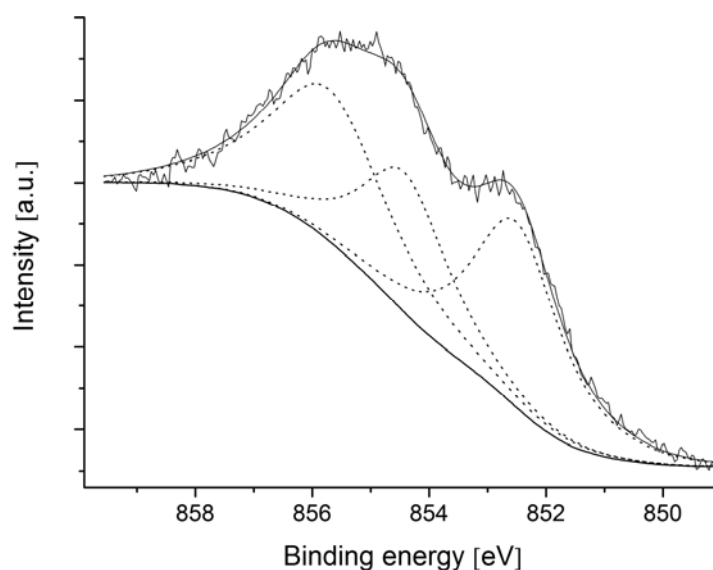
Figure 2.7: Fitted $Ni2p_{3/2}$ XP-spectrum, photon energy = 982 eV; a Shirley background (solid line beneath spectrum) and three components (dotted lines) are indicated. The smooth solid line running along the noisy spectrum is the sum of background and components (the "fit").

For representation of the peaks Lorentzian-Gaussian convolution (Voigt) functions should be used, since the intrinsic lifetime width of the core-level hole state results in a Lorentzian line shape, while instrumental broadening is assumed to give a Gaussian contribution. For computational reasons XPS-fitting programs approximate true Voigt functions by Lorentzian-Gaussian (LG) combination functions. Throughout this work the LG product function was used [11], with constant LG-ratios within each spectrum. The fitting procedure is to put as many components as needed onto the background and to fix as many parameters as possible (e.g. peak positions, widths, chemical shifts) to known or assumed values. The remaining parameters are left open as fitting variables, and a least-squares optimization can be started. The result of such a procedure is to be judged critically if no reference data recorded on the same instrument is available; usually many parameters are unknown and thus open as fitting variables,

and each additional degree of freedom improves the fit, regardless of physical reality. The freeware program *XPSPeak* [12] was used for fitting.

2.7 Photoemission electron microscopy (PEEM)

PEEM is the main method of this work. The basic idea is to use the work function Φ, which is very sensitive to the surface chemical composition [13], to monitor surface concentrations *in situ*, in real time and spatially resolved. For this purpose the sample is illuminated with UV-light, and the resulting photoelectrons are imaged through a system of electrostatic lenses onto a detector. Two effects are exploited to gain work function contrast: on the one hand, the photoelectron current (and thus the PEEM intensity I) depends on Φ according to Fowler's law [14]

$$I \sim \left(h\nu - \Phi\right)^2 \qquad\qquad\qquad (2\text{-}5)$$

provided that $h\nu > \Phi$ (otherwise $I = 0$). On the other hand a deuterium discharge lamp (D 200 F, Heraeus Noblelight) is used as light source, which does not emit an isolated UV line, but a continuous spectrum (maximum intensity at 6.2 eV); this leads to more photons with $h\nu > \Phi$ at lower Φ. Since both effects add up to produce high intensity at a low work function, small changes of Φ strongly affect I. Thus changes and differences are visualized with high contrast in PEEM images, regions with low Φ appearing bright and regions with high Φ dark. The major drawback of this effective contrast mechanism is that the origin of Φ differences is usually unknown and hence additional information is required to interpret PEEM data in terms of chemistry. Moreover, a calibration is needed for quantitative Φ measurements.

A sketch of the microscope [1] is displayed in figure 2.8. As indicated there, the main body is biased to a high positive potential (for this work instead of 20 kV just $12 - 14$ kV were used to prevent discharges at high pressures), so the electrons are accelerated into the microscope. A three-lens optics (objective, intermediate- and projector lens) produces a magnified image, then the electrons are slowed down in the drift tube to hit the detector with an appropriate energy. A microchannel plate (operated with 1 kV) multiplies the electrons, which are then accelerated again to 5 keV onto a luminescent phosphor screen, producing the visible image.
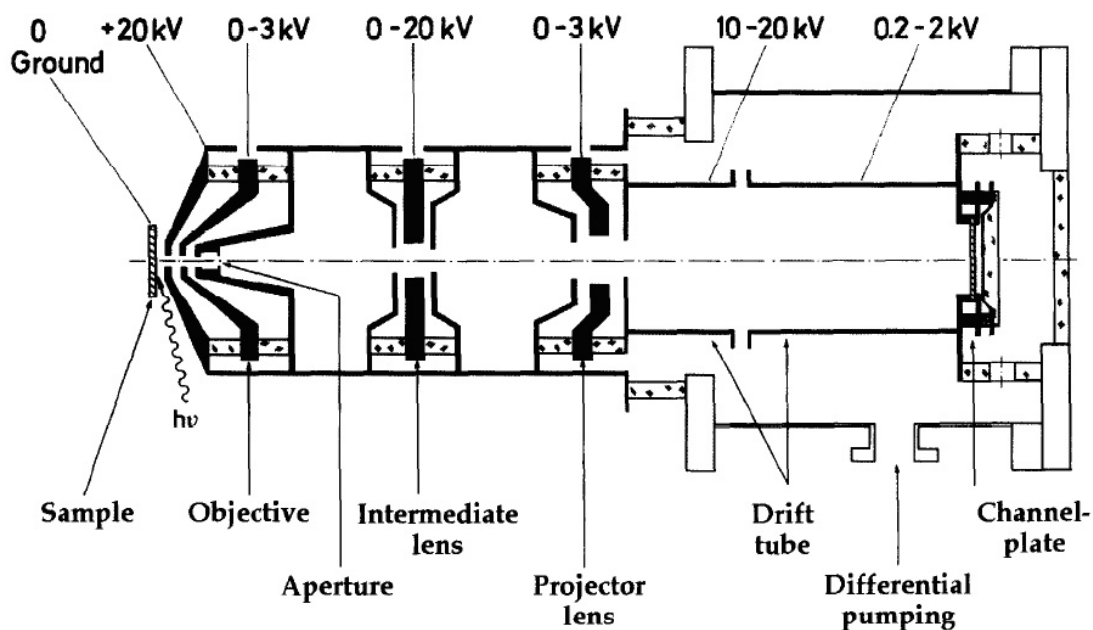
Figure 2.8: Sketch of the photoemission electron microscope designed by Engel [1]. The electrons travel from the sample (left) to the detector (right). They pass by all the indicated electrostatic lenses, yielding a magnified image of the local work function. Reproduced according to the GNU public license regulations.
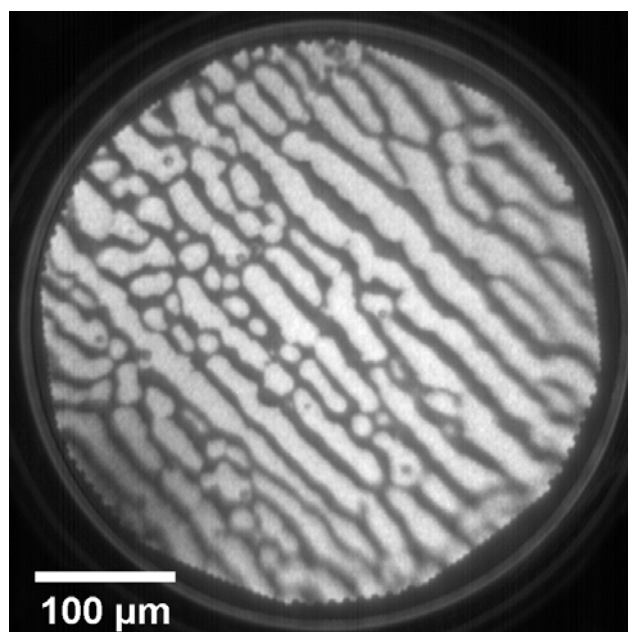

Figure 2.9: Example PEEM image of a typical VO_x stripe pattern on Rh(111) formed under reaction conditions at $\Theta_V = 0.2$ MLE, $p(O_2) = 1.25 \cdot 10^{-5}$ mbar, $p(H_2) = 4 \cdot 10^{-6}$ mbar, $T = 500°C$. The oxide appears dark, in contrast to the area in between where only traces of V are present. The image is blurred at the right and lower rim, due to aberrations at large FOV.

The lateral resolution of the instrument is ~1 μm, fields of view (FOV) between 100 and 500 μm can be adjusted. With differential pumping operation at pressures up to

10^{-3} mbar is possible, and since there is no direct connection between microscope and specimen (5 − 10 mm distance), high sample temperatures can be handled.

The image on the phosphor screen was captured by a video camera connected to the TV-adapter of a PC, where the video-processing freeware-program *VirtualDub* [15] was used to record the data. This was performed without any video compression at frame rates between 1 and 25 frames/s. For evaluation and presentation, images or movies were processed with *VirtualDub* [15] or *Giotto* [16]; usually several frames were averaged for noise reduction, and the contrast was optimized. More advanced evaluation (grey level scans, image calculations) were performed with *ImageJ* [17]. An example for a PEEM image is displayed in figure 2.9, showing a typical stripe pattern formed by vanadium oxide (dark = high Φ) on Rh(111) under $H_2 + O_2$ reaction conditions.

2.8 Low energy electron microscopy (LEEM) and related techniques

The additional structural and chemical information required for interpretation of PEEM data was collected using LEEM instruments. One is located in Clausthal at the group of Lilienkamp, which was available for a few days of measurements. The majority of data was obtained during a beamtime at the synchrotron light source *Elettra* in Trieste/Italy. At the *Nanospectroscopy* station a LEEM is attached to a beamline, which gives the instrument a great variety of modes of operation that shall be described in the following.

LEEM was developed by Telieps and Bauer and introduced in 1985 [18]. The basic idea is to combine LEED with high-resolution real-space imaging, using reflected electrons. The company Elmitec offers instruments mounted in especially designed UHV chambers, which were used for this work (*LEEM III*). In addition to the microscope, those chambers are equipped with an ion gun for sputtering, QMS and *in situ* metal evaporators, allowing real-time observation of thin film growth. A simplified schematic representation of the microscope is given in figure 2.10, details can be found in [19].

The imaging electrons are generated by a lanthanum boride single-crystal cathode biased on -18 kV, and are hence accelerated through some beam alignment lenses (not shown in figure 2.10) towards the magnetic sector field. In contrast to the PEEM with its electrostatic lenses (see section 2.7), magnetostatic lenses are used in LEEM. The sector field deflects the beam towards the specimen which is also biased on

-18 kV plus an additional voltage ΔU between 0 and a few hundred V, so that the electrons are decelerated to reach the surface with typical LEED energies (< 500 eV). After reflection/diffraction there, the electrons are accelerated back into the microscope. A diffraction image is obtained in the back focal plane of the objective lens, corresponding to a LEED pattern at the energy $e \cdot \Delta U$. Traveling onward through the collimator lens (CL in figure 2.10) into the sector field, the electrons are imaged on the intermediate image plane to give a real-space representation of the surface. The image undergoes such transformations from reciprocal to real space and vice versa 13 times between the back focal plane and the detector (MCP), of which just 3 are indicated in figure 2.10. The sector field deflects the beam into the imaging column, where again behind a transfer lens (TL) a diffraction pattern is produced; an intermediate lens (IL) images the beam into the energy filter, which removes inelastically scattered electrons. Finally projector lenses (PL) image the result onto a microchannel plate detector (MCP), where it is captured by a CCD camera and stored on a PC.
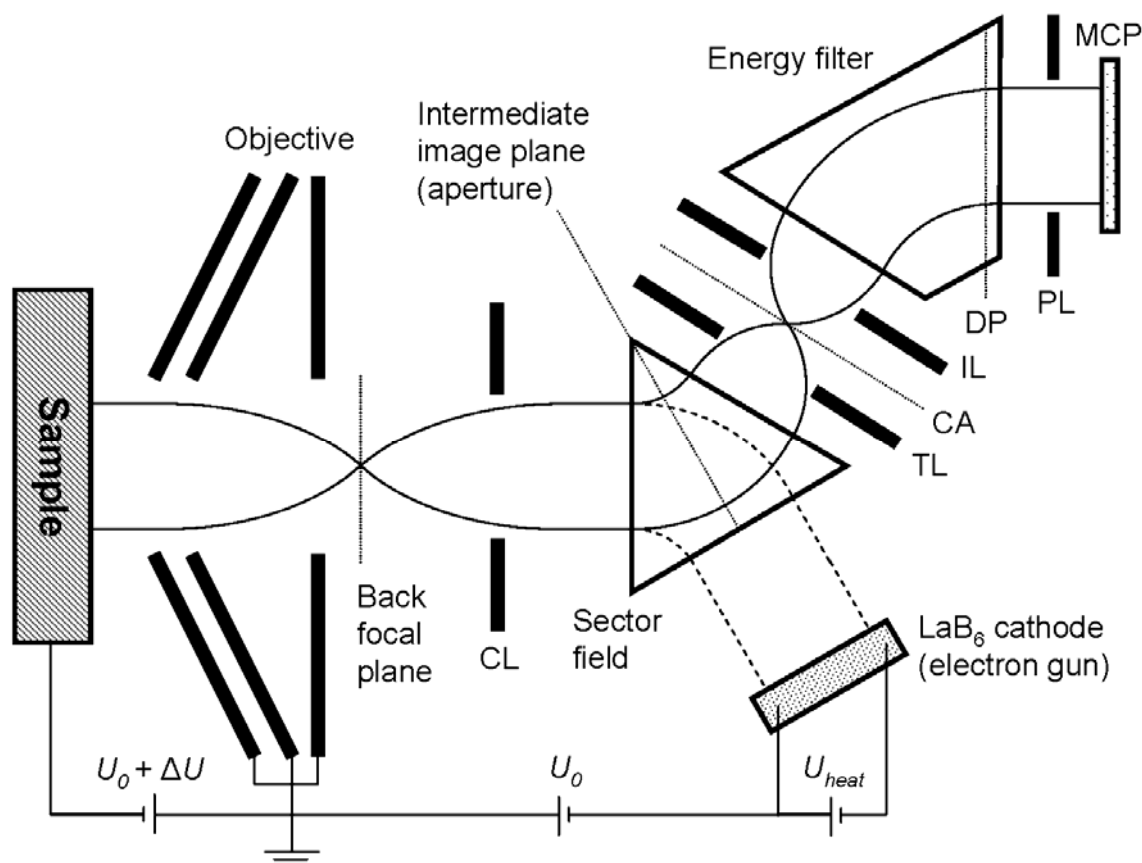

Figure 2.10: Simplified schematic representation of a LEEM. Many electron-optical components are omitted, as well as details of the optical path. For explanation, see text. MCP = microchannel plate, PL = projector lens, DP = dispersive plane, IL = intermediate lens, CA = contrast aperture, TL = transfer lens, CL = collimator lens, U_0 = 18 kV.

The standard mode of operation is bright-field LEEM. An aperture (contrast aperture, CA) is inserted into a diffraction plane (see figure 2.10) to select the (00)-beam of the LEED pattern for imaging. Contrast arises from local differences in reflectivity for electrons of certain energy. Atomic steps can be visualized as dark lines resulting from *Fresnel diffraction* [18]: if the height of a step is $\lambda/2$ (with λ being the wavelength of the electron beam), the reflected electron waves from adjacent terraces have a path difference of $\lambda/2$, leading to destructive interference at steps. By varying ΔU and thus λ, step heights can be measured.

If ΔU is adjusted to slightly negative values, the electrons cannot reach the surface, but are reflected at an equipotential plane in front of the specimen. Contrast thus arises from the topography and the local work function [20]. This mode of operation is called MEM (mirror electron microscopy) and exhibits work function contrast as in PEEM, but contrary to that, regions with high Φ appear bright in MEM.

The contrast aperture (CA in figure 2.10) can also be used to select beams from the diffraction pattern other than (00) for imaging. This is useful if the surface is partially covered with an adlayer producing additional spots in LEED. If such a beam is selected, only the corresponding regions appear bright. Even the spatial distribution of rotational domains can be visualized this way. This contrast mechanism is called dark-field LEEM.

LEED patterns can be obtained by adjusting the intermediate lens (IL) to image a diffraction pattern instead of a real space image plane onto the following projector system. Of course the contrast aperture (CA) has to be removed. The field limiting aperture can be inserted into the intermediate image plane instead (see figure 2.10), which allows to select areas between 2 and 30 μm in real space for electron diffraction. This technique is called μ-LEED.

Instead of the electron beam, soft x-ray light is available at *Elettra* to illuminate the sample, which allows surface chemical characterization. In the imaging mode x-ray photoemission electron microscopy (XPEEM) can be performed. The energy filter and a retarding voltage (ΔU) define the kinetic energy of the imaged photoelectrons: if a binding energy of an XPS peak is selected then, the lateral distribution of the corresponding element is imaged. To record an actual XP-spectrum, the exit slit of the energy filter is opened completely, and the projector lenses (PL) are adjusted to image the energy dispersive plane (DP in figure 2.10) onto the detector. A 10 eV wide section of the spectrum appears as a line, with its brightness being proportional to the intensity. The energy section is chosen by adjusting the retarding field (ΔU). Additionally, a

region of the sample can be selected by putting an aperture into the intermediate image plane as in μ-LEED. This way μ-XPS is possible. The binding energy scale is calibrated to either the Fermi edge or a peak with fixed position; an accuracy of ± 0.2 eV is estimated. The recording geometry is fixed to normal emission and grazing incidence at 16°.

The lateral resolution of the instrument is limited to 20 to 50 nm, depending on the mode of operation. This is more than one order of magnitude better than in conventional PEEM (~1 μm), but on the downside the field of view is limited to ~60 μm. Another drawback is the working pressure limit in the 10^{-6} mbar range. A further disadvantage of the LEEM systems is a lack of accuracy in temperature readout (± 25 K) and control (manual adjustment of indirect heating).

The images have been processed like described for PEEM (see section 2.7). Additionally, the commercial program *IGOR Pro* [21] was used to read out line profiles and to normalize images. Normalization means that an image is divided by another one which displays only the inhomogeneities of the detector, which are removed this way from the original image. In case of dispersive plane images this is absolutely necessary to read out an XP-spectrum.

2.9 References

[1]   W. Engel, M. E. Kordesch, H. H. Rotermund, S. Kubala, A. von Oertzen, *A UHV-compatible photoelectron emission microscope for applications in surface science*, Ultramicroscopy 36 (1991), 148.

[2]   J. T. Grant, T. W. Haas, *A study of Ru(0001) and Rh(111) surfaces using LEED and Auger electron spectroscopy*, Surf. Sci. 21 (1970), 76.

[3]   J. Schoiswohl, M. Sock, S. Eck, S. Surnev, M. G. Ramsey, F. P. Netzer, G. Kresse, *Atomic-level growth study of vanadium oxide nanostructures on Rh(111)*, Phys. Rev. B 69 (2004), 155403.

[4]   J. Schoiswohl, S. Surnev, F. P. Netzer, G. Kresse, *Vanadium oxide nanostructures: from zero- to three-dimensional*, J. Phys. Condens. Matt. 18 (2006), R1.

[5]   J. P. Biberian, G. A. Somorjai, *On the determination of monolayer coverage by Auger electron spectroscopy. Application to carbon on platinum*, Appl. Surf. Sci. 2 (1979), 352.

[6]   F. Lovis, M. Hesse, R. Imbihl, *Redistribution of Supported Vanadium Oxide Catalysts by Pattern Formation*, Catal. Lett. 136 (2010), 171.

[7]   J. Schoiswohl, S. Surnev, M. Sock, S. Eck, M. G. Ramsey, F. P. Netzer, G. Kresse, *Reduction of vanadium-oxide monolayer structures*, Phys. Rev. B 71 (2005), 165437.

[8]   G. Ertl, J. Küppers, *Low Energy Electrons and Surface Chemistry*, VCH, Weinheim 1985.

[9]   N. W. Ashcroft, N. D. Mermin, *Festkörperpysik*, Oldenbourg, München 2005.

[10]   D. A. Shirley, *High Resolution X-Ray Photoemission Spectrum of the Valence Bands of Gold*, Phys. Rev. B 5 (1972), 4709.

[11]   S. Evans, *Curve Synthesis and Optimization Procedures for X-ray Photoelectron Spectroscopy*, Surf. Interf. Anal. 17 (1991), 85.

[12]   R. W. M. Kwok, *XPSPeak 4.1* (1999).

[13]   K. Christmann, *Introduction to Surface Physical Chemistry*, Steinkopf/Springer, Darmstadt/Berlin 1991.

[14]   R. H. Fowler, *The Analysis of Photoelectric Sensitivity Curves for Clean Metals at various Temperatures*, Phys. Rev. 38 (1931), 45.

[15]   A. Lee, *VirtualDub 1.9.7* (2009).

[16]   Dittelsoft, *Giotto 2.1.2* (2007).

[17]   W. Rasband, *ImageJ 1.42q* (2009).

[18]   W. Telieps, E. Bauer, *An Analytic Reflection and Emission UHV Surface Electron Microscope*, Ultramicroscopy 17 (1985), 57.

[19]   T. Schmidt, S. Heun, J. Slezak, J. Diaz, K. C. Prince, G. Lilienkamp, E. Bauer, *SPELEEM: Combining LEEM and Spectroscopic Imaging*, Surf. Rev. Lett. 5 (1998), 1287.

[20]   W. Swiech, B. Rausenberger, W. Engel, A. M. Bradshaw, E. Zeitler, *In situ studies of heterogeneous reactions using mirror electron microscopy*, Surf. Sci. 294 (1993), 297.

[21]   WaveMetrics, *IGOR Pro 6.1.2.1* (2009).

3. Vanadium oxide on Rh(111)

The first part of this work deals with the behavior of sub-monolayer coverages of vanadium oxide under reaction conditions. The central finding is that VO_x is redistributed on the surface: under exposition to the $H_2 + O_2$ reaction under certain conditions non-equilibrium (quasi-) stationary structures form. These were studied in detail, along with further properties of the inverted model catalyst.

3.1 Growth and structures of VO_x overlayers on Rh(111)

The deposition of ultra-thin VO_x layers on Rh(111) has been investigated extensively in the group of Netzer by scanning tunneling microscopy (STM) as main method [1−7]. Some new information obtained by LEED and LEEM is presented here, along with a short survey of the structures which are of importance for this study.

The substrate itself, the (111)-face of rhodium, can be considered as a plane of closest packed spheres: each Rh atom is surrounded by a hexagon of 6 nearest neighbors in plane, as illustrated in figure 3.1a. The hexagonal diffraction pattern of Rh(111) is shown in figure 2.5. The substrate exerts a structure-directing influence on adsorbed overlayers and can serve as a template, leading to the formation of coincidence structures which can be referenced to the substrate (see section 2.4). Such ultra-thin film structures usually have no bulk analogs and thus may exhibit unexpected properties.

If vanadium is deposited like described in section 2.3 (400°C, $2 \cdot 10^{-7}$ mbar O_2) there is enough adsorbed oxygen present on the surface to readily oxidize V to its highest possible oxidation state, +5. Two V^{5+}-oxide sub-monolayer structures are known on Rh(111) [1], the already mentioned $(\sqrt{7} \times \sqrt{7})$R19.1° (referred to as $\sqrt{7}$ hereafter) and a similar one, $(\sqrt{13} \times \sqrt{13})$R13.8° (called $\sqrt{13}$). Structural models have been developed for both, based on STM measurements and simulations by density functional calculations [1]; an illustration of the $\sqrt{7}$-structure is reproduced in figure 3.1 (a). The unit cell and the basic building block are indicated: the overlayer consists of $O_4V{=}O$ pyramids, with oxygen always connecting V to Rh and an additional vanadyl-oxygen on top of each V atom. This results in an O-V-O trilayer of VO_3 stoichiometry, which is not in conflict with the V^{5+} oxidation state, since most O atoms also bind to the substrate.

In figure 3.1 (c) the $\sqrt{7}$ LEED pattern is displayed. It consists of two energetically equivalent rotational domain structures; the reciprocal elementary cells of both are indicated (dashed/dotted lines), as well as the one of the substrate. An analogous representation for the $\sqrt{13}$-structure is given in figure 3.1 (d), where additionally a (2×2)-pattern is superimposed (encircled beams), originating from oxygen atoms chemisorbed on V-free Rh(111) regions [9]. The model for the $\sqrt{13}$-structure is not presented here, because it is quite similar to the $\sqrt{7}$-structure: the $O_4V=O$ pyramids are arranged slightly more dense, resulting in 0.46 V atoms per Rh, instead of 0.43 for the $\sqrt{7}$-structure.
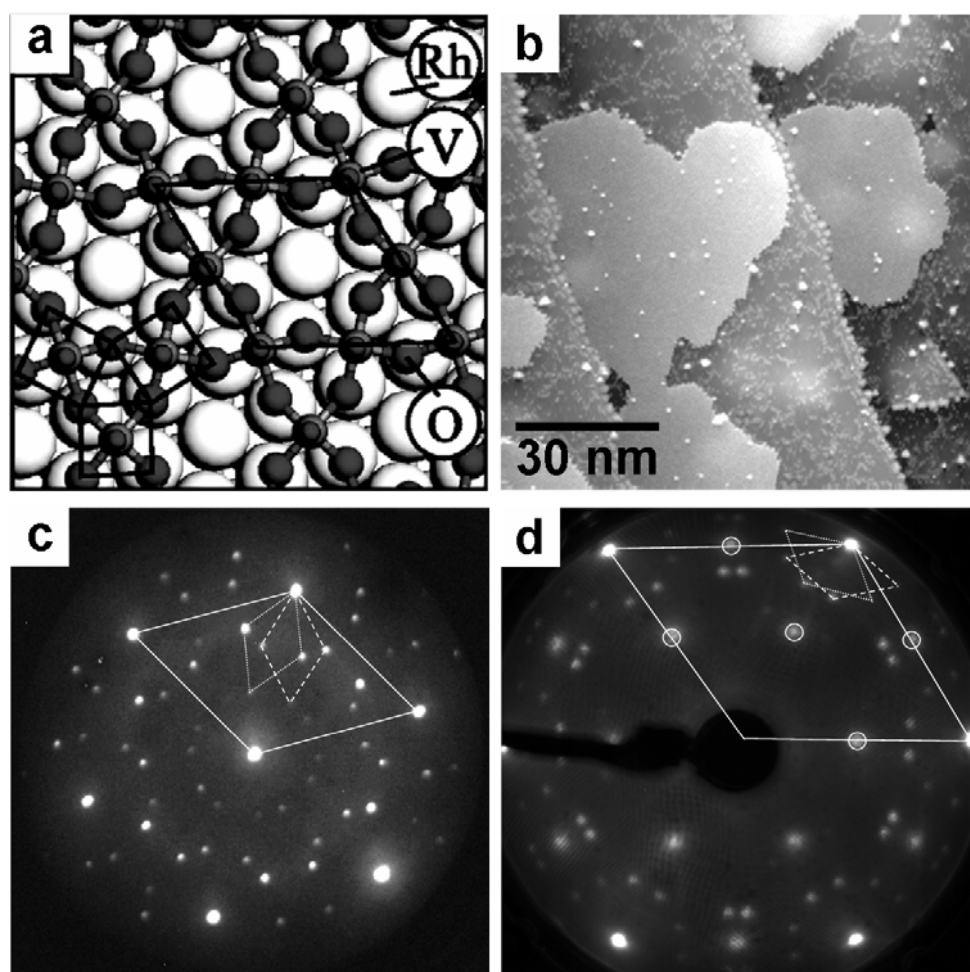
Figure 3.1: (a) Schematic representation of the $(\sqrt{7} \times \sqrt{7})R19.1°$-structure, reproduced with permission from [3]. Bright spheres represent Rh atoms and light grey ones V atoms, which are always underneath of O atoms (dark spheres). (b) STM micrograph (100 x 100 nm^2) of islands of the $\sqrt{7}$-structure, 0.15 MLE, reproduced with permission from [1]. (c) $(\sqrt{7} \times \sqrt{7})R19.1°$ LEED pattern, recorded at 50 eV with a LEEM instrument. The unit cells of the two rotational domains are indicated (dashed and dotted), as well as the one of the substrate. (d) $\sqrt{13} \times \sqrt{13} R13.8°$ LEED pattern at 57 eV with 0.25 MLE VO_x. Additionally a (2×2)-O pattern [9] is superimposed, the half-order spots are encircled.

In figure 3.1 (b) an STM micrograph (100 x 100 nm^2) of the $\sqrt{7}$-structure is displayed: 0.15 MLE vanadium oxide were deposited in the usual manner (400°C, $2 \cdot 10^{-7}$ mbar O_2), resulting in 2-dimensional island growth [1]. Additional information on the growth process was gathered during a calibration experiment in LEEM (see figure 3.3), but prior to discussing that some more vanadium oxide structures have to be introduced.

A couple of reduced monolayer VO_x structures is known on Rh(111). Starting with a $\sqrt{7}$-structure, reduction (10^{-9} mbar H_2, 400°C, [3, 6]) yields a sequence of oxides with lower oxygen content. First a (5×5)-$V_{11}O_{23}$ layer (0.44 V atoms per Rh) is formed, followed by a $V_{13}O_{21}$ structure denominated ($5 \times 3\sqrt{3}$)-rect (0.43 V/Rh); both are mixed-valence oxides with decreased vanadyl (V=O) content. Upon further reduction all vanadyl-oxygen atoms are removed, leaving first a (9×9)-V_2O_3 overlayer (0.44 V/Rh) and after that a VO layer denoted as "wagon wheel"-structure with 0.73 V/Rh [3]. Two further structures have been reported, both not as part of the reduction sequence, but during oxide growth [1]. One denoted as the "oblique phase" actually consists of two different incommensurate structures observed together in STM, for which no structure models are available; it is only known from vibrational spectroscopy that vanadyl groups are present [1]. Another oxide layer observed during growth, a so-called Moiré structure [1], has a VO_2 stoichiometry and a high density of 0.85 V/Rh. This structure will be introduced in detail at the end of this section.

Out of this diverse group of structures just the (9×9)-V_2O_3 overlayer is displayed in figure 3.2, since it is of particular interest for this work. It is shown in section 3.4 that under reaction conditions a (2×2)-VO_x monolayer structure forms which has not been observed on flat Rh(111) before. (2×2)-V_2O_3 monolayers are known to grow on Pd(111) [11] and on Rh(15 15 13), which is a stepped surface featuring (111) terraces [8]. On those a (2×2)-overlayer is formed instead of (9×9)-V_2O_3. In figure 3.2 it is illustrated that the two structures are indeed very similar, being both composed of the same hexagonal V_6O_{12} building units (encircled). The (9×9) unit cell even contains a section with local (2×2) symmetry, indicated as a hexagon in figure 3.2 with (2×2) unit cells inside (which are identical with (2×2)-V_2O_3 on Pd(111) [6]). Both structures have the same stoichiometry, but the density of a (2×2)-overlayer (0.5 V/Rh) is significantly higher compared to (9×9)-V_2O_3 (0.44 V/Rh). Formation of the (9×9)- instead of the (2×2)-structure on Rh(111) probably compensates a slight lattice mismatch [8].
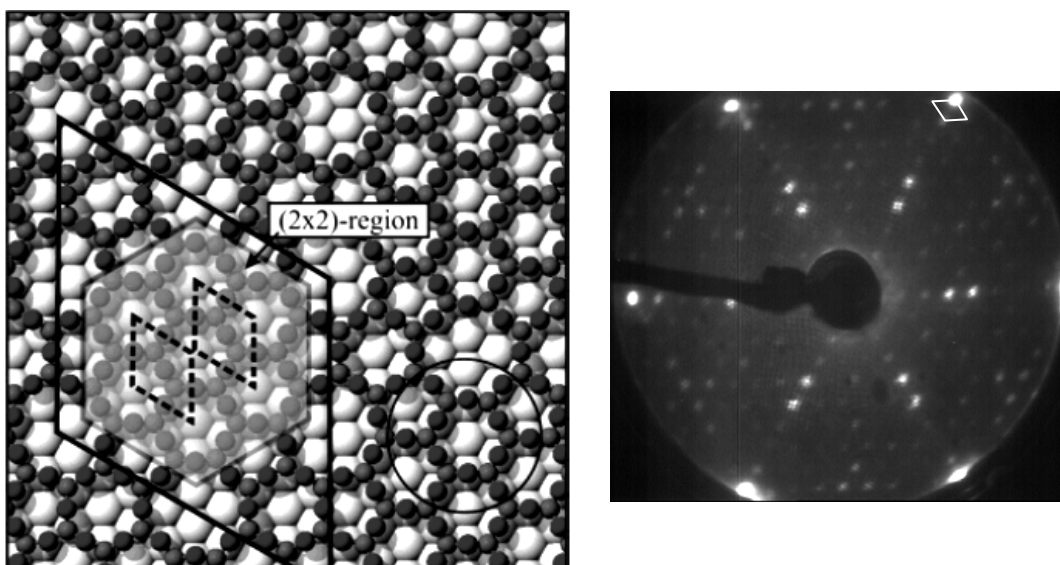
Figure 3.2: DFT-derived model of the (9×9)-V$_2$O$_3$ overlayer on Rh(111), reproduced with permission from [8]. Rh is represented by white spheres, V by medium grey and O by dark spheres. Additionally a V$_6$O$_{12}$ building unit (circle), the (9×9) unit cell and a region with local (2×2) geometry (hexagon with small dashed (2×2) unit cells) are indicated. On the right side the (9×9) LEED pattern is displayed, recorded at 64 eV; a (9×9) reciprocal unit cell is indicated.

Vanadium was deposited under the microscope at the usual conditions while recording a movie of the growth process; some selected frames are displayed in figure 3.3. The LEEM images can be interpreted in the context of an STM growth experiment conducted under similar conditions [1]. In contrast to here, vanadium was deposited in increments in the STM experiment, and after each increment the surface was scanned. Additional details are revealed here due to *in situ* evaporation.

The first image in figure 3.3 (0.013 MLE) was recorded right before visible structures nucleate, so the only contrast is caused by heavily stepped regions (step bunches) appearing as dark wavy lines. The three black spots and the shady blotches (better visible at 0.43 MLE) are artifacts from detector damage. Two subsequent images (0.031 and 0.141 MLE) show the nucleation and growth of VO$_x$ along step bunches; in the latter image the oxide starts to spread onto terraces (encircled).

In separate LEED experiments it was found that both V^{5+} structures, $\sqrt{7}$ or $\sqrt{13}$, can grow under the given p(O$_2$) and temperature conditions, depending on the deposition rate. At 0.4 MLE/hour the $\sqrt{7}$-structure was observed exclusively, while slower evaporation (0.15 MLE/hour) leads to mixed growth. This coincides with the finding that the $\sqrt{13}$-structure is thermodynamically stable under these conditions, while $\sqrt{7}$-growth is kinetically favored [1]. As vanadium was deposited at 0.53 MLE/hour in

figure 3.3, the $\sqrt{7}$-oxide grows exclusively. This was also observed in the STM experiment where much higher deposition rates (0.2 MLE/min) were applied [1]. The different rate has consequences for the growth morphology: while at slow evaporation a few large islands grow at the step bunches (see figure 3.3), much smaller islands are observed in the STM experiment, growing on terraces (see figure 3.1 (b)).
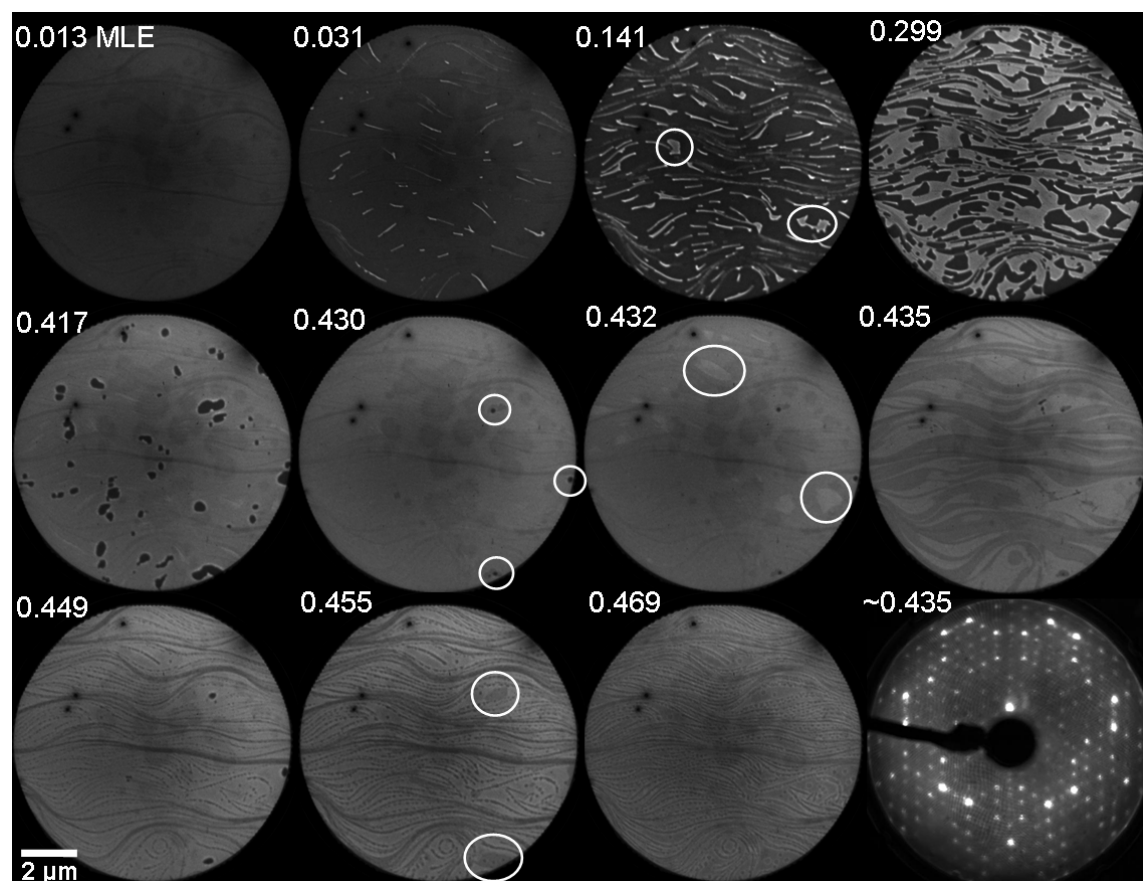

Figure 3.3: Sequence of LEEM images (11 eV) illustrating the growth of VO$_x$ on Rh(111) at 400°C, $2 \cdot 10^{-7}$ mbar O$_2$, during ~50 min; for further explanation see text. The coverage is given for every image. Some features which appear in every image, i.e. the three black spots and some shady blotches, are artifacts from detector damage. The last image is a LEED pattern (50 eV) from a separate growth experiment under similar conditions (unpublished work of M. Hesse).

In the following images the $\sqrt{7}$-oxide continues to cover the surface until completion of a full wetting layer (except three little holes, encircled). Consequently, the coverage is assigned to be 0.43 MLE at that point, since the $\sqrt{7}$ unit cell contains 0.43 V atoms per Rh. This assignment is the basis of the coverages given for LEEM experiments.

After completion of the wetting layer, instead of nucleation of a second layer a sequence of surface transformations is observed, combined with decoration of steps.

Apparently the surface reacts to further vanadium deposition by incorporation of V into the first layer, forming reduced oxide structures of higher V-density. Almost immediately (0.432 MLE in figure 3.3) a brighter structure nucleates on the flat parts of the surface (encircled) and covers the area quickly via propagating fronts (0.435 MLE, 20 s later), before step bunches get decorated. This decoration appears in LEEM in form of dark dots (0.449 MLE). Upon further deposition another structure nucleates (0.455 MLE, encircled) and covers the terraces via dark fronts (completed at 0.469 MLE). The holes which are visible since 0.43 MLE (encircled) seem to act as nucleation centers; most likely they represent surface inhomogeneities/defects.

The formation of dark dots at the step bunches can be explained according to [1], where the formation of hexagonal "tiles" was observed at the steps. Those turned out to be a Moiré-VO_2 structure (for details see below).

The structures developing on the terraces cannot be identified clearly. As mentioned above, an "oblique phase" was observed together with the Moiré-VO_2 tiles in the STM growth experiment [1], between completion of the wetting layer and the onset of 3D growth. That "oblique phase" is apparently an intermediate compression layer which is consequently not observed upon reduction at lower coverage [3, 6]. In analogy with the STM study it is assumed that the structure which nucleates at 0.455 MLE and appears dark in LEEM, is the "oblique phase".

After completion of the wetting layer the $\sqrt{7}$-structure is quickly transformed into an overlayer appearing bright in LEEM (0.432 MLE in figure 3.3). An indication for the identity of this structure was found by M. Hesse during a separate growth experiment (unpublished). This was conducted at 400°C and $2 \cdot 10^{-7}$ mbar O_2, evaporating vanadium in increments and recording LEED patterns. LEED reveals that the $\sqrt{7}$-structure is replaced by the (9×9)-V_2O_3 structure, as indicated by the presence of both diffraction patterns in figure 3.3 (bottom right image). Since the conditions are the same as in the LEEM experiment, except for faster deposition (~0.15 MLE/min), the bright overlayer is assigned to (9×9)-V_2O_3. The transformation of the $\sqrt{7}$-structure into the (9×9)-oxide allows the uptake of additional vanadium into the first layer, because the V-density of the (9×9)-oxide is slightly higher (0.44 V/Rh) than that of the $\sqrt{7}$-structure (0.43 V/Rh). With further V incorporation the Moiré "tiles" (0.85 V/Rh) develop at 0.449 MLE. The intermediate (9×9) overlayer was probably overlooked in the STM study due to incremental deposition [1].

In LEEM as well as in STM [1] the Moiré structure occurs as one of the reduced intermediate structures leading from 2- to 3-dimensional growth, covering only a small fraction of the surface. Apparently the Moiré structure is not mentioned in later literature anymore, which might lead to the impression that it only forms as a minor product under delicate coverage conditions. However, the opposite is true: during the experiments for this work it was observed regularly, often as the only VO_x structure present. The Moiré LEED pattern displayed in figure 3.4 (a) was recorded after deposition of $\Theta_V = 0.82$ MLE and an O_2 treatment at $5 \cdot 10^{-6}$ mbar and 600°C. Another Moiré structure forms at lower coverages and high O_2 pressure ($4 \cdot 10^{-5}$ mbar, 500°C, 0.2 MLE), as displayed in (b).
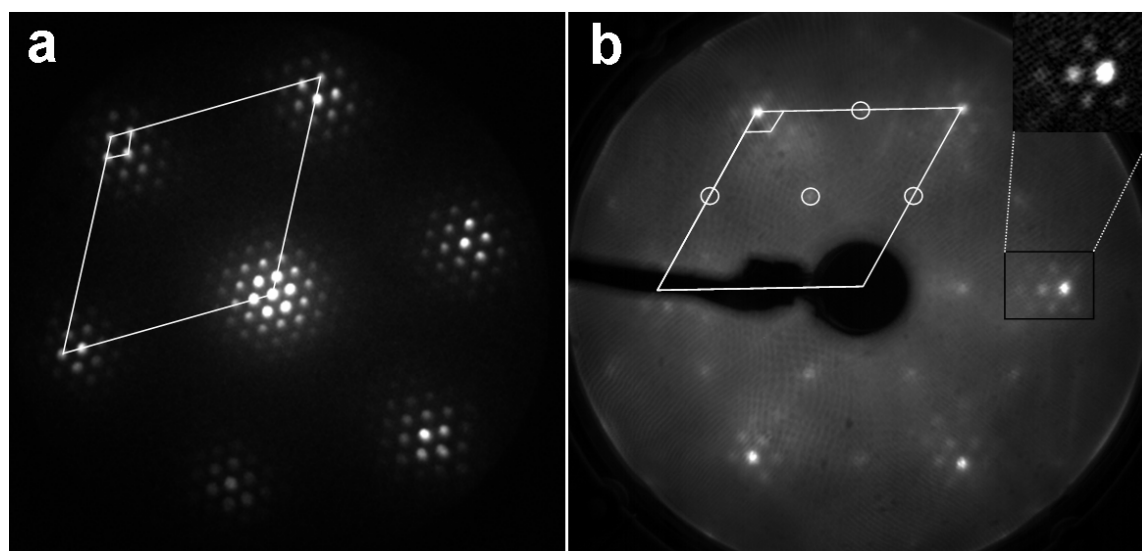
Figure 3.4: (a) LEED pattern of the high coverage Moiré structure recorded at 42 eV with a LEEM instrument. The surface was prepared with $\Theta_V = 0.82$ MLE and oxidation at 600°C, $5 \cdot 10^{-6}$ mbar O_2. (1×1) and (12×12) unit cells are indicated. (b) LEED pattern of the low coverage Moiré structure recorded at 100 eV with a conventional LEED instrument. The surface was prepared with $\Theta_V = 0.2$ MLE and oxidation at 500°C, $4 \cdot 10^{-5}$ mbar O_2. (1×1) and (9×9) unit cells are indicated, additional (2×2)-spots are marked with circles. The inset was strongly modified in contrast and reveals more detail than the original image.

The term "Moiré structure" originates from the optical "Moiré effect", which describes the appearance of long-range modulations if patterns with different periodicities are superimposed. In chemistry this is known from graphene layers on hexagonal surfaces, e. g. Rh(111) [10], resulting in diffraction patterns very similar to those in figure 3.4. The VO_x Moiré structure reported in [1] is assigned to be analogous to the VO_2-hex structure known from Pd(111) [11], which is an O-V-O stack of

hexagonally close packed O- and V-layers growing pseudomorphously on Pd(111). Due to the small mismatch (~2 %) between the Rh and Pd lattice constants this is not possible on Rh(111), resulting in a Moiré structure. Derived from STM data the coincidence lattice is ($\sqrt{133}\times\sqrt{133}$)R4.3° [1]; two rotational domains were observed.

The two Moiré diffraction patterns displayed in figure 3.4 exhibit differently sized overlayer unit cells. The size is determined as the ratio of the overlayer and substrate reciprocal lattice constants, as determined from the LEED images. This procedure is not very precise, due to aberrations in imaging. For the Moiré structures which form at high coverages (figure 3.4 (a)), ratios between 11 and 13 are measured; taking a medium value, the structure is termed "(12×12)-Moiré". For the low coverage Moiré structures (figure 3.4 (b)) on the other hand, ratios between 8 and 10 are found; hence it is termed "(9×9)-Moiré" structure.

The (12×12)-Moiré structure is probably identical with the ($\sqrt{133}\times\sqrt{133}$)R4.3°-Moiré structure reported in [1]; the periodicities match within the experimental error. No rotational domains show up in figure 3.4 (a), but they might just be not resolved. In STM also deviating rotational angles were observed, indicating weak substrate-overlayer interaction; probably slightly different rotational domains are averaged in figure 3.4 (a). The LEED pattern possibly matches the one presented in [1], but the quality of the image given there is to poor to decide that question.

The assignment is corroborated by another consideration. As mentioned above, the ($\sqrt{133}\times\sqrt{133}$)R4.3°-Moiré structure is a VO_2 overlayer, arranged as a hexagonal O-V-O stack [1]. Its vanadium density is the highest of all known monolayer structures, being 0.85 V atoms per Rh (calculated from STM data in [1]). It is the only known monolayer structure capable of taking up the 0.82 MLE vanadium coverage deposited in figure 3.4. The Moiré pattern appears exclusively in the image, which means that 3-dimensional oxide or second layer structures [1, 2] are not simultaneously present. Thus the vanadium in figure 3.4 (a) (0.82 MLE) is, in fact, organized in a single vanadium layer, which strongly suggests the hexagonal O-V-O stack with its high V-capacity as the (12×12)-Moiré structure. If more vanadium than 0.85 MLE is added on top of the Moiré-VO_2 layer, other structures develop, namely a (2×2) second layer or ($\sqrt{3}\times\sqrt{3}$)R30°-V_2O_3 bulk-like crystallites [1]. This will be of interest in later discussion.

The (9×9)-Moiré structure (figure 3.4 (b)) has not been reported in literature up till now. Throughout this work it was regularly observed if low vanadium coverages

(< 0.3 MLE) were exposed to high oxygen pressures ($> 10^{-5}$ mbar) at 500°C. It might be closely related to the (12×12)-Moiré structure, but will be regarded as unknown here. The highly oxidized (9×9)-Moiré structure can be distinguished from the reduced (9×9)-V_2O_3 by LEED: as typical for Moiré patterns, only the satellite beams close to the substrate reflexes are visible, which is different for a regular (9×9) pattern (see figure 3.2).

3.2 Behavior of ultra-thin films exposed to the $H_2 + O_2$ reaction

For typical PEEM reaction experiments the surface was prepared with a sub-monolayer dosage VO_x, as described in section 2.3. Then the oxygen partial pressure $p(O_2)$ and the sample temperature T were adjusted to the desired values, and the sample was moved to the microscope position. Usually $p(H_2)$ was treated as control parameter during an experiment while keeping $p(O_2)$ and T constant. At high temperatures, $p(O_2)$ was almost always kept at a certain minimum value (10^{-7} mbar) to prevent alloying [12], since oxygen acts like an anchor trapping vanadium on the surface as an oxide. Most experiments were conducted at 500°C < T < 600°C; at significantly lower temperatures the mobility of vanadium appears to be too small to observe pattern formation on a limited time scale. Higher temperatures were usually avoided, also to prevent alloying.

After deposition of 0.2 MLE VO_x the oxide is homogeneously distributed on the length scale of PEEM; the distribution on a smaller scale should be similar to the 0.141 MLE image in figure 3.2. This homogeneous state is lifted by pattern formation. The surface can be rehomogenized by annealing the sample at 750°C in $2 \cdot 10^{-7}$ mbar O_2 for 3 min. This procedure was used regularly to get identical starting conditions in different experiments without having to deposit fresh vanadium every time. Figure 3.5 shows how a surface is modified as it is exposed to the $H_2 + O_2$ reaction at 500°C and $p(O_2) = 5 \cdot 10^{-6}$ mbar by slowly increasing the hydrogen partial pressure (H_2 upramping).

Without hydrogen the surface appears dark, indicating a high work function Φ caused by the high oxygen coverage Θ_O; this is the usual observation for surfaces covered by adsorbed atomic oxygen O_{ad} [13]. Upon continuously increasing the hydrogen partial pressure the surface brightens at $p(H_2) = 1.2 \cdot 10^{-6}$ mbar (60 s after

starting the p(H$_2$) ramp) to lower Φ. This can be interpreted straight forward as a decrease of Θ_O due to the onset of hydrogen adsorption and reaction, as it is demonstrated in section 3.3. Spatial inhomogeneities appear 25 s later at p(H$_2$) = 2·10^{-6} mbar; hydrogen is kept constant now. A stripe pattern evolves during the next 20 s. It is shown in section 3.4 that the dark parts of the surface are covered by VO$_x$, while the bright parts are almost bare Rh(111).
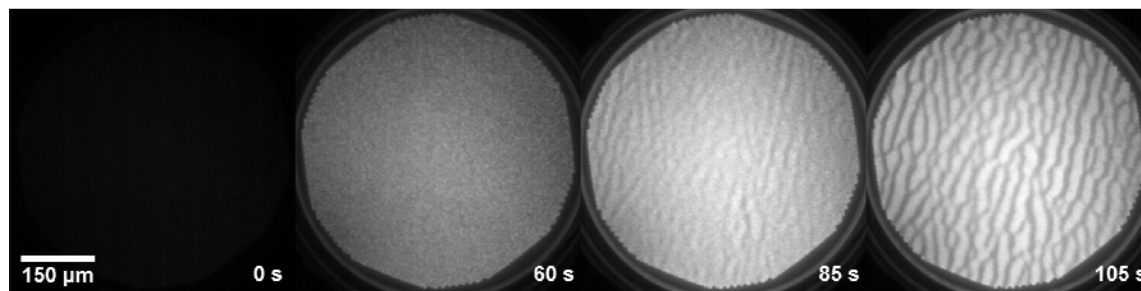

Figure 3.5: Sequence of PEEM images of the Rh(111)/VO$_x$ surface (0.2 MLE) exposed to the H$_2$ + O$_2$ reaction at 500°C and 5·10^{-6} mbar O$_2$. p(H$_2$) is increased continuously from residual pressure (~10^{-8} mbar) via 1.2·10^{-6} mbar (60 s) to 2·10^{-6} mbar (85 and 105 s).

Figure 3.6 focuses on details prior to stripe pattern formation. The PEEM brightness trace of the experiment from figure 3.5 is displayed in (a), while figure 3.6 (b) shows one from a similar experiment conducted at ten times higher pressure. The latter experiment (b) was done without first applying the homogenization treatment described above, so inhomogeneities of a previous experiment are still present (see figure 3.8). At higher pressure the phenomenology is similar, but the transformations of the surface occur, in contrast to figure 3.6 (a), via reaction fronts. Therefore, different states of the system can be distinguished.

Comparing (a) and (b) in figure 3.6, one notices several differences. The steep brightness changes in (b) are associated with the reaction fronts displayed in (c)-(e). They represent transitions between different states of the system, denoted as I, II, III and IV. Trace (a) exhibits a similar structure, with smoother transitions (the brightness minimum at 63 s is not mentioned in figure 3.5). These transitions are shifted to a higher H$_2$:O$_2$ ratio in (b), as compared to (a).

The transition I $\rightarrow$ II is associated with the removal of oxygen from vanadium-free Rh(111) area at the onset of the H$_2$ + O$_2$ reaction, as demonstrated in section 3.3. The state transition proceeds via a reaction front due to the site-blocking effect O$_{ad}$ exerts on H$_2$ adsorption (see section 1.2).
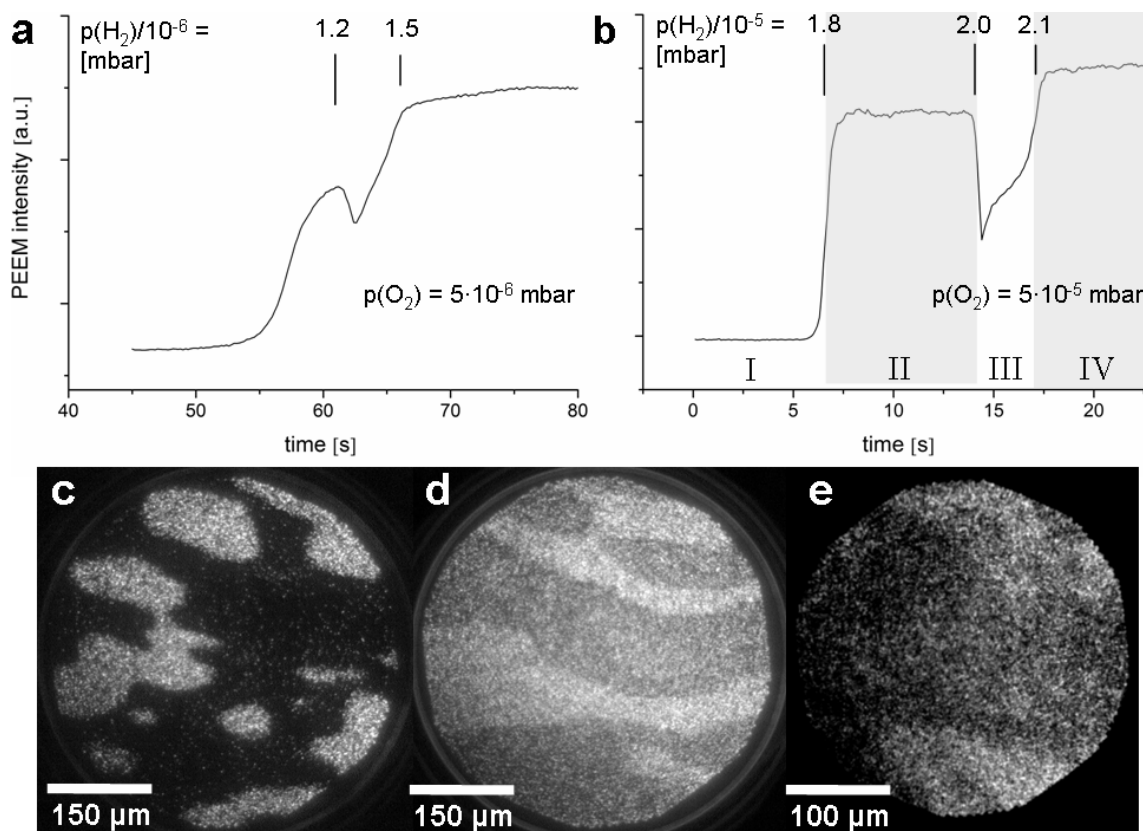
Figure 3.6: (a) PEEM brightness trace from the experiment in figure 3.5 (T = 500°C, p(O$_2$) = 5·10^{-6} mbar, Θ_V = 0.2 MLE); the time scale refers to the start of the H$_2$ ramp, as in figure 3.5. (b) Similar experiment at 500°C, p(O$_2$) = 5·10^{-5} mbar, Θ_V = 0.2 MLE; the steep brightness changes correspond to reaction fronts which allow to distinguish the system states I, II, III and IV. The zero of the time scale here is arbitrary, the H$_2$ ramp starts before 0 s. (c-e) PEEM images showing the three front-induced surface transitions in order of appearance; (c) and (d) originate from another experiment at slightly higher pressure (p(O$_2$) = 8·10^{-5} mbar) showing the fronts more clearly; (e) is taken from experiment (b), with strongly enhanced contrast to visualize the spatial inhomogeneity.

Transition II → III, leading to an intermediate grey level, is interpreted as reduction of the VO$_x$ overlayer. Since the experiments are started in oxygen, a highly oxidized ($\sqrt{7}$, $\sqrt{13}$ or (9×9)-Moiré) structure is initially present, which gets reduced under reaction conditions. This is shown in the sections 3.4 and 3.5.

Patterns evolve either from state III or IV. Usually p(H$_2$) was raised until reaching state IV. A pattern then develops within a few minutes or seconds, depending on the pressure (see figure 3.5). Experiments at ~10^{-4} mbar O$_2$ showed that at such high pressures, favoring fast dynamics, patterns can also develop if the H$_2$ ramp is stopped in state III. However, the dynamics are quite slow in this case, compared to state IV; this is addressed in section 3.6. The main difference between the system states III and IV is the

microstructure of the oxide, as demonstrated by LEED and LEEM measurements in section 3.5.

The actual pattern formation process is discussed in subsequent sections; all the patterns presented there were formed from state IV, unless stated otherwise. It has to be noted that the partial pressure ratios $O_2:H_2$ inducing the state transitions appear to depend not only on p and T, but also on the history of the sample. The additional influence supposedly results from differences in the initial vanadium distribution.

If $p(H_2)$ is reduced after a pattern has evolved from state IV, one could expect a reversed behavior to that in figure 3.6, but this is only partially true. Even at high pressures no reaction fronts are observed upon H_2 reduction in PEEM, with one exception: the VO_x oxidation step III $\rightarrow$ II can proceed via front propagation, provided that $p(H_2)$ is decreased extremely slow. The PEEM images in figure 3.7 illustrate the transition III $\rightarrow$ II at $4.5 \cdot 10^{-5}$ mbar O_2, 500°C and a VO_x coverage of 0.3 MLE. The two rows correspond to subsequent experiments, with the only difference that the hydrogen pressure is decreased slightly faster in the bottom row. Apparently this faster variation causes the pattern to vanish more quickly, and without a macroscopic reaction front.
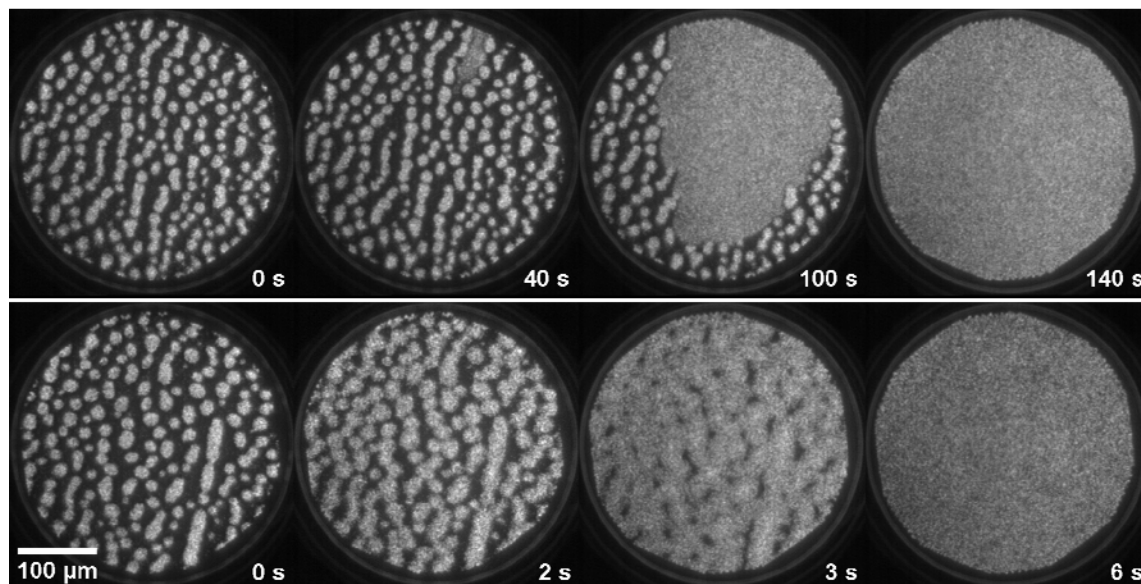
Figure 3.7: top row: sequence of PEEM images displaying the transition III $\rightarrow$ II at 500°C, $4.5 \cdot 10^{-5}$ mbar O_2 and $\Theta_V = 0.3$ MLE, induced by an extremely slow $p(H_2)$ decrease; the VO_x is oxidized and the pattern vanishes. Bottom row: similar experiment, with slightly faster $p(H_2)$ decrease.

Besides oxidation of the VO_x overlayer something else happens in figure 3.7: the pattern unravels and is not longer visible in state II. In principle this can be caused by

either a homogenization of the vanadium distribution, or a too low work function contrast between V-covered and V-free areas in state II. It turns out that the latter explanation is correct.
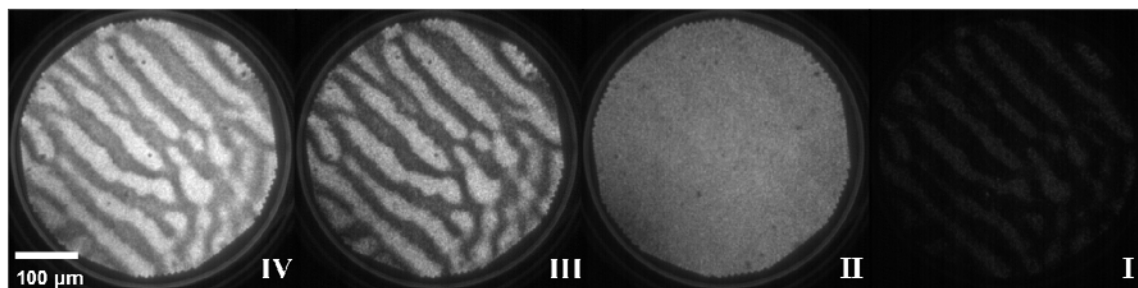

Figure 3.8: PEEM image sequence from an H_2 downramping experiment at 545°C and $2.5 \cdot 10^{-6}$ mbar O_2 and $\Theta_V = 0.2$ MLE, displaying the four states upon reducing hydrogen. In state I the pattern is still present (though barely visible), while in state II the work function contrast is not sufficient to distinguish the pattern. The system states IV and III differ just slightly in brightness and contrast.

Figure 3.8 displays the four system states upon decreasing the hydrogen pressure. The states IV and III just differ in brightness/contrast. In state II the pattern is not visible, as in figure 3.7, but it reappears in I. Usually in the oxygen covered state the PEEM image is homogeneously dark, but the conditions (high T, low $p(O_2)$) were chosen to produce a low oxygen coverage intermediately. Therefore, the oxygen covered Rh(111)-O surface appears not completely dark at first, and some contrast to the VO_x-covered area is given. This demonstrates that the pattern, while not being visible in state II, still exists. In state I the pattern is in principle unstable, but the surface needs several hours to homogenize even at temperatures around 500°C. This is due to the low mobility of the highly oxidized VO_x overlayers on Rh(111)-O.

The transition II → I corresponds to the inhibition of the reaction by formation of an oxygen adlayer on Rh(111) which blocks H_2 adsorption (see section 1.2). But figure 3.8 shows that changes also occur on the VO_x-covered area, since its brightness changes as well. LEEM measurements reveal that the oxygen coverage on the Rh(111) surface also affects the adjacent VO_x film: upon decreasing $p(H_2)$ the closed oxide layer breaks apart into nanoscale islands which can drift onto the Rh(111)-O surface. This is demonstrated in section 3.5.

3.3 Catalytic activity

The activity of Rh(111) is modified by addition of a partial monolayer of vanadium oxide. In order to obtain information on that, measurements with differentially pumped quadrupole mass spectrometers (QMS) were performed; the setup is described in figure 2.1 (b). In addition to a QMS mounted in the regular fashion behind a cone pointing towards the sample, a second one was mounted within the pump line of the differentially pumped PEEM. The purpose was to analyze the gas flow directly from the surface, as imaged by the microscope. In this way, effects from the backside of the specimen should be discriminated. That did not work perfectly due to the big distance between sample and microscope, but nevertheless one successful experiment was conducted, which is shown in figure 3.10. Thus it can be recommended to adopt the idea to modern PEEM or LEEM instruments working at a smaller distance.

Thin vanadium oxide films on Rh(111) easily change between the V oxidation states upon low-pressure treatment with oxygen or hydrogen at elevated temperatures (see section 3.1 and [3, 6, 14]). Thus they fulfill the most fundamental requirement for catalytic activity. For bulk V_2O_5 it has been demonstrated that the $H_2 + O_2$ reaction is facilitated under continuous flow conditions at atmospheric pressure [15]. In principle this also holds at low pressures, as shown by a rather exotic experiment with VO_x films on Pd(111) [16]: films of varying thickness (up to several monolayers) were exposed to the reactants at 430°C yielding water, but H_2 was supplied via permeation through the sample, not from the gas phase. A more conventional approach was followed here to measure the reactivity of VO_x/Rh(111). The sample was completely covered with vanadium oxide and heated in an oxygen atmosphere, and an excess of hydrogen was added then.

The experiment at $1 \cdot 10^{-4}$ mbar O_2 and 500°C on a ~3 MLE film is displayed in figure 3.9; for comparison the activity of bare Rh(111) is given as well. Varying the conditions to 600°C or ten times lower pressures yields similar results. The plot shows directly that VO_x is much less active than Rh(111). The raw data of the water production rate gives a ratio Rh(111):VO_x of roughly 15:1. This has to be corrected for the water produced by the ion source of the QMS itself (determined by blank measurement), yielding 80:1.

In figure 3.9 (b) the oxygen consumption traces of the experiment are displayed. Under stationary conditions the water production rate is reflected in the O_2 consumption as a consequence of mass balance of the reaction. Therefore, the water production ratio of Rh(111):VO_x (80:1, see above) should be reflected in (b); one reads, however, 6:1. The reason for this deviation is the activity of the back side of the rhodium sample. If the reaction takes place on the back side, water molecules have to interact several times with the chamber walls in order to reach the detector. H_2O molecules exhibit high sticking probabilities (close to 1), so almost every molecule sticks before being detected ("wall pumping"). Due to a lower sticking probability, O_2 is much less affected by wall pumping. Therefore, water production on the back side is detected far less efficient than consumption of oxygen, which explains the detected deviations of water production and oxygen consumption. Evidently, the backside produces high amounts of water. Probably there is even a back side contribution to the water trace in 3.9 (a) (VO_x), since the activity of the probed oxide-covered front side of the specimen is extremely small. The value of 80:1 for the VO_x activity compared to Rh(111) is hence considered to be an upper limit.
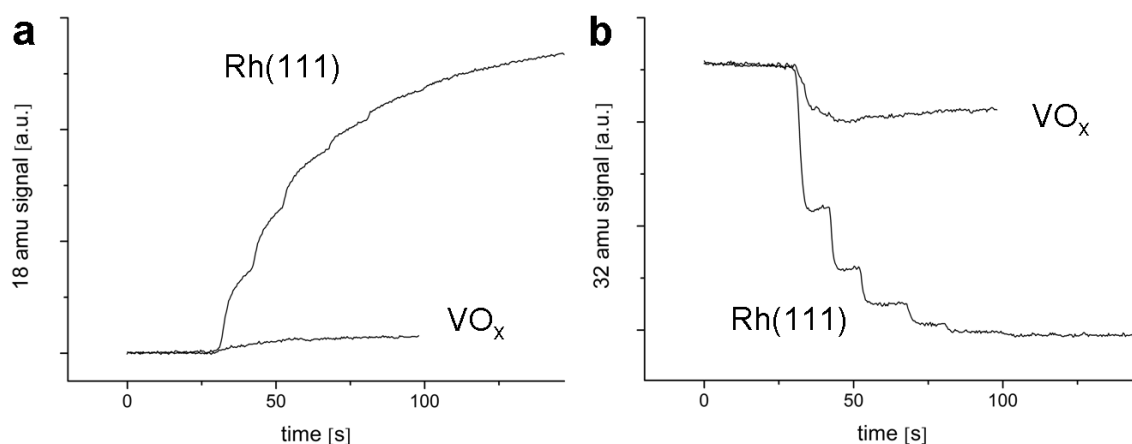
Figure 3.9: (a) QMS experiment to compare the catalytic activity of a dense VO_x film (~3 MLE) with bare Rh(111). At 500°C and $1 \cdot 10^{-4}$ mbar O_2 an excess of hydrogen was added (at 30 s), stepwise in case of Rh(111), and in one step in case of VO_x. The H_2O traces (mass 18) are displayed. (b) O_2 traces (mass 32) of the same experiment; offsets had to be added.

This result is surprising, as significant activity has been demonstrated in the literature (see above), but those experiments are quite different. V_2O_5 powder has been exposed to the reactants at 450°C and atmospheric pressure [15], while here a thin film is treated with a seven orders of magnitude lower pressure. Prior to the experiment in figure 3.9, LEED indicated the presence of a variety of structures, mainly V_2O_3 bulk-like

crystallites and the "wagon wheel"-VO monolayer structure (see section 3.1). No V^{5+} appears to be present and is also not likely to form during reaction: within the first monolayer the V^{5+} structures, $\sqrt{7}$ and $\sqrt{13}$, are strongly disfavored at high coverages due to their high demand for space (only 0.43 and 0.46 V/Rh, respectively, see figure 3.1). The literature suggests that also the crystallites cannot be oxidized to V_2O_5, as it was stated in a recent review that bulk V_2O_5 films are apparently not stable in UHV (referring to pressures $< 10^{-3}$ Torr) [17]. Although this statement was recently proven to be wrong [18], it still holds that such films seemingly do not *form* at low pressures. If V^{5+} is an essential component of the main catalytic mechanism, high activity is not to be expected at low pressures.

An experiment with a Pd(111) surface covered completely with V_2O_3 crystallites demonstrated $H_2 + O_2$ activity already at 430°C and 10^{-6} mbar O_2 [16], although no V^{5+} should have been present as well. The fundamental difference to the experiment presented here is that hydrogen was not dosed directly from the gas phase, but enters via the backside of the sample, which is used as a permeation source. H atoms hence reach the probed surface via diffusion, which eliminates the steps of H_2 adsorption and dissociation from the catalytic cycle. This might be the reason why the reaction works in spite of missing V^{5+}.

In section 3.2 several states of the catalytic system are described which can be observed upon exposing a partially VO_x-covered surface (0.2 MLE) to different O_2:H_2 ratios at 500°C. In order to understand how those system states are related to the activity of the catalyst, rate measurements have been performed under these conditions.

Figure 3.10 presents the results from H_2 upramping experiments at 500°C and $1 \cdot 10^{-4}$ mbar O_2. The experiment displayed in (a) and (b) was performed with the rate measurement setup shown in figure 2.1 (b), with one "line of sight"-QMS analyzing the gas flow directly from the sample. In addition, a second QMS behind the PEEM was used to monitor the "external" partial pressures in the main chamber, which allows distinguishing between real effects from the probed surface, and others. Most features in the mass traces of the "line of sight"-QMS also appear much *weaker* in the "PEEM"-QMS data, but, in contrast to that, artifacts from manual leak valve operation or contributions from the back side of the sample are detected *stronger* in the "PEEM"-QMS and can thus be identified. This is applied in figure 3.10 (a): the real effects between 280 and 350 s do almost not appear in the grey line ("PEEM"-QMS).

Contrary to that, a small "dent" in the grey line at 400 s is reflected much weaker in the black mass 2 trace ("line of sight"-QMS) and is thus identified as a backside effect, together with the associated decrease of O_2 (Mass 32).
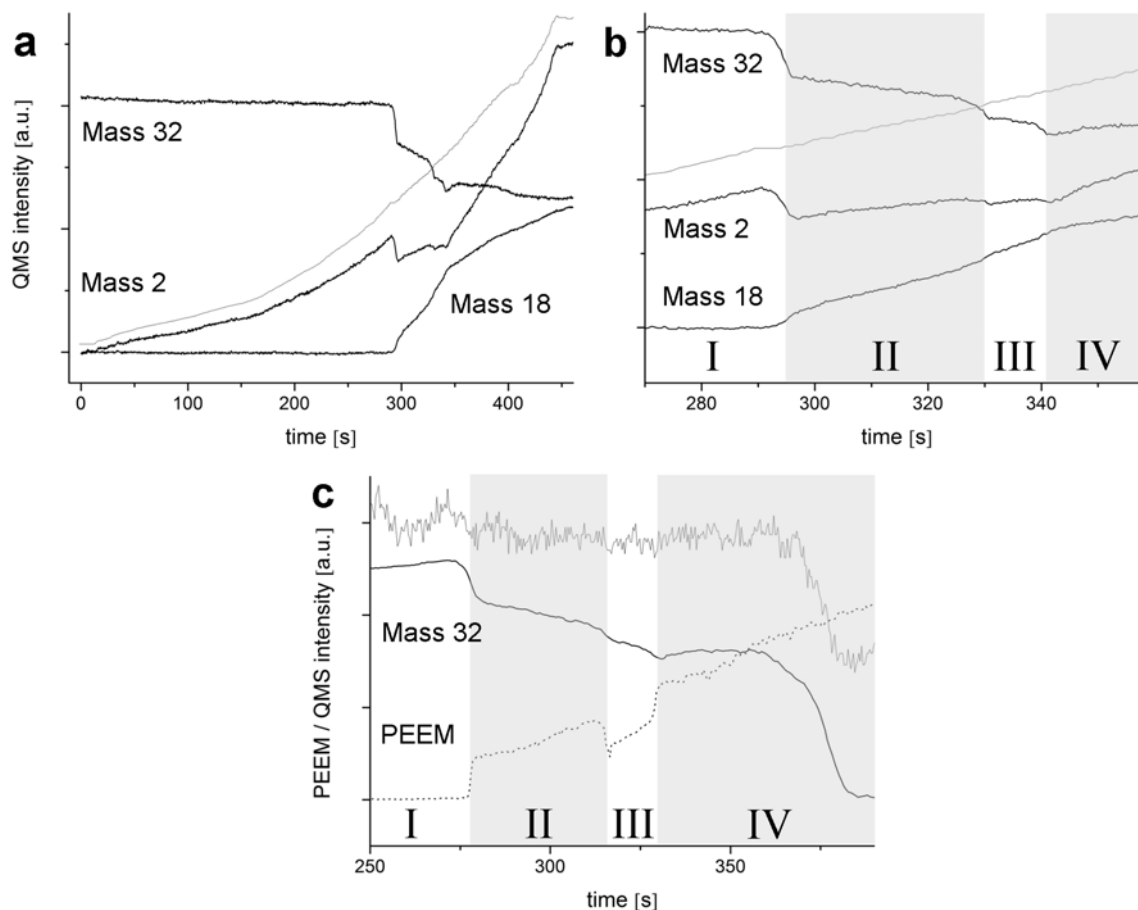

Figure 3.10: H_2 upramping experiment followed by two differentially pumped QMS. In (a) the "line of sight"-QMS traces for hydrogen (mass 2), oxygen (mass 32) and water (mass 18) are displayed as black lines. An additional trace representing the "external" hydrogen partial pressure in the main chamber is also shown (gray line); it was recorded by a second QMS behind the PEEM (see figure 2.1 (b)) and was scaled roughly to the other H_2 trace, with an offset. The conditions are $T = 500°C$, $\Theta_V = 0.2$ MLE, $p(O_2) = 1 \cdot 10^{-4}$ mbar, $p(H_2)$ is varied up to $\sim 6 \cdot 10^{-5}$ mbar. (b) Detail on (a), focusing on the system state transitions; the states are denoted in analogy to figure 3.6. (c) Analogous experiment conducted in front of the PEEM, with the two QMS used vice versa. Only the oxygen trace exhibits significant features resembling the one in (b), except for the huge pressure drop after 350 s which is a backside effect, and a small increase at $t < 250$ s, which is an artifact. The gray line represents the "external" O_2 pressure, the dashed line the integrated PEEM intensity.

Upon raising the hydrogen pressure continuously, no water is produced until $t = 295$ s (see figure 3.10 (a)). The onset of H_2O production is connected with a reaction front transforming the surface from state I $\rightarrow$ II; figure 3.10 (b) displays in detail how

the rate changes are related to the system state transitions. The water signal begins to increase at 295 s, while the reactant traces exhibit a steplike drop. The increasing reaction rate can actually be followed best in the O_2 trace, since oxygen is supplied constantly and the signal reacts instantly to changes, unlike the H_2O signal where variations are obscured due to the strong wall interaction of water.

In section 3.2 it is stated that the system state transition II → III corresponds to reduction of VO_x. In figure 3.10 (b) a steplike decrease of O_2 (330 s) indicates that state III is more active than state II. At first sight this seems to be in conflict with the hypothesis that the $H_2 + O_2$ reaction proceeds essentially on the bare Rh(111) surface. In that case a change of the oxide structure should not significantly influence the activity. However, a closer look at the structures (see section 3.1) explains the observation. The initial VO_3 overlayers, $\sqrt{7}$ and $\sqrt{13}$, have low V-densities (only 0.43 and 0.46 V/Rh, respectively, see figure 3.1) and thus cover a relatively large fraction of the substrate surface. Upon reduction the space requirement of the oxide might change, and hence more bare Rh(111) might be available after. This is actually the case, as demonstrated by LEEM in section 3.5.

During the system state transition III → IV, the O_2 trace in figure 3.10 (a) and (b) exhibits not a steplike drop, but rather a notch, with oxygen almost returning to its prior value. The feature is also present in the H_2 trace. It is concluded that the activity of the states III and IV is equal and that O_2 and H_2 are consumed during the transition. Considering that the transition represents a change in the VO_x microstructure (see section 3.5), one would expect a reduction step upon raising H_2, but reduction should not consume oxygen. However, the notch turns out to be reproducible (see figure 3.10 (c)). Two possible explanations can be offered: either the structural change is a swift two-step reaction consisting of VO_x reduction and reoxidation of an unstable intermediate, or there is some kind of phase boundary effect, allowing oxygen uptake at the edges of oxide islands. The experimental results do not allow an answer. Perhaps an STM study on the VO_x structures of state III and IV (both unknown) can achieve that in the future.

The tentative assignment of the system states I, II, III and IV to figure 3.10 (b) can be verified by an additional experiment shown in (c). It is basically the same as the experiment displayed in (a) and (b), but the sample is in PEEM position and the two mass spectrometers are used vice versa: the "PEEM"-QMS now analyzes the gas flow from the front side of the sample, and the other QMS controls the "external" O_2 pressure in the main chamber (grey line). A PEEM movie is recorded synchronously. The PEEM

brightness trace is displayed as a dashed line; between 250 and 350 s it exhibits the same three steep changes associated with reaction fronts which are originally used to define the system states in figure 3.6. The oxygen trace, represented as a solid black line, closely resembles the one in figure 3.10 (b); the three features between 250 and 350 s coincide with the reaction fronts in the PEEM trace. Therefore, the system states assigned to figure 3.10 (c) and (b) are the same as in figure 3.6 (b).

Figure 3.10 (c) also demonstrates the benefit of having a QMS mounted behind a differentially pumped electron microscope. As already mentioned above, the setup does not work too well due to the big PEEM-to-sample distance, so after 360 s the O_2 trace is dominated by a huge backside effect (same effect as in (a) at 400 s). But the detection of the state transitions shows that the front side signal is preferentially measured anyway.

3.4 Surface characterization *in situ*

In section 3.2 pattern formation during the $H_2 + O_2$ reaction is reported (see figures 2.9, 3.5, 3.7 and 3.8). From PEEM alone it is already possible to assign the dark stripes as V-enriched, compared to the brighter area in between: if vanadium is deposited only on a part of the surface, PEEM shows under reaction conditions that the uncovered part appears just like the VO_x-covered region, but without the dark structures. More detailed surface characterization under reaction conditions was accomplished with the LEEM instruments in Clausthal and Trieste.

Combining LEEM with LEED and XPS, as done in figure 3.11, allows a closer look at the stripe pattern. The energy for the LEEM image in (a) is chosen to give a contrast similar to PEEM, imaging the V-enriched part of the surface as dark area. Both regions are characterized with μ-LEED and μ-XPS. The bright and dark areas exhibit a (1×1) and a (2×2) diffraction pattern, respectively. Figure 3.11 (b) adds the chemical information. The (1×1) region is almost bare Rh surface, only small amounts of V and O are detected. The oxygen signal originates from O_{ad} and OH_{ad} (present due to the ongoing $H_2 + O_2$ reaction), and supposedly also an additional oxygen species is bound to the residual vanadium with its high oxygen affinity. Small planar hexagonal clusters of V_6O_{12} were reported to travel on a Rh(111) surface at elevated temperatures; they were also reported to condense into islands in presence of O_2 or H_2 at 250°C [2, 4, 6, 7], but in

presence of both gases at 500°C they might be stable nevertheless. The small $V2p_{3/2}$ signal exhibits a binding energy of ~515 eV (see lower spectrum, figure 3.11 (c)) and hence does not represent alloyed vanadium; a binding energy close to metallic V (512.4 eV, [19]) is to be expected in that case.

While outside the stripe in the (1×1)-region little vanadium is found, the major fraction is condensed in the (2×2)-region as an oxide. Thus the phenomenon of stripe pattern formation under reaction conditions is regarded as an almost complete phase separation. The nature of the (2×2)-VO_x phase is not completely clear, since it was not observed before in the system Rh(111)/VO_x.
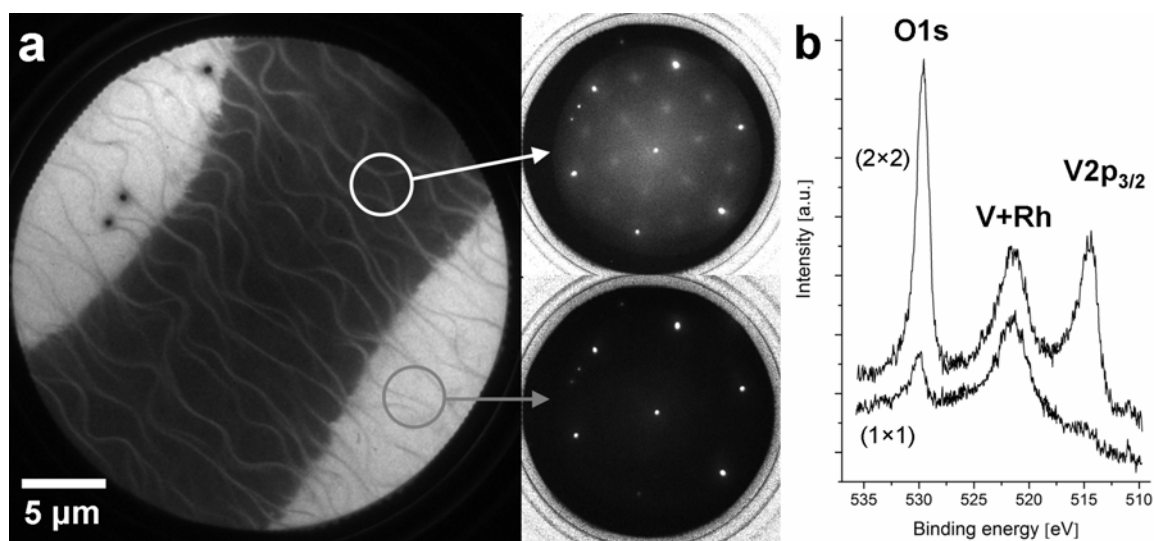
Figure 3.11: (a) Bright-field LEEM image (5 eV) of a VO_x stripe in system state IV (480°C, $p(O_2) = 5.7 \cdot 10^{-7}$ mbar, $p(H_2) = 6.6 \cdot 10^{-7}$ mbar, $\Theta_V = 0.2$ MLE) and μ-LEED patterns of the dark (2×2)- and bright (1×1)-region at 40 eV. The tree black spots (white spots in LEED) are due to detector damage, the wavy lines represent step bunches. (b) μ-XPS of the (2×2)- (upper spectrum) and (1×1)- (lower spectrum) regions at $h\nu = 655$ eV. Three single dispersive plane spectra were combined in each case; the energy scale was calibrated to the $Rh2p_{3/2}$ peak (not shown, measured separately to be at 496.3 eV, referenced to the Fermi level), which does not shift since it originates essentially from the bulk. The peaks represent (from left to right): O1s, $V2p_{1/2}$ + $Rh3p_{1/2}$ and $V2p_{3/2}$.

Figure 3.12 gives more detail on the (2×2)-region. In (a) dark-field LEEM data is presented; the indicated half-order spots selected for imaging lead to high intensity in the area where the corresponding overlayer is located. A bright-field image is shown for comparison (top right). The two dark-field images look essentially the same, indicating that probably a true (2×2)-structure is present, in contrast to the three domains of a (2×1)-structure which also give rise to a (2×2) diffraction pattern [9]. The spots selected in figure 3.12 (a) actually *would* belong to two different rotational domains of a

(2×1)-structure, so the fact that they yield the same image indicates that either the domains are to small to be spatially resolved, or that there are no domains and thus no (2×1)-structure. The first case can not be excluded, but the experiment speaks in favor of a true (2×2)-structure.
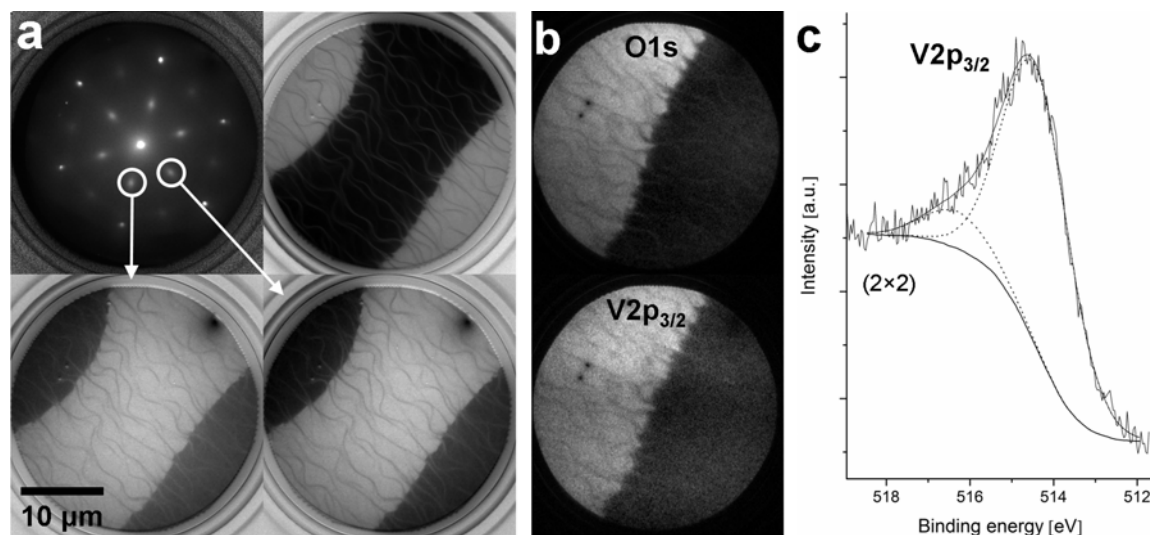

Figure 3.12: (a) Dark-field analysis of the (2×2)-structure; the top row shows the integral LEED image (52 eV) and the corresponding bright-field image (5 eV), the bottom row shows dark-field images from the indicated beams (15 eV). The images were normalized. (b) XPEEM images on the indicated photoemission lines, recorded at $hv = 655$ eV; background images were subtracted. (c) V2p$_{3/2}$ detail of the μ-XP spectrum on the (2×2)-region; the data was fitted with equal widths for both peaks (FWHM = 1.85 eV). The binding energies are 514.4 and 516.3 eV; the intensity ration is 8:1.

The origin of the unexpected (2×2) diffraction pattern is still to be discussed. In principle, the phase might be something new, but some (2×2)-structures are known from the literature which are possibly related to this one. It is well-known is that O$_{ad}$ alone can form (2×2)-O and (1×2)-O structures on Rh(111) [9]. Clearly oxygen is condensed together with vanadium in the (2×2) region. This fact is already known from figure 3.11, but it can also be demonstrated directly with XPEEM. In figure 3.12 (b) the phase boundary is imaged using O1s and V2p$_{3/2}$ photoelectrons, respectively, resulting in very similar representations; apparently oxygen and vanadium are well-mixed within the resolution limits (~50 nm). One could argue that smaller V-free regions might exist where a Rh(111)-O overlayer gives rise to the observed (2×2) diffraction pattern. However, μ-LEED of the mesoscopic V-depleted region demonstrates that Rh(111) exhibits a (1×1) pattern under the applied conditions (see figure 3.11), so this hypothesis can safely be rejected.

A V-Rh(111) surface alloy with a (2×2)-structure was reported in [20]. If this alloy would accommodate an oxygen adlayer on top, it could also be a possible candidate. This is, however, excluded by XPS, as shown in figure 3.12 (c). A V2$p_{3/2}$ detail spectrum reveals two components at binding energies of 514.4 and 516.3 eV obtained from peak fitting. Both values are too high to represent alloyed vanadium, as mentioned above. They correspond to oxidic V, and indeed a (2×2)-VO$_x$ structure on Rh(111) is known: as mentioned in section 3.1, a V-oxide layer with a (2×2) periodicity can grow on top of a (12×12)-Moiré layer. This (2×2)-layer is supposed to be the same honeycomb-lattice V$_2$O$_3$ structure observed on Pd(111) and Rh(15 15 13) (see section 3.1 and [1, 8, 11, 21]). The bilayer of (2×2)-V$_2$O$_3$ on Moiré-VO$_2$ (actually an O-V-O-V$_2$O$_3$ stack, V$_6$O$_{11}$) is an appealing model for the (2×2) region at the first glance, because it directly explains the two V components of the XP spectrum as V^{3+} and V^{4+}. The binding energies of even these structures on Pd(111) were measured to be 514.2 eV ((2×2)-V$_2$O$_3$) and 516.3 eV (VO$_2$-hex, analogous to (12×12)-Moiré) [21], which might be considered to match, regarding the different substrates and the experimental error. But a closer look at the binding energies reveals that the model is to be rejected. The value of ~514 eV for V^{3+} is only valid if the vanadium is coordinated to a metallic substrate, but if this is not the case, as in O-V-O-V$_2$O$_3$, binding energies around 516 eV are to be expected [1, 19]). Therefore, the main component in figure 3.12 (c) is not explained by the V$_2$O$_3$-on-Moiré bilayer model.

The XP spectrum in figure 3.12 (c) suggests a surface-V$_2$O$_3$ structure, with V coordinated to Rh, as main component of the (2×2)-phase. Surface-V$_2$O$_3$ usually exhibits a (9×9)-periodicity on Rh(111) (see figure 3.2), but on similar substrates, Pd(111) and Rh(15 15 13), a (2×2)-V$_2$O$_3$ overlayer was observed [6, 8]. The close structural relationship between the (2×2)- and (9×9)-structure is shown in figure 3.2. There was some discussion in the literature about why a (9×9)-overlayer forms on Rh(111) instead of (2×2) [6, 8]; the selection was attributed to interfacial strain between Rh(111) and the (2×2)-V$_2$O$_3$ structure. The (9×9)-overlayer represents a strain-less structural variation matching the Rh(111) lattice constant which is about 2 % smaller compared to Pd(111). In fact, both overlayers can be observed on Rh(15 15 13) [8]: the (2×2)-oxide is present on narrow terraces (< 3 nm) where the big (9×9) unit cell does not fit. This selection by the terrace size cannot be responsible for the observation of (2×2)-V$_2$O$_3$ here, since the surface orientation is nominally (111), with typical terrace widths of about 100 nm.

One can only speculate for now why the (2×2)-overlayer is observed under reaction conditions instead of (9×9)-V$_2$O$_3$. The energy difference between the two structures appears to be quite small, since otherwise the (2×2)-overlayer would not form on narrow Rh(111) terraces. The (9×9)-oxide is usually favored, but the presence of the reactant gases at ≥ 500°C might increase the concentration of vacancies. Those might provide some strain relieve and hence stabilize the (2×2)-structure.

The second component of the XP spectrum in figure 3.12 (c) at 516.3 eV is of unknown origin, the binding energy suggests a high V oxidation state of +4 or +5. A phase boundary effect can be excluded, since there are no phase boundaries in the probed area. However, V^{+3} is clearly present in excess. This information alone is sufficient to rule out the possibility of a mixed-valent oxide overlayer with a (2×2)-periodicity: at least one highly oxidized V atom would have to be present in the elementary cell, and, based on the XP spectrum, many more V^{3+} atoms, plus the associated O atoms. But a (2×2) unit cell is already crowded with 2 V and 3 O atoms (see model in figure 3.2), which is the reason why surface-V$_2$O$_3$ usually relaxes into the (9×9)-structure. Mixed-valent monolayer structures with one oxidation state in excess require larger unit cells, as in the case of the (5×5)- and ($5 \times 3\sqrt{3}$)-rect structures [3].

It is concluded that the highly oxidized vanadium species detected in XPS is not part of the (2×2)-structure. A likely explanation could be VO$_x$ accumulation at the step bunches, since step edges, as well as V atoms, have a high affinity towards oxygen [22]. Thus population of step bunches with highly oxidized V should be favorable. To sum this up, the stripes probably consist of honeycomb-lattice (2×2)-V$_2$O$_3$ stabilized by vacancies, along with higher oxidized vanadium at step bunches.

From the μ-XP spectrum in figure 3.11 (b) the relative coverages of oxygen and vanadium can be obtained by evaluation of the relative intensities. Integration of the O1s and V2p$_{3/2}$ peaks after subtracting Shirley backgrounds (see section 2.6) yields a raw intensity ratio O1s:V2p$_{3/2}$ of 1.7:1. Correction of this value with the transmission of the analyzer (~10 % despite the small energy difference) and subsequent addition of 50 % for the V2p$_{1/2}$ level (degeneracy = (2j+1)) gives a ratio O1s:V2p of 1:1. In order to obtain the actual ratio of emitters, which equals the relative O and V coverages, the photoionization cross sections χ of the core levels have to be taken into account. Those can be calculated according to [23]:

$$\chi = \frac{\sigma}{4\pi} \cdot \left(1 + \frac{\beta}{2}\left(3\cos^2\delta - 1\right)\right); \;\; \delta = 16°$$

$$\sigma_{O1s} = 0.33, \;\; \beta_{O1s} = 2.00 \Rightarrow \chi_{O1s} = 0.073 \tag{3-1}$$

$$\sigma_{V2p} = 1.14, \;\; \beta_{V2p} = 1.24 \Rightarrow \chi_{V2p} = 0.190$$

σ is the angle independent contribution to the photoionization cross section, β the so-called asymmetry parameter (both taken from [23]), and δ the angle enclosed by the emission direction (surface normal) and the photon polarization vector.

Consideration of the photoionization cross sections from equation (3-1) yields relative coverages O:V of 2.6:1. This value is not in sufficient agreement with the picture of the (2×2)-phase presented above: for a V_2O_3 overlayer one would expect 1.5:1. However, the V2p$_{3/2}$ binding energy of the main component (314.4 eV) excludes a highly oxidized VO_x layer. The excess of surface oxygen has to be explained differently. On the one hand, there is the second, higher oxidized vanadium species probably located at the step bunches, which binds some extra oxygen. On the other hand, it is mentioned above that the (2×2)-V_2O_3 is probably stabilized by vacancies; those are probably missing vanadium atoms. In addition, extra oxygen atoms could be bound to the rhodium substrate inside of the vacancies, increasing the oxygen content of the overlayer while not influencing the vanadium oxidation state.

3.5 The system states in LEEM and LEED

Figure 3.13 illustrates a hydrogen downramping experiment conducted in LEEM, providing additional information on the different states of the system observed with PEEM (see figure 3.6). The system states in figure 3.13 are assigned in analogy to the PEEM and QMS experiments presented in the figures 3.6, 3.8 and 3.10. The states III and II are not stationary here, as indicated by the continuously changing LEEM brightness in the VO_x trace in figure 3.13 (d). This should be due to slow dynamics at relatively low temperature and pressure here; even though p(H$_2$) is varied quite slowly (see figure 3.13 (d)), the system is continuously adopting to the conditions. Therefore, the state limits indicated in (d) are set to thresholds where the LEEM image starts to change qualitatively to a new appearance. The reaction front at the transition III → II is marked separately by an arrow.
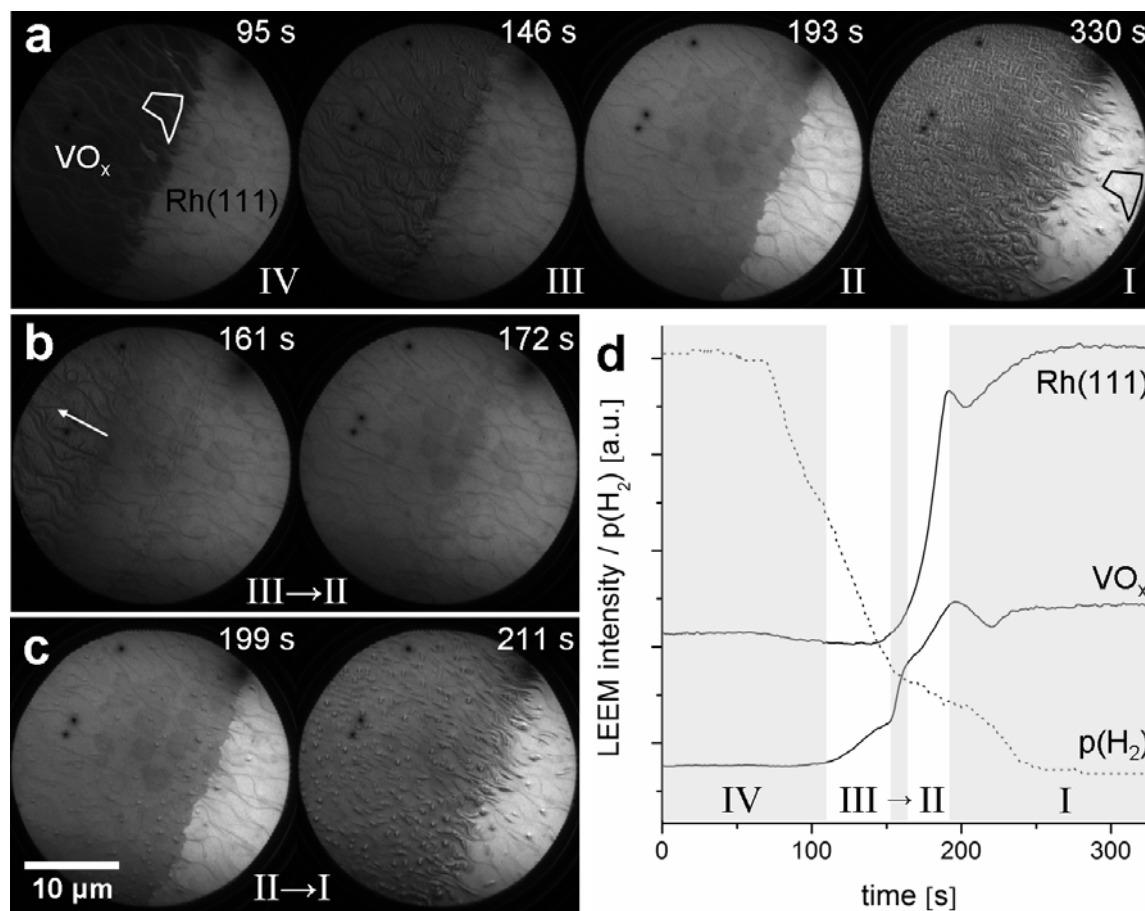
Figure 3.13: (a) Series of LEEM images (5 eV) representing the four system states during an H_2 downramping experiment at 480°C, $p(O_2) = 5 \cdot 10^{-7}$ mbar, $\Theta_V = 0.2$ MLE; $p(H_2)$ is reduced from $6 \cdot 10^{-7}$ mbar to zero. The images are not drifted, but display essentially the same region of the surface. (b) Detail images on the state transition III → II; the propagation direction is indicated by an arrow. (c) Detail images on the transition II → I. (d) LEEM brightness traces of the V-covered and uncovered phases; the scanned regions are indicated in (a). In addition the trace of the H_2 ramp (dotted) is given. The system states are indicated as defined in figure 3.6; the reaction front leading from III → II is separately marked by an arrow.

The experiment starts under reaction conditions in state IV, featuring the (2×2)-oxide which appears dark. Upon lowering $p(H_2)$ the VO_x phase changes continuously to a brighter appearance with a strange topological contrast, which is assigned to state III. Further decrease of the hydrogen partial pressure initiates a reaction front on the oxide, retreating from the phase boundary (see figure 3.13 (b) and compare figure 3.7, bottom row). The remaining VO_x phase is hard to distinguish from the substrate at first (172 s); the latter then turns brighter while the VO_x expands a bit to give the state denoted as II in (a). Furthermore, the initially smooth VO_x film substantially roughens (see (c)), yielding the final state I.

One important detail of the experiment is the expansion of the VO_x phase between 170 and 190 s, which reflects a decrease of the vanadium density. At the end of the experiment the $\sqrt{7}$-structure with 0.43 V/Rh is observed (see figure 3.16), and thus the V-density in the states III and IV is definitely higher than that. This result is in conflict with the coverages originally assigned to PEEM images on the basis of the AES calibration presented in section 2.3. The AES calibration is hence concluded to be wrong. However, the higher vanadium density is in agreement with the proposed model for the (2×2)-oxide being honeycomb-lattice V_2O_3 with 0.5 V/Rh (neglecting the postulated vacancies, see section 3.4). Based on this model the coverages for the PEEM images of state III or IV can now be estimated from the oxide-covered fraction of the surface, because the (1×1)-region contains almost no vanadium (see figure 3.11). If, for example, 40 % of the surface is covered by the (2×2)-phase in a PEEM image, the total coverage is $\Theta_V = 0.2$ MLE, since the (2×2)-oxide contains 0.5 V/Rh. At high coverages, where no clear phase separation is observed, Θ_V can be extrapolated from the vanadium dosage, using this calibration.

The expansion of the oxide phase represents an oxidation step: starting with a dense V_2O_3 phase and ending up with a less dense VO_3 phase requires oxygen uptake associated with an expansion, as observed here. A detailed XPS analysis of the process was not possible, because the vanadium oxides suffer heavily from beam damage. While the (2×2)-structure was found to be stable exposed to the synchrotron beam, the $\sqrt{7}$- and $\sqrt{13}$-structure decomposed instantly. Despite the beam damage problem, synchrotron XPS data exist in the literature for the $\sqrt{7}$-structure [1, 3]; supposedly a less focused, and hence less intense beam was used in those studies.

The LEEM brightness trace of the Rh(111) area in figure 3.13 (d) exhibits an intensity increase starting at about 150 s. It can safely be assigned to the formation of an oxygen adlayer, since it is known that the system Rh(111)/$H_2 + O_2$ is bistable (see section 1.2). A decrease in $p(H_2)$ therefore initiates a transition from the reactive, more or less adsorbate free state of the surface to an inactive oxygen covered state, blocking hydrogen adsorption and thus poisoning the catalyst. The onset of oxygen adsorption coincides with the start of the reaction front III $\rightarrow$ II, as can be seen by comparison with the VO_x trace. Apparently the front is triggered by oxygen adsorption on Rh(111), explaining why it nucleates at the phase boundary. The front, in turn, initiates the expansion (oxidation) of the oxide phase; one could speculate that the structural integrity

of the oxide is lifted, facilitating adsorption or spill-over of oxygen from V-free rhodium phase.

Before reaching its final value, the Rh(111) brightness trace passes through a maximum followed by a local minimum. The region in which the intensity was integrated (see figure 3.13 (a), last image) was selected carefully to exclude any of the small VO_x islands which start forming at the transition to state I (~200 s). However, the Rh(111) brightness maximum coincides with the onset of this roughening process of the oxide phase. The roughening (see figure 3.13 (c)) appears to be a break-up of the smooth film into nanoscale islands. In the LEEM images at 199, 211 and 330 s a growing fraction of such islands populates the previously uncovered region; apparently they can drift onto the Rh(111)-O surface. This observation leads to the interpretation that the growing oxygen coverage on the Rh(111) surface actually causes the break-up of the oxide film.
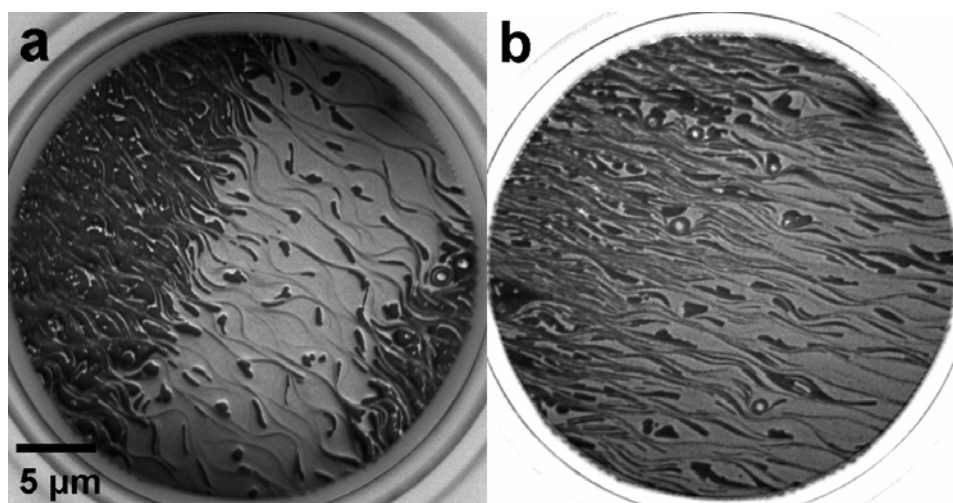
Figure 3.14: Normalized LEEM images (5 eV) illustrating the homogenization of the surface in oxygen. (a) 10 min after figure 3.13 at 480°C, $p(O_2) = 5 \cdot 10^{-7}$ mbar; location and focus of the microscope were slightly adjusted. (b) Former phase boundary 30 min after a similar experiment, recorded at 70°C and $6 \cdot 10^{-7}$ mbar O_2 (sample heating off after experiment); in the left side of the image, the former location of a stripe, the oxide concentration (dark) is still much higher.

The break-up of the oxide film initiates a surface homogenization process lasting for several hours; the mesoscopic islands (stripes) decompose into a microscopic island structure. Illustrating this, figure 3.14 displays a two LEEM images: (a) shows the surface 10 min after the experiment of figure 3.13 (sample slightly moved), and 3.14 (b) shows a former phase boundary about 30 min after shutting off hydrogen in a similar experiment. This process resembles another phenomenon reported on a smaller length

scale: upon exposing islands of the $(5 \times 3\sqrt{3})$-rect $V_{13}O_{21}$ structure (see section 3.1) to oxygen, flat V_6O_{12} clusters evaporate onto the Rh(111) surface [7]. However, it turned out that this evaporation can also be triggered by H_2 exposition of the (5×5)-oxide [6]; it is an intermediate reaction step, and thus a completely different phenomenon compared to the fragmentation process illustrated in figure 3.13 (c).

The spreading of vanadium oxide onto previously oxide-free Rh(111) upon reducing the hydrogen pressure resembles a surface wetting process. Indeed a reversible wetting/dewetting behavior was reported for VO_x on Pd(111) while changing from oxidative to reducing conditions [24]. The (2×2)-V_2O_3 has a V-density of 0.5 V/Pd and thus covers the whole surface at $\Theta_V = 0.5$ MLE. Upon oxidation other structures form, most of which exhibit higher V-densities than 0.5 V/Pd. Consequently, the initially closed oxide layer contracts, forming isolated islands and leaving bare metal surface. This process, termed dewetting, is rather similar to the state transition III → II in figure 3.13. There oxidation apparently leads to the formation of a VO_x structure which, in contrast to the Pd system, is less dense and thus covers a bigger fraction of the surface than before oxidation.

The state transition II → I (see figure 3.13), associated with breaking up the closed VO_x layer into nanoscale islands, can be interpreted considering the phase boundary lines separating V-free from V-covered regions. Numerous boundary lines are generated during the break-up, which is presumably initiated by adsorption of oxygen on Rh(111), as stated above. From this correlation it can be concluded that the formation of an oxygen adlayer on Rh(111) reduces the phase boundary energy, which in turn facilitates formation of small islands. Those are then slowly redistributed on the surface, approaching a more homogeneous state.

To further rationalize the fragmentation/redistribution behavior, the following idea is proposed. Taking the traditional concept of surface wetting as starting point, the interfacial free energies of the 2-dimensional phase boundaries substrate/gas, substrate/overlayer and overlayer/gas are considered [25]. The limit case is complete wetting with a contact angle of 0°, so a flat overlayer covers the whole substrate, separating it from the gas phase (see figure 3.15). A monoatomically thick and structurally open overlayer introduces a problem: the 2-dimensional phase boundaries are not clearly defined anymore. The concept breaks down.

How can the wetting concept be extended into the sub-monolayer range? A *gedankenexperiment* might help. If one considers a complete wetting layer of an arbitrary substance on an arbitrary substrate and starts to remove material, its thickness will be reduced to the point where it cannot entirely separate the gas phase from the substrate anymore. This is the limit of the macroscopic concept. One has to restrict the possible variations to two dimensions now. Upon further removal of material the overlayer can sustain its structure only if it reduces its area. This means creating free substrate surface, i.e. dewetting occurs. A perfectly wetting layer on the contrary would reduce its density (atoms per area) in order to still cover the whole substrate.

One could imagine a 2-dimensional gas where all interatomic distances are allowed, but in contrast to that a 2-dimensional solid or liquid is considered here: islands of variable size will be surrounded by free substrate area. Two limit cases can be formulated. Full fragmentation into the smallest possible island size or cluster corresponds to complete wetting. The largest possible island containing all overlayer atoms corresponds to complete dewetting. Partially fragmented states could be characterized by the mean island size.
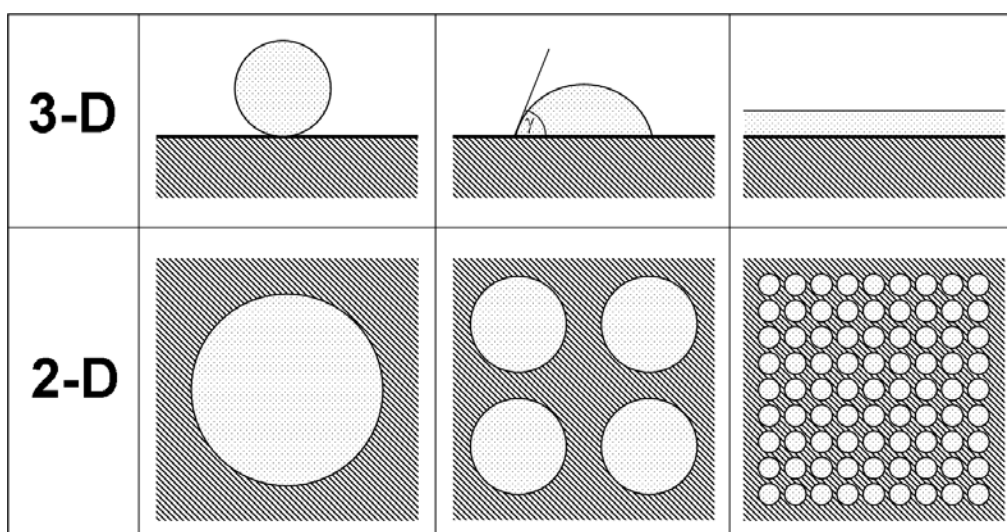
Figure 3.15: Scheme illustrating the proposed analogy between surface wetting (3-dimensional, side view) and fragmentation (2-dimensional, top view). From left to right: dewetting/defragmentation, partial wetting/fragmentation, complete wetting / full fragmentation. The small islands there represent a size limit below which the overlayer would have to be treated as a 2-dimensional gas. γ is the contact angle.

Assuming that kinetic barriers do not play a role, there should be a fragmentation equilibrium. In addition to interfacial energies one has to consider the line tension given by the boundaries of islands, which indeed represents the decisive contribution is the

simple example illustrated in figure 3.15: in the 2-dimensional case the total boundary length is the only variable.

The experiment presented above is more complex than the model system just introduced here, essentially because the O_{ad} coverage of the Rh(111) substrate changes, and therefore its surface tension. Anyway, the state transition II $\rightarrow$ I can be interpreted in terms of the proposed concept, with O_{ad} acting as a 1-dimensional analogon of a surfactant, enforcing fragmentation.

However, considering the reverse process, removing the surfactant O_{ad} by exposition to hydrogen alone does not trigger the phase separation. Supposedly O_2 and H_2 have to be supplied continuously, in order to stabilize the oxide in the required state, which is the (2×2)-structure.

An H_2 downramping experiment is shown in figure 3.16, observing a vanadium oxide stripe in µ-LEED. This experiment is analogous to the LEEM experiment from figure 3.13, at slightly different pressure and temperature.

The VO_x-covered phase exhibits a sequence of diffraction patterns upon reducing $p(H_2)$, as illustrated in figure 3.16 (a). The initial (2×2)-pattern changes into a *split*-(2×2) pattern, i.e. the two are related by splitting of the half-order beams. More detail is visible at 36 eV in (b) and in the scheme (c). Later, all overlayer spots disappear for some time, leaving only the (1×1)-beams of the substrate. Finally the $\sqrt{7}$-pattern emerges at a low hydrogen partial pressure. This evolution can be followed by the intensity traces of the overlayer spots displayed in (d).

The system states IV − I indicated in figure 3.16 (a) have been assigned by comparison with the LEEM-experiment (figure 3.13). In principle a direct assignment should be possible based on the ratio of partial pressures, but in the LEED experiment oxygen was supplied from a capillary in front of the specimen, so that the true oxygen pressure in front of the surface can just be estimated. However, the assignment for state IV and I at the starting/end points is clear anyway; the *split*-(2×2) pattern forms directly out of the (2×2)-pattern (see figure 3.16 (d)), just like state III out of IV (LEEM). The (1×1) substrate pattern represents a disordered overlayer and can hence be safely assigned to the transition III $\rightarrow$ II, associated with the continuously expanding VO_x film (see figure 3.13). It remains unclear whether the $\sqrt{7}$-structure already forms in state II, before the closed film breaks up into fragments, or during fragmentation.
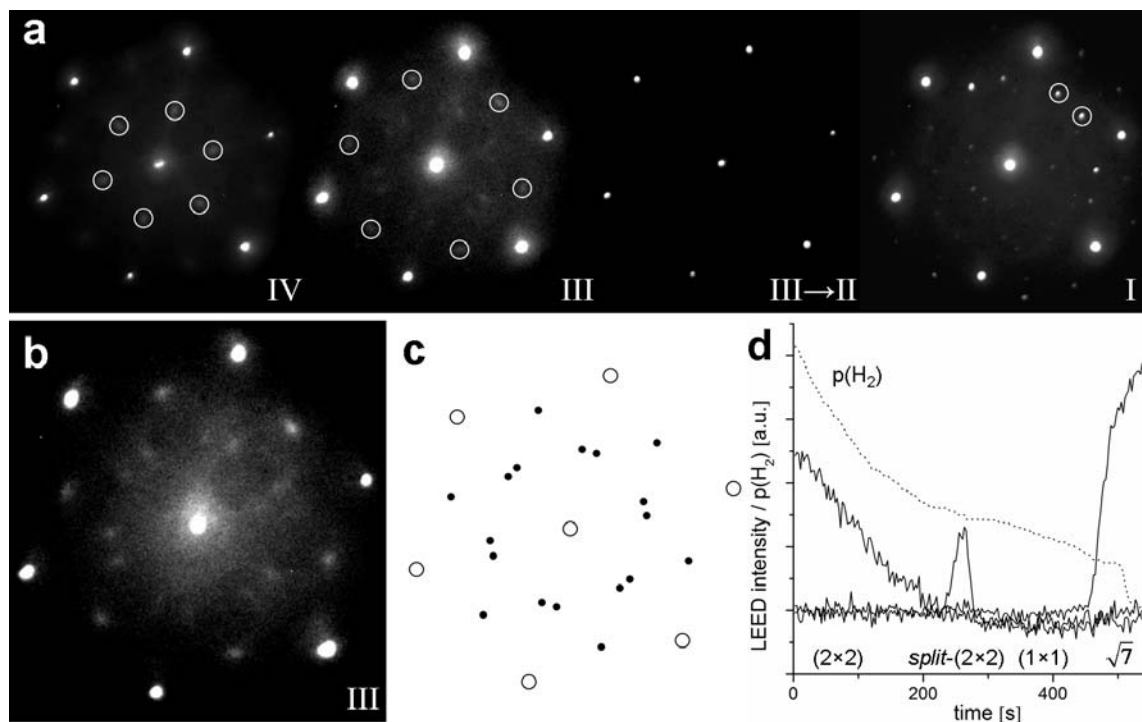
Figure 3.16: (a) Sequence of LEED images at 47 eV following an H_2 downramping experiment at 485°C and ~8·10^{-7} mbar O_2, $\Theta_V = 0.1$ MLE; p(H_2) is decreased from 8.4·10^{-7} mbar to zero. The contrast of the weak raw data was increased strongly to show the diffraction patterns; all available images were averaged. (b) *split*-(2×2) pattern at 36 eV from a reproducing experiment. (c) Scheme of the *split*-(2×2) pattern; ○ represents substrate spots, and • overlayer spots. (d) Intensity traces for the overlayer structures; the evaluated spots are indicated in (a). The $\sqrt{7}$-intensity was divided by a factor of 3 to allow better presentation, backgrounds were subtracted. The p(H_2) trace is given as dotted line.

The *split*-(2×2) pattern is not just a transient, but can be stabilized at constant pressure. Such a structure is reported here for the first time in the system Rh(111)/VO$_x$. The diffraction pattern itself is known from adsorption studies of CO on Rh(111) where it appears at coverages between 0.25 and 0.75 MLE, while at saturation ($\Theta_{CO} = 0.75$ MLE) a regular (2×2)-pattern is observed [26]. Carbon contamination can be ruled out as origin of these patterns for Rh(111)/VO$_x$: sufficient CO coverages cannot accumulate at ~500°C in presence of oxygen, since the desorption temperature of CO is around 200°C [27]. Significant contamination would have been detected with XPS anyway.

A *split*-(2×2) pattern can be interpreted in two ways. It could originate from a hexagonal, incommensurate overlayer, exhibiting double diffraction. This model was disproved for CO [26], and it is also unlikely for VO$_x$: the elementary cell is quite small (~170 % of the substrate cell) and would contain at least one vanadium atom, which

leads to a V-density of ≥ 0.6 V/Rh. This is in contradiction to the LEEM investigation (figure 3.13), from which a density equal to the (2×2)-V_2O_3 (~0.5 V/Rh) is expected.

The alternative interpretation derives from a regular (2×2)-structure: patches of the (2×2)-overlayer are arranged on the surface as antiphase domains, separated by domain walls (possibly uncovered rhodium). This leads to large unit cells involving several domains; for the case of CO adsorption this is described in detail in [26]. An analogous model can explain the VO_x *split*-(2×2) pattern. The (2×2)-V_2O_3 is assumed to be stabilized by randomly distributed vacancies (see section 3.4), which might rearrange into domain walls in a disorder-order transition, yielding the *split*-(2×2) structure.

3.6 Stripe pattern formation and morphology

PEEM images show anisotropic stripe patterns, for example in the figures 2.9 or 3.5. The formation of such anisotropic patterns on the isotropic Rh(111) substrate is rather unexpected. One might think that the crystallographic directions of the substrate determine the symmetry; in that case three different stripe directions are to be expected, deviating from each other by 60° rotation. Regions with different stripe orientations are observed indeed, but the deviations appear random, for example ~90° in figure 3.17.
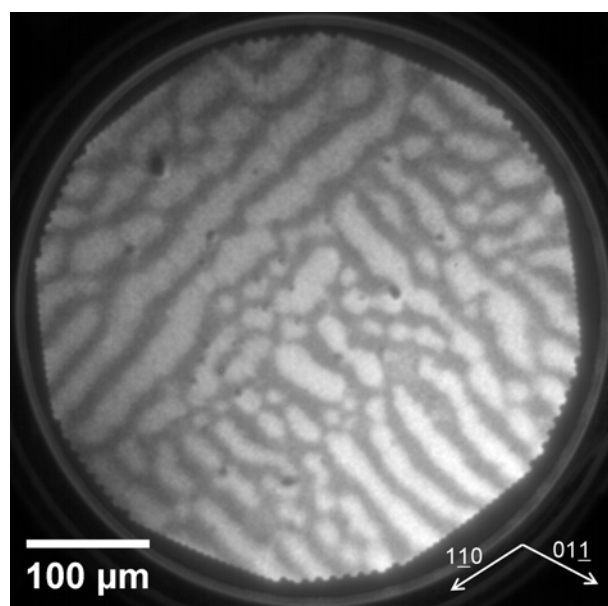
Figure 3.17: PEEM image of a stripe pattern under reaction conditions at 500°C, $p(O_2) = 2\cdot10^{-6}$ mbar, $p(H_2) = 6\cdot10^{-7}$ mbar, $\Theta_V = 0.2$ MLE. The boundary between two regions with different stripe orientation is displayed. Crystallographic directions are indicated for comparison (determined by LEED).

The influence aligning the stripe patterns is revealed by LEEM. In the images shown in the previous sections the phase boundaries are always orientated more or less perpendicular to the mean direction of the step bunches. This is established by figure 3.18 (a), showing four regions with deviating step bunch directions, the VO$_x$ stripes always being aligned perpendicular. The circular surface defects are rhodium mesas.
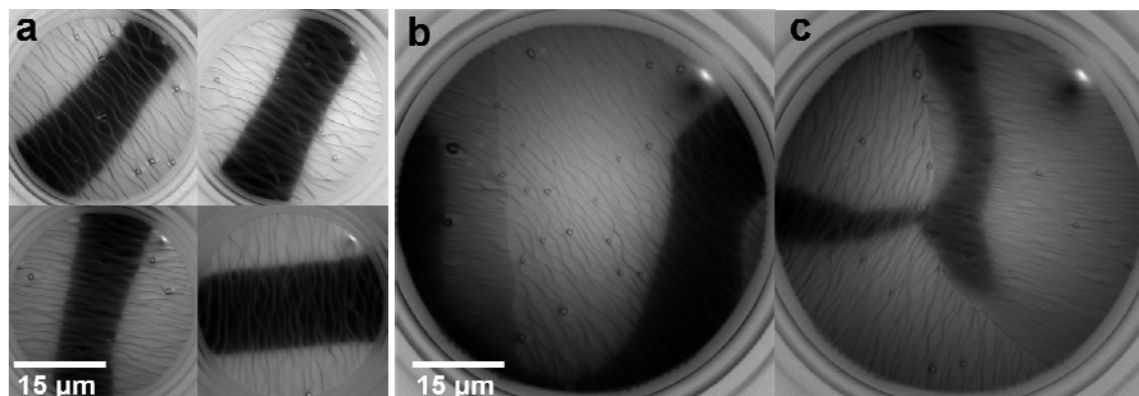

Figure 3.18: Normalized LEEM images illustrating the relative orientations of stripes and step bunches at 480°C, $p(O_2) \approx 8 \cdot 10^{-7}$ mbar, $p(H_2) = 7 \cdot 10^{-7}$ mbar, $\Theta_V = 0.1$ MLE. (a) Regular case with perpendicular stripes with respect to step orientation; four regions with different step bunch directions are shown. (b, c) Large-scale images demonstrating the influence of grain boundaries, which show up as a change in the orientation of step bunches. The circular defects are rhodium mesas.

In figure 3.18 (b) and (c) it is shown that the specimen is actually not a single crystal, but composed of several individuals (grains). The crystallographic orientations of the grains are close to each other. Just slightly tilted (111)-LEED patterns result, but the differences are apparently sufficient to induce strong deviations in step bunching.

So the different stripe directions are closely related to differently orientated step bunches on the grains. In addition, the grain boundaries exhibit a directing influence. In figure 3.18 (b) the stripe on the right grain enters the image perpendicular to the step bunches, but is bent upon approaching the grain boundary. In (c) the vertical stripe is partially attached to the boundary from one side, while the horizontal stripe is misaligned to the step bunches, approaching and merging with the vertical stripe across the grain boundary. In principle, the influence of the grain boundaries can be easily understood. It is demonstrated below that the stripe direction is determined by the formation dynamics via on-terrace diffusion of VO$_x$; grain boundaries acting as diffusion barriers should therefore have an orientating effect. According to figure 3.18, however, the details are complicated, as the stripes are "attracted" or "repulsed" by the boundaries. Probably mass transport is inhibited to a different extent in both directions.

The formation of a VO$_x$ stripe can be followed in LEEM. The residues of a stripe from a preceding experiment, displayed in figure 3.19 (a), act as nucleation center for a new stripe to be formed upon returning to reaction conditions. Hydrogen is raised at constant p(O$_2$); when the system reaches state IV, vanadium from small, distributed islands is transported back to the stripe and condenses there. The transport itself can barely be observed in LEEM, because low local concentrations of vanadium are not visible. As shown in figure 3.19 (b) just the high VO$_x$ concentrations approaching the location of the stripe (c) are imaged dark and fuzzy. Apparently the small VO$_x$ islands are not stable under the given conditions, so they probably decompose to molecular sized traveling clusters, as described in the literature [2, 4, 6, 7]. However, figure 3.19 clearly indicates that vanadium mass transport, i.e. diffusion, preferentially occurs along the mean direction of the step bunches.
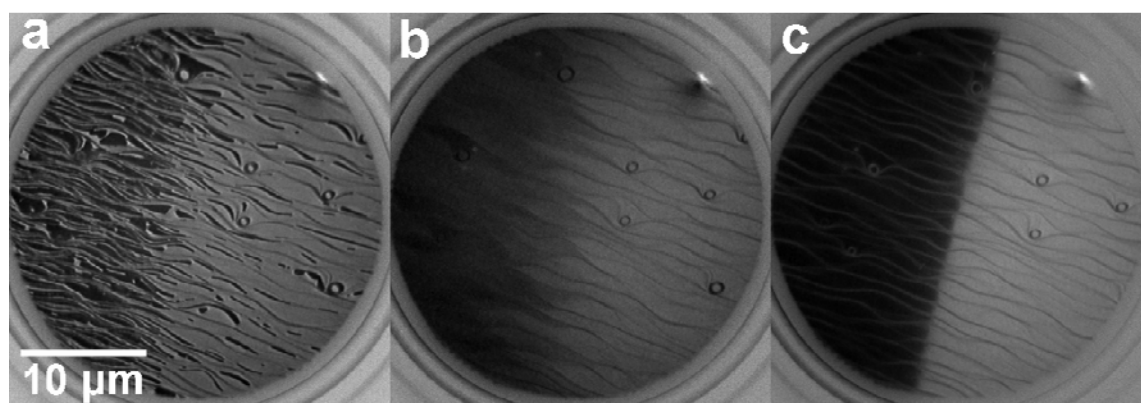
Figure 3.19: (a) LEEM image (5 eV) of VO$_x$ stripe residues at 490°C, ~8·10^{-7} mbar O$_2$, Θ_V = 0.1 MLE. (b) Stripe formation while introducing hydrogen at p(H$_2$) = 3.2·10^{-7} mbar. (c) Readily formed stripe, about 6 min later, at p(H$_2$) = 8.1·10^{-7} mbar.

A consequence of the diffusion anisotropy shows up in between (b) and (c) of figure 3.19, during formation of the phase boundary line. The detail images in figure 3.20 (a) show how a smooth phase boundary is aligned, starting from a sawtooth-like initial shape with the individual "teeth" being separated by step bunches. Apparently diffusion across the step bunches is inhibited, because otherwise the straight front line would result immediately. Nevertheless, vanadium can be exchanged in some way during the alignment process, as shown in the following. Imaging a similar experiment at higher magnification, single atomic steps are resolved, as displayed in figure 3.20 (b). The mean direction of the step edges, and hence the direction of the terraces, is identical to the mean direction of the step bunches and mass transport. Diffusion on terraces is the

most efficient channel. However, single step edges seem not to represent great barriers for diffusion, since the VO_x coverage on adjacent terraces changes in parallel, suggesting rapid material exchange. Since a step bunch is just a series of close-by steps, one can conclude that vanadium can cross step bunches at a lower rate; this is a possible mechanism for material exchange between the regions separated by step bunches.
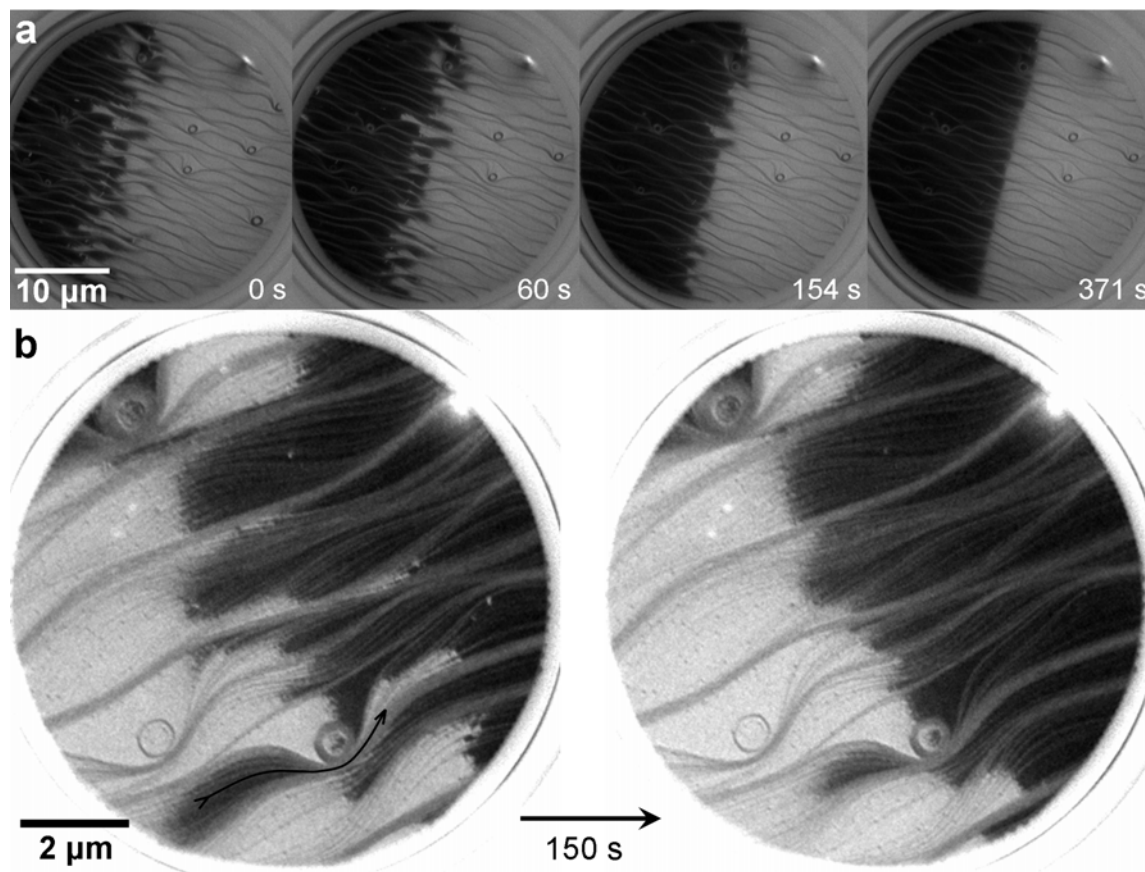

Figure 3.20: (a) Sequence of LEEM images (5 eV) showing the alignment of a phase boundary at 490°C, $p(O_2) \approx 8 \cdot 10^{-7}$ mbar, $p(H_2) = 8 \cdot 10^{-7}$ mbar, $\Theta_V = 0.1$ MLE. The sample was slightly moved between the first two images. (b) Similar experiment (475°C, $p(O_2) = \sim 9 \cdot 10^{-7}$ mbar, $p(H_2) = 1.1 \cdot 10^{-6}$ mbar) showing more detail at higher magnification; single atomic steps are resolved. The arrow indicates a possible diffusion way along a step bunch.

Figure 3.20 (b) also suggests an additional pathway. Step bunches are interconnected by individual terraces, which become very narrow as they converge into a step bunch. Therefore, step bunches act as bottlenecks for on-terrace diffusion along step edges. An example for this behavior is indicated by a black arrow: apparently VO_x (dark) flows from one region into another one, both only connected by a step bunch. This "bottleneck diffusion" mechanism could also contribute to the vanadium exchange between areas separated by step bunches, since individual terraces from both sides of a

step bunch meet inside of this step bunch. There, material can move to a terrace from the other side by crossing just one or a few step edges; subsequent transport then occurs via on-terrace diffusion.

Vanadium oxide must exhibit some kind of interaction across the step bunches in order to facilitate the alignment process shown in figure 3.20. This interaction causes a minimization of the phase boundary length; hence the phenomenon is probably closely related to the fragmentation/defragmentation process discussed in section 3.5. One of the conclusions reached there is that VO_x-covered surface area bordering bare Rh(111) gives rise to a high phase boundary energy. Probably this still holds if a step bunch separates both areas.

From the experiments presented in figure 3.19 and 3.20 it can be concluded that the orientation of the stripes perpendicular to step bunches arises from the pattern formation dynamics. This conclusion is corroborated by another observation. If a pattern is formed at high pressures around 10^{-4} mbar and exposed to the reaction for some time, the stripe orientation changes.
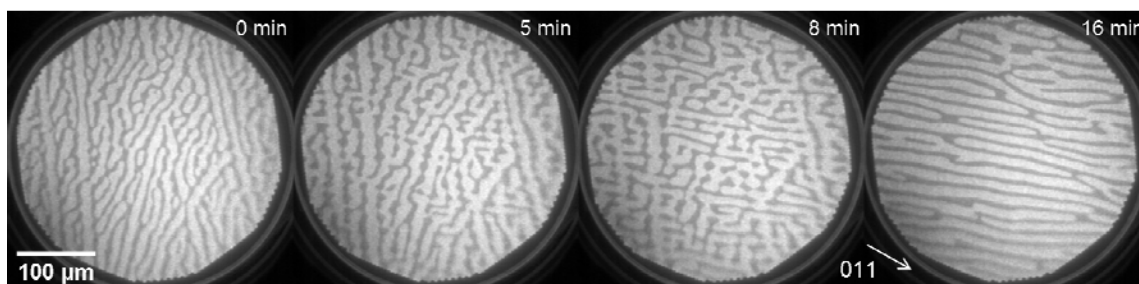
Figure 3.21: Series of PEEM images at 500°C, $p(O_2) = 1.6 \cdot 10^{-4}$ mbar, $p(H_2) = 8 \cdot 10^{-5}$ mbar, $\Theta_V = 0.2$ MLE. The orientation of the pattern is rotated into a parallel alignment to the step bunches. A crystallographic axis (determined by LEED) is indicated for comparison.

Figure 3.21 shows the rotation of a stripe pattern by about 90°. The orientation in the initial state is not completely well defined, probably due to the local step bunch structure. In the final pattern the stripes are aligned perpendicular to the initial orientation and hence parallel to the step bunches; as indicated in the figure, there is no relation with the crystallographic directions. The final orientation is thermodynamically favored, and thus the initial one is of kinetic origin.

Stripe reorientation was not observed below $5 \cdot 10^{-5}$ mbar, patterns just coarsen with time (details in the next section). The difference could be of thermodynamic or

kinetic nature. A different oxide might be produced at high pressures, which favors parallel alignment to the step bunches. The other possibility is that parallel alignment is the true stationary state at all pressures; this state would just not be reached at low pressures within the experimental timescale of several hours, due to too slow kinetics.

A large effect of the total pressure on the pattern morphology, namely reorientation, is demonstrated in figure 3.21. An effect of the partial pressure ratio, the stripe fragmentation at excess O_2, is discussed in detail in section 3.5. No drastic effects are observed exposing a stripe pattern to high partial pressures of hydrogen, the patterns are preserved even at 500-fold excess ($1 \cdot 10^{-6}$ mbar O_2, $\sim 5 \cdot 10^{-4}$ mbar H_2, 500°C). A rather subtle change in the morphology occurs: the oxide stripes become thinner. The two PEEM images in figure 3.22 show the same region, before (a) and after (b) increasing $p(H_2)$ by a factor of 12. Brightness changes are caused by a reduced oxygen coverage on Rh(111), and the darker, VO_x-covered area is probably brightened by stray light from the bright area. Besides that, the dark regions become smaller, as demonstrated by a deviation image (c) produced by digital image processing (division of (b) by (a)). The previously dark stripe boundaries appear bright, indicating a slight expansion of the bright phase. It has to be noted that the image visualizes the difference just qualitatively; quantitatively it is not reliable, due to artifacts produced by uneven illumination and an imperfect drift correction (see lower left corner). However, the oxide-covered fraction of the surface is becomes smaller, caused either by an increased vanadium density inside the stripes, or a higher V surface concentration outside. This could not be clarified with XPS for instrumental pressure limits.
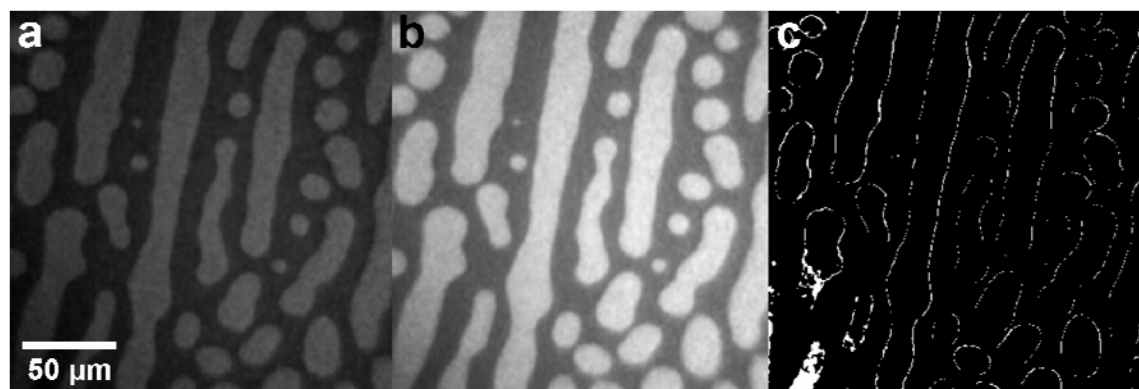

Figure 3.22: Drift-corrected PEEM images showing a VO_x pattern on the same region at 500°C, $p(O_2) = 5 \cdot 10^{-5}$ mbar, and (a) $2.4 \cdot 10^{-5}$ mbar H_2, (b) $3 \cdot 10^{-4}$ mbar H_2. A deviation image (c) has been generated by adjusting the same contrast range to the raw images and dividing (b) by (a).

All stripe patterns presented up to here were formed by raising hydrogen to high pressures corresponding to surface state IV. However, pattern formation also occurs at lower $p(H_2)$ in surface state III, as already mentioned in section 3.2. The example presented in figure 3.23 deviates significantly from the patterns formed in state IV. Most features are perfectly straight lines, orientated in random directions. The pattern appears to represent a decoration effect; maybe residues of scratches from the polishing process are highlighted by the VO_x distribution. Pattern formation is also about one order of magnitude slower, compared to state IV at higher hydrogen pressure and, apart from that, equal conditions. An explanation for both differences could be low VO_x diffusivity in state III, suppressing the organization of the oxide into stripes.
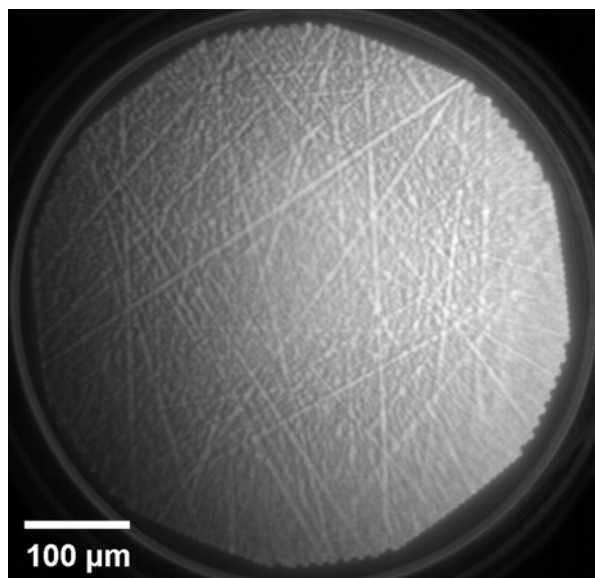
Figure 3.23: PEEM image of a VO_x pattern formed in surface state III, at 500°C, $p(O_2) = 1.6 \cdot 10^{-4}$ mbar, $p(H_2) = 5.5 \cdot 10^{-5}$ mbar, $\Theta_V = 0.2$ MLE. The lines are orientated randomly.

3.7 The length scale of stripe patterns

In figure 3.21 a stripe pattern is shown to change with time. Changes occur at lower pressures as well, but without rotation of the pattern.

Exposition of a freshly formed stripe pattern to constant reaction conditions in system state IV leads to substantial coarsening, as illustrated in figure 3.24 (a). After formation many narrow stripes are present, merging to less, broader stripes upon time. This development is fast at the beginning and slows down as it proceeds, as shown in (b): the experiment can be quantified by putting section lines perpendicular to the

patterns mean direction and defining an average wave number *k* as the number of crossed stripes, divided by the corresponding length.
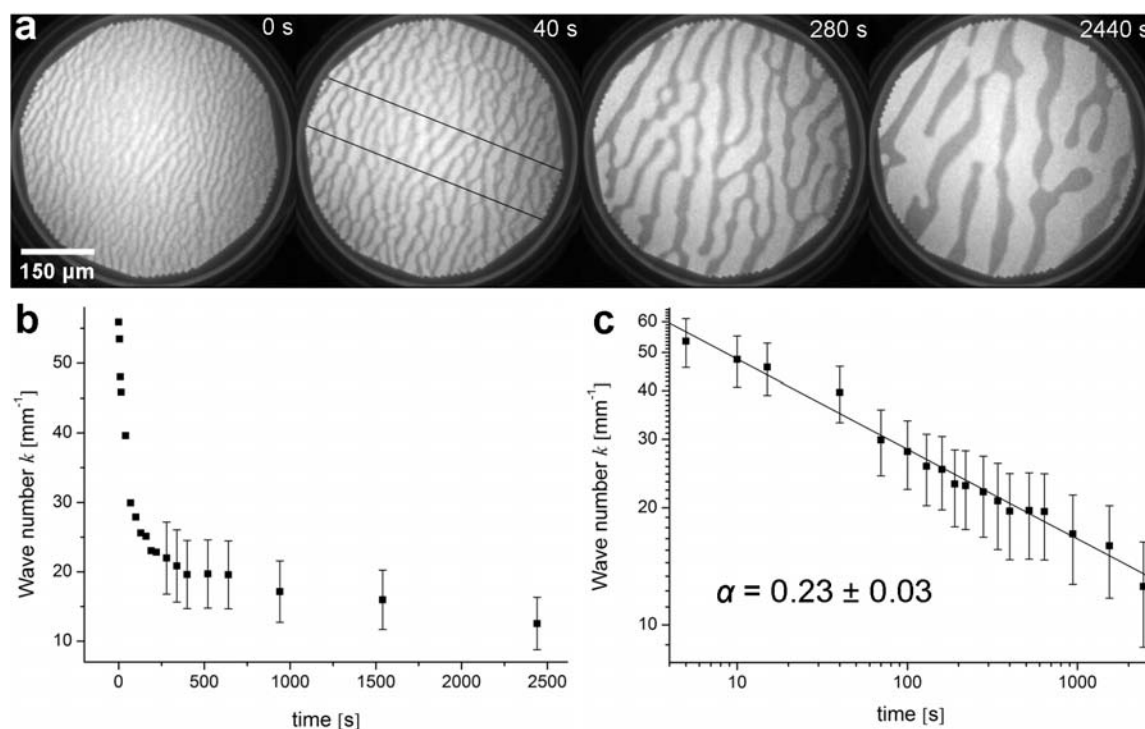

Figure 3.24: Temporal development of a freshly formed stripe pattern under reaction conditions at 500°C, $p(O_2) = 1 \cdot 10^{-5}$ mbar, $p(H_2) = 4 \cdot 10^{-6}$ mbar, $\Theta_V = 0.2$ MLE. (a) Sequence of PEEM images for illustration. (b) Plot of the average wave number vs. time; the data points are taken from counting intensity minima of line profiles, drawn as indicated in (a), second image. The error is given by the square root of counts, error bars are not shown where the graph is steep for visual reasons. (c) Double logarithmic plot of the same data; the straight line represents the best linear fit.

A similar behavior is known for submonolayer films of Au or Au + Pd on Rh(110) exposed to the $H_2 + O_2$ reaction [28]. Reactive phase separation was observed, driven by the chemical affinity between rhodium and oxygen; stripe patterns of Au-rich and Au-poor domains were observed to form and coarsen with time. The phenomenon was associated with spinodal decomposition. This term originally describes the demixing of a liquid mixture quenched to lower temperature into a miscibility gap, when phase separation can be initiated by small concentration fluctuations [29]. It is tempting to apply that concept to Rh(111)/VO$_x$ as well, as the systems are quite similar: in both cases low-index rhodium surfaces are partially covered with material of significantly lower catalytic activity which gets redistributed when exposed to the $H_2 + O_2$ reaction, forming stripe patterns coarsening with time. Interpreting this as spinodal decomposition implies that applying reaction conditions is analogous to quenching a mixture into a

miscibility gap. This interpretation is supported by the results of section 3.5. As demonstrated there, stopping the hydrogen supply and thus the reaction leads to fragmentation of the oxide phase which is clearly separated from VO_x-free area, into distributed nanoscale islands. This resembles a mixing or solvation process, with an oxygen adlayer on Rh(111) acting as a 1-dimensional analogon of a surfactant, as concluded from LEEM data (figures 3.13 – 3.15). Removing this "surfactant" under reaction conditions can indeed be considered as analogous to quenching a mixture into a miscibility gap. The driving force for pattern coarsening is supposedly the same as for condensation of nanoscale islands into stripes: the total length of phase boundary lines, and hence their energy, is minimized in absence of an oxygen overlayer on Rh(111).

After initiating phase separation, a pattern is formed which coarsens as expected for spinodal decomposition. The domain size of the pattern increases with time according to a power-law dependence [30]. Taking the wave number k as a measure for the inverse domain size, one expects

$$k(t) \sim t^{-\alpha} \tag{3-2}$$

to be the scaling law, with α as characteristic scaling exponent. A double logarithmic plot yields a straight line with slope α, as shown in figure 3.24 (c) with $\alpha = 0.23 \pm 0.03$.

A scaling exponent α of roughly ¼ was verified at lower pressure ($p(O_2) = 5 \times 10^{-6}$ mbar, $p(O_2) = 2 \times 10^{-6}$ mbar, $\alpha = 0.25 \pm 0.05$). In principle, the value allows interpretation regarding the coarsening mechanism. In the case of simple *Ostwald ripening* limited by surface diffusion $\alpha = \frac{1}{3}$ is to be expected [31], while the exponent ¼ is the theoretical value for an island coalescence mechanism limited by terrace diffusion [31, 32]. However, experimental values of such exponents depend also strongly on the particular conditions, e.g. for copper islands on Cu(100), where values between 0.12 and 0.25 were observed [33].

Figure 3.25 clearly reveals the general mechanism as stripe coalescence by direct observation, while the microscopic details of motion can only be guessed. The stripes are remarkably mobile, considering their size. Concerted movement of large oxide patches would require huge activation energies and can therefore be excluded. In section 3.4 it is postulated that the stripes are composed of honeycomb-lattice (2×2)-V_2O_3 stabilized by vacancies; one can speculate whether those vacancies are the diffusing species responsible for mass transport.
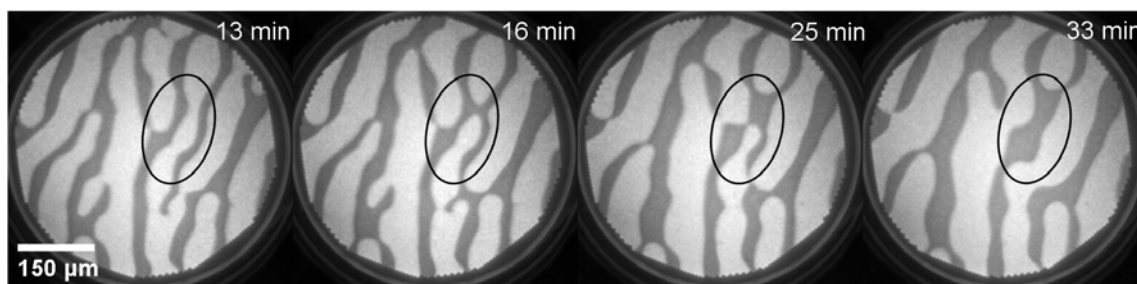
Figure 3.25: Series of PEEM images revealing the mechanism of pattern coarsening; in the encircled region two stripes coalesce. T = 500°C, p(O$_2$) = 5·10^{-6} mbar, p(H$_2$) = 2·10^{-6} mbar, Θ$_V$ = 0.2 MLE. The given time refers to the initiation of pattern formation.

Comparing the reactive phase separation observed during the H$_2$ + O$_2$ reaction for Au and Au/Pd on Rh(110) to the present phenomenon, one recognizes a difference: in contrast to Rh(111)/VO$_x$ the coarsening process freezes within 30 min, yielding a stationary pattern [28]. This freezing of pattern coarsening agrees with theoretical expectations, since it has been predicted that spinodal decomposition can get "pinned" (= frozen) in presence of a chemical reaction [30]. For the resulting stationary structures on Rh(110)/Au/Pd a power-law dependence of the wave number on the total pressure was found [28]:

$$k(p) \sim p^{\alpha'} \tag{3-3}$$

with α' = 0.18 ± 0.02. This result was interpreted as a consequence of freezing of spinodal decomposition, since it had been predicted that the stationary inverse domain size should in that case depend on the *reaction rate constant* via a power law [30]. Courageously assuming that this is also valid for the *reaction rate* and furthermore for the total pressure (at constant T and H$_2$:O$_2$ ratio), the power-law dependence in equation (3-3) was explained, taking k as a measure for the inverse domain size [28]. The authors also estimated an expectation value of α' = ¼ from theoretical considerations, which is comparable to the experimentally obtained exponent of 0.18.

In figure 3.24 (b) the wave numbers appear to approach a constant value at first sight, but the double logarithmic plot (c) reveals that the coarsening proceeds without any indication of freezing. Even after 3 hours at constant reaction conditions no true stationary pattern could be observed. So instead of stationary stripe patterns, their initial state directly after formation is compared at different total pressures in figure 3.26. In several experiments, each starting with a homogenized surface (O$_2$-treatment at 750°C,

$2 \cdot 10^{-7}$ mbar), a designated value of $p(O_2)$ is adjusted at 500°C; then $p(H_2)$ is raised up slowly (within ~1 min) to an O_2:H_2 ratio of 2.5:1, initiating pattern formation. The first images featuring visible patterns are used for the double logarithmic plot in figure 3.26. Also for the system $Rh(111)/VO_x$ a power-law dependence according to equation (3.3) is found. This is another similarity to $Rh(110)/Au/Pd$, though comparing frozen patterns to not-frozen ones; here the exponent is $\alpha' = 0.33 \pm 0.05$.
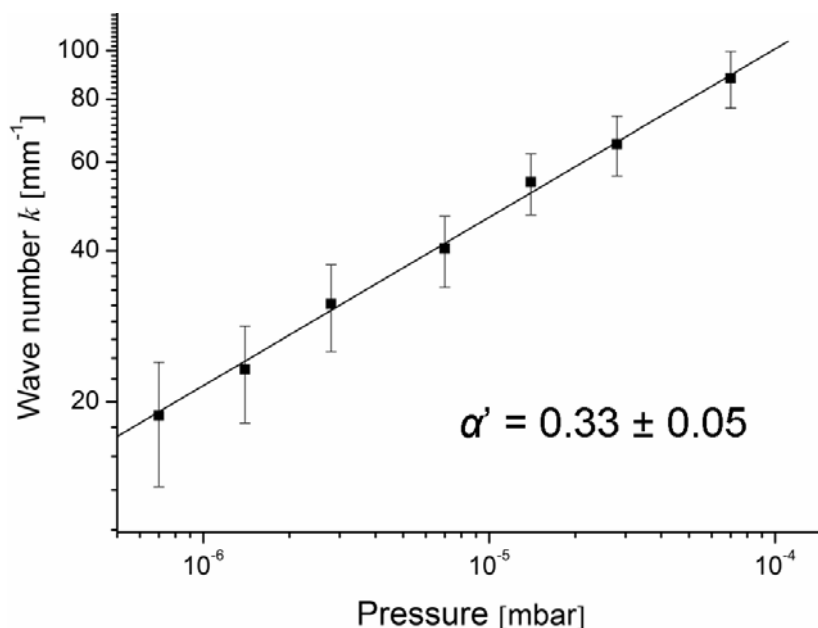
Figure 3.26: Double logarithmic plot of the wave number vs. pressure at 500°C, $\Theta_V = 0.2$ MLE; the O_2:H_2 ratio is 2.5:1 for all data points. The data is extracted from PEEM images as described for figure 3.24; for experimental details see text.

An additional significant influence on the length scale of stripe patterns becomes apparent performing pressure-jump experiments. If at 500°C and $1 \cdot 10^{-4}$ mbar O_2 pattern formation is initiated by slowly increasing $p(H_2)$ as in figure 3.26, wave numbers about 100 mm^{-1} are observed. If instead an excess of hydrogen ($4 \cdot 10^{-4}$ mbar, O_2:H_2 = 1:4) is adjusted as quickly as possible (within a few seconds), a finer pattern with $k \approx 280$ mm^{-1} is observed, as displayed in figure 3.27. This pattern exhibits the shortest wavelength found in this study. Even higher wave numbers are probably available, going beyond the experimental pressure limit of 10^{-3} mbar. It is not clear whether the higher hydrogen partial pressure or the speed of changing the latter during pattern formation is the particular reason for the high wave number; for the case of $Rh(110)/Au/H_2 + O_2$ it was stated that quickly changing parameters produce nanoscopic patterns, while slow changes lead to mesoscopic ones [34].

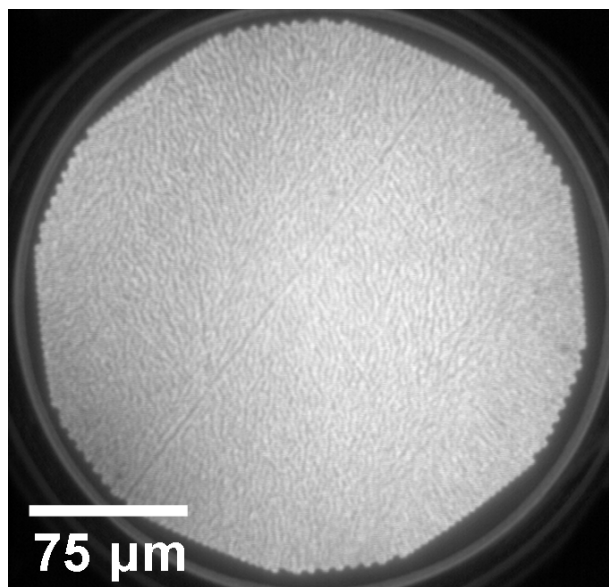Figure 3.27: Finest stripe pattern ($k \approx 280$ mm^{-1}) observed during this study, generated by a p(H$_2$)-jump experiment at 500°C, p(O$_2$) = 1·10^{-4} mbar, p(H$_2$) = 4·10^{-4} mbar.

The question remains whether the coarsening of the VO$_x$ patterns proceeds until macroscopic phase separation is reached (regular spinodal decomposition), or if the influence of the reaction is strong enough to freeze the patterns at some point to a fixed wavelength ("pinned" spinodal decomposition = reactive phase separation). It might be possible to clarify that matter by a long-term experiment, but in case of long transients it is always difficult to separate true stationary states from surface roughening or other slow processes modifying the catalytic properties. From theoretical work on spinodal decomposition [30] a stationary state can be expected in presence of a reaction. Also a theoretical model more specific to the present system exhibits reactive phase separation: a bimolecular surface reaction was considered, in presence of an additional adsorbate (here: vanadium) interacting strongly with one of the reactants (here: oxygen) [35, 36]. It was predicted that, regardless if the additional species is a promoter, a poison or inactive, instabilities of spatially uniform states can be found, leading to formation of stationary patterns. However, the VO$_x$ stripe patterns are termed quasi-stationary for now.

3.8 Microstructuring

The discovery that a catalytic reaction causes (quasi-) stationary patterns of vanadium oxide or gold to form on rhodium surfaces, and that the morphologies of those

patterns can be tuned by the reaction conditions (see sections 3.6, 3.7 and [28]), raises the question of exploiting the effect for microstructuring catalytic surfaces This could be an alternative to lithographic techniques.

In the case of VO_x there are limitations. If a pattern is formed under reaction conditions and the hydrogen supply is stopped, the stripes broaden and break apart into nanoscale islands (see section 3.5). Dense stripes instantly blend with each other; only for coarse patterns an unstable structure with broadened stripes remains (shown in figures 3.8 and 3.14 (a)), which can be frozen cooling down to room temperature. In order to circumvent the stripe breakup and broadening it was tried to cool down the sample while still supplying both gases. This procedure turned out to be not feasible: the sample gets quickly covered by oxygen, causing the breakup.

Of course such frozen patterns are not stable against oxygen at elevated temperatures; in case of the $O_2 + H_2$ reaction they can even be considered to be a surface variable, as demonstrated by this study. A way to stabilize such patterns is addition of nickel as a further element, i.e. in presence of nickel the stripes do not fragmentize anymore under oxygen excess. Nickel could be added *in situ*, in form of a gas mixture of CO containing some $Ni(CO)_4$.

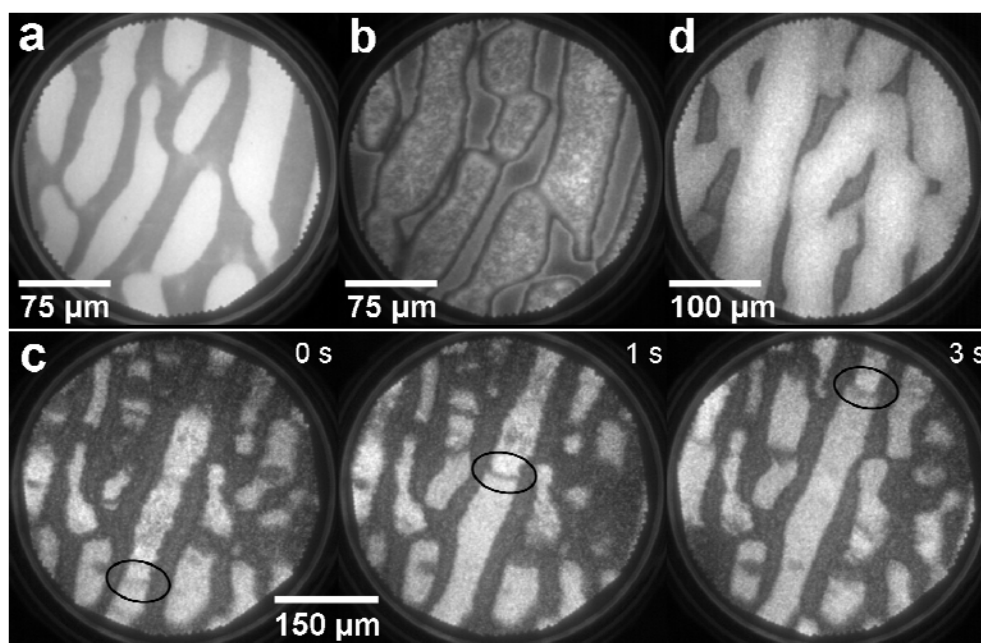Figure 3.28: (a) PEEM image of a stripe pattern formed at 500°C, $p(O_2) = 5 \cdot 10^{-6}$ mbar, $p(H_2) \approx 2 \cdot 10^{-6}$ mbar, $\Theta_V = 0.2$ MLE. (b) Same area after treatment with $1 \cdot 10^{-6}$ mbar O_2 and $5 \cdot 10^{-4}$ mbar CO/Ni(CO)$_4$ at 500°C. (c) Image sequence illustrating how a pulse (encircled) travels trough a channel, confined by VO_x stripes acting as walls; T = 500°C, $p(O_2) = 5 \cdot 10^{-5}$ mbar, $p(H_2) = 6 \cdot 10^{-5}$ mbar. (d) Eroded stripe pattern after ~25 hours of such reaction experiments (different area).

Figure 3.28 (a) shows a regular VO_x stripe pattern under reaction conditions. In (b) the same area is displayed after treating the sample at high pressures with a mixture of O_2 and CO, containing some $Ni(CO)_4$. Proof for the presence of nickel on the surface after that kind of treatment is given by XPS in chapter 4. As mentioned above, nickel deposition stabilizes the oxide structures, but furthermore, the properties of the brighter areas in between are changed: they become excitable in the presence of the $H_2 + O_2$ reaction. The rough appearance of those regions (see figure 3.28 (b)) is probably due to nickel oxide particles. One also notices that the phase boundaries are affected, which now appear as dark, broad lines.

The oxide stripes separate the area into independent catalyst areas, which could be termed micro-reactors. This can be demonstrated, as the system is excitable and produces pulses. Figure 3.28 (c) shows how a pulse travels through the central channel, crossing the field of view. This can be considered as 1-dimensional pulse propagation in a confined geometry. Such a phenomenon was studied before utilizing photolithography; the NO + CO reaction on Pt(100) was spatially confined by TiO_2 microstructures of several hundred Å thickness [37]. However, the lithographically prepared surface is supposedly more stable than the VO_x-structures, which are only a few Å high. Figure 3.28 (d) shows the surface after ~25 hours of reaction experiments, usually at 500°C and up to 10^{-4} mbar: the structures are slowly eroded by the reaction.

One can generate more complex patterns comprising several length scales by applying different reaction conditions successively. As an example figure 3.29 (a) and (b) display the modification of a regular VO_x stripe pattern by first stopping the reaction, followed by returning to reaction conditions at the 5-fold pressure; a shorter length scale is introduced by this procedure, causing the stripes to appear as if split in two.

A possibility to generate coarse, less regular patterns is to heat up the sample with a regular stripe pattern under reaction conditions. The PEEM image in figure 3.29 (c) shows such a pattern at 640°C and ~10^{-5} mbar. Even higher temperatures are possible: the phase separation is stable until at least 750°C at 10^{-4} mbar. Also at higher temperatures a finer structure can be added as described above; stopping the hydrogen supply and returning to reaction conditions at 10^{-4} mbar and 640°C yields the structure shown in (d). For the holes generated in the large oxide domains small vanadium oxide islands on the previously uncovered area are generated.
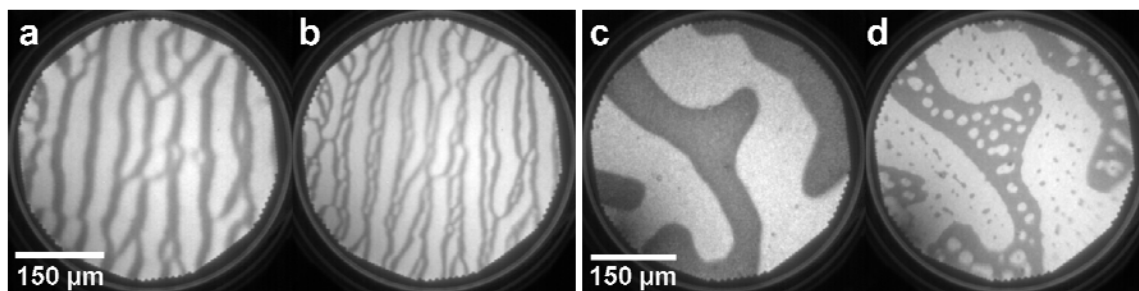
Figure 3.29: (a) PEEM image of a stripe pattern formed at 500°C, $p(O_2) = 2 \cdot 10^{-6}$ mbar, $p(H_2) \approx 1 \cdot 10^{-6}$ mbar, $\Theta_V = 0.2$ MLE. By interrupting the hydrogen supply and returning to reaction conditions at 5-fold pressure, (b) is produced. (c) The pattern was formed at 500°C, $p(O_2) = 1 \cdot 10^{-5}$ mbar, $p(H_2) = 4 \cdot 10^{-6}$ mbar and $\Theta_V = 0.2$ MLE and modified by heating up to 640°C; interrupting the hydrogen supply and returning to reaction conditions at the 10-fold pressure produces (d).
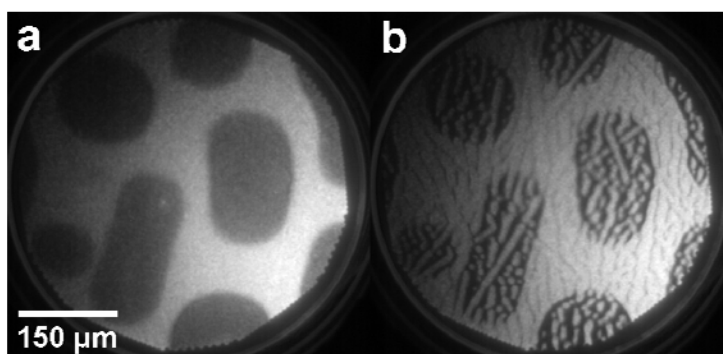
Figure 3.30: PEEM images illustrating pattern formation by oxygen alone and in combination with hydrogen; the surface was pretreated with 10^{-4} mbar O_2 for 90 min at 600°C. (a) Large VO_x islands (dark) appear while increasing hydrogen at 500°C, $p(O_2) = 8 \cdot 10^{-5}$ mbar, $p(H_2) = 2.8 \cdot 10^{-5}$ mbar, $\Theta_V = 0.2$ MLE. (b) Same area under the same conditions as (a), while decreasing hydrogen after peaking at $p(H_2) = 3 \cdot 10^{-5}$ mbar.

There is another possibility to organize the vanadium oxide distribution on Rh(111). It is mentioned in section 3.2 that a 3 min treatment at 750°C and $2 \cdot 10^{-7}$ mbar O_2 homogenizes the surface on the length scale of PEEM, which was regularly utilized to obtain an oxide distribution used as a reference state; the higher resolving power of LEEM reveals that the oxide decorates the step bunches. In contrast to that, oxygen treatments at higher pressures ($> 10^{-5}$ mbar) have the opposite effect. The oxide condenses into large islands of approximately circular or elliptic shape, as shown in figure 3.30. (a) displays a surface after exposition to 10^{-4} mbar oxygen for 90 min at 600°C, and subsequent cooling to 500°C. Since the oxygen-covered surface exhibits almost no PEEM intensity, addition of hydrogen is required to reveal the island

structure. Upon ramping up $p(H_2)$, reactive pattern formation occurs in addition, yielding the structure displayed in figure 3.30 (b); apparently there is still some VO_x between the large islands. An additional type of microstructures is accessible this way.

3.9 Higher coverages

It is already shown in section 3.3 that a ~3 MLE VO_x film exhibits very low catalytic activity. In PEEM such a surface appears just homogeneously dark and does not respond to high partial pressures (~10^{-4} mbar) of hydrogen or oxygen at 500°C. The same behavior is already observed at $\Theta_V = 1.3$ MLE.

An experiment at $\Theta_V = 0.3$ MLE is already presented in figure 3.7, exhibiting a similar phenomenology as at the usual coverage (0.2 MLE). The main difference is the formation of a more cellular pattern instead of stripes.

At $\Theta_V = 0.45$ MLE a different behavior was observed in PEEM upon cycling $p(H_2)$ at constant O_2 pressure. Increasing the hydrogen partial pressure yielded a homogeneous PEEM image; a pattern became visible while decreasing hydrogen again. The result at 500°C in the 10^{-4} mbar range is displayed in figure 3.31. The bright dots are presumably Rh(111) holes in the VO_x film. The formation of holes in a high coverage overlayer under reaction conditions is again similar to Rh(110)/Au [28].
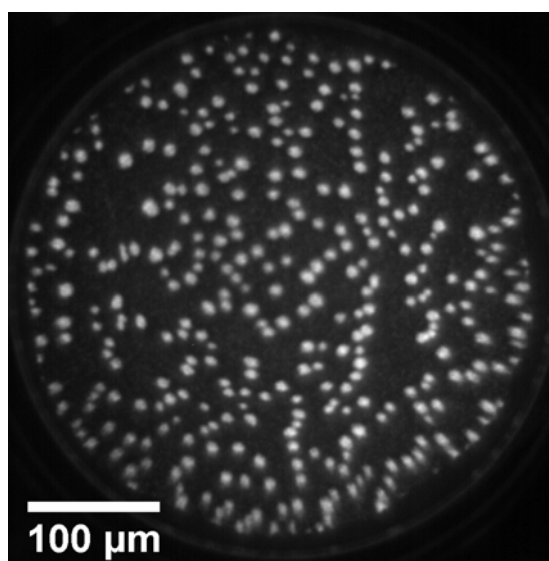

Figure 3.31: PEEM image of a dot pattern at 500°C, $\Theta_V = 0.45$ MLE, $p(O_2) = 1 \cdot 10^{-4}$ mbar, $p(H_2) = 5 \cdot 10^{-5}$ mbar; pattern formation was initiated by decreasing hydrogen from $9 \cdot 10^{-5}$ mbar.

At $\Theta_V = 0.6$ MLE no stationary patterns, but reaction fronts were observed. Starting with an oxygen-covered surface (dark in PEEM) at 500°C and $p(O_2) = 5 \cdot 10^{-6}$ mbar, reduction fronts could be initiated by adding $1 \cdot 10^{-5}$ mbar hydrogen. Decreasing $p(H_2)$ to $7 \cdot 10^{-6}$ mbar, the fronts stayed clearly defined, propagating slowly and reducing the surface to a state appearing light grey in PEEM. Upon collision of two reduction fronts something peculiar happened: the collision area turned much brighter than the surrounding reduced surface. The formation of such a low work function (low-Φ) area is displayed in figure 3.32; it vanishes within ~1 min.

Almost exactly the same phenomenon was observed on Rh(111) without VO$_x$ [13], after treating the sample excessively with oxygen. The low-Φ areas were assigned to accumulations of sub-surface oxygen, referring to earlier studies on Pt(100) and Pt(110) [38, 39]. It was argued that oxygen incorporation beneath the first atomic layer should reverse the surface dipole compared to oxygen adsorption, and thus have the opposite effect on the work function, reducing it. Since the present observation is extremely similar, that explanation is also considered for Rh(111)/VO$_x$; it might very well be that the presence of higher vanadium oxide coverages favors the penetration of the surface by oxygen atoms.
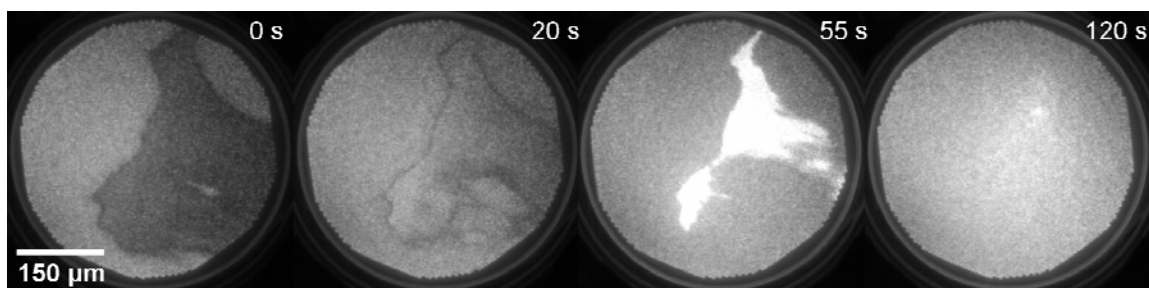

Figure 3.32: Series of PEEM images illustrating the formation and disappearance of a low-Φ area at 500°C, $\Theta_V = 0.6$ MLE, $p(O_2) = 5 \cdot 10^{-6}$ mbar, $p(H_2) = 7 \cdot 10^{-6}$ mbar. The fronts were initiated at $p(H_2) = 1 \cdot 10^{-5}$ mbar.

On the other hand there are serious concerns that the assignment of the low-Φ areas to sub-surface oxygen [19, 38, 39] is not correct and that the phenomena are instead caused by alkali metal contamination [40]. In the case of Rh(111) [19] and the present study it is not plausible why the sub-surface species should only be observed in collision areas of reduction fronts, but not generally in regions freed of O_{ad}. In the case of Pt(100) [38] it was reported that low-Φ areas do not form on a freshly sputtered (cleaned) surface, but just if such a surface is annealed at high temperature; that

observation strongly points towards contamination during heating, e.g. by surface segregation.

Explaining the observed phenomena (figure 3.32 and [19]) by alkali metal contamination is straight forward. It is known that the presence of alkali metals drastically reduces the work function of noble metal surfaces, and that they are transported with reduction fronts in the bistable $H_2 + O_2$ reaction, at least for the case of potassium on Rh(110) [41]. Due to its chemical attraction to oxygen, potassium becomes enriched in the steadily decreasing O-covered regions, forming low-Φ areas. Those disappear quickly in the case of Rh(111) [19] and Rh(111)/VO$_x$, supposedly as the co-adsorbed oxygen is consumed by the reaction; the driving force for alkali metal enrichment no longer exists.

Alkali metal contamination is considered to be the most likely explanation for the low-Φ areas (see figure 3.31 (b)). Although no alkali metals could be detected by Auger spectroscopy, the contamination hypothesis is not ruled out: lithium and potassium are almost impossible to detect on rhodium, due to Auger peak overlap. In any case, the alkali hypothesis as explanation for the formation of low-Φ areas has to be verified by experiment.

3.10 Summary

The study presented above shows how the inverted model catalyst system Rh(111)/VO$_x$ responds dynamically to changing conditions when exposed to the $H_2 + O_2$ reaction at temperatures above 500°C. The central finding is that a spatially homogeneous vanadium distribution at sub-monolayer coverages (< 0.5 MLE) is unstable. Under an oxygen atmosphere the oxide exists in form of nanoscale islands, which condense into mesoscopic patterns in presence of the reaction (see sections 3.2, 3.5).

Establishing reaction conditions by slowly adding hydrogen to an oxygen atmosphere initiates sudden state transitions in the system. First the oxygen adsorbed on rhodium is removed. Reduction of the initial V^{5+}-oxide follows, to an overlayer exhibiting a *split*-(2×2) structure. Further hydrogen increase causes a transformation into a regular (2×2)-oxide structure, which is predominantly composed of V^{3+}. This previously unobserved structure is presumably an analogon of the honeycomb-lattice

(2×2)-V_2O_3 overlayer known from Pd(111) and Rh(15 15 13) [8, 11, 21]. The (2×2)-V_2O_3 phase is probably stabilized by vacancies, and contains higher oxidized V bound to step bunches. The *split*-(2×2) oxide is also reported for the first time; the diffraction pattern suggests a structure of antiphase (2×2)-domains [26]. Probably both novel (2×2)-oxides are related by an order/disorder transition of domain boundaries to randomly distributed vacancies. Both structures are apparently not stable in absence of a chemical reaction (see sections 3.2, 3.4, 3.5).

Under reaction conditions regions covered by reduced oxides coexist with almost bare Rh(111) regions, forming mesoscopic patterns. With an oxygen-rich mixture of reactants an unusual pattern is observed, probably due to decoration effects (see figure 3.23). At higher hydrogen pressure stripe patterns with an intrinsic length scale are produced. The morphology of those patterns is governed by the conditions at the time of formation and changes with time. In addition, the microscopic morphology of the substrate plays a decisive role: since vanadium mass transport occurs predominantly on terraces, steps bunches represent diffusion barriers and align the VO_x stripes (see sections 3.4, 3.6, 3.7, 3.8).

A possible explanation for pattern formation is reactive phase separation (see section 1.4). The concept describes the phenomenon that nonequilibrium conditions, provided by a chemical reaction, cause condensation of phase separating mixtures into stationary, periodic structures. Rh(111)/VO_x is clearly a phase separating mixture, due to the strong chemical interaction between V and O. This is demonstrated by the formation of nanoscale islands under a pure oxygen atmosphere. Under reaction conditions periodic structures are formed, though a true stationary state could not be established, possibly due to long transients, i.e. too slow kinetics. Rh(111)/VO_x exhibits striking similarities to Rh(110)/Au/Pd [28], which is classified as a reactive phase separating system. In both cases the $H_2 + O_2$ reaction causes a material of significantly lower activity to be redistributed on a rhodium surface; periodic stripe patterns are formed and coarsen with time. Moreover, a power-law dependence between pressure and characteristic length scale was found for both systems (see sections 3.1, 3.5, 3.7).

On the other hand, a massive influence of phase boundary energies is evident. Apparently the presence of O_{ad} on the oxide-free rhodium surface favors nanoscale VO_x islands, which condense into mesoscopic islands (stripes) when O_{ad} is removed by the reaction. The driving force seems to be a drastic reduction of the total length of the phase boundary lines; this fragmentation/defragmentation transition might be regarded as a

2-dimensional analogon of a wetting/dewetting process, with O_{ad} on Rh(111) playing the role of a surfactant. The coarsening of the patterns observed under constant reaction conditions can be attributed to the reduction of the phase boundary length as well. If the phase boundary energy turns out to be the decisive influence, the true stationary state should be one large, circular oxide island (see sections 3.5, 3.7).
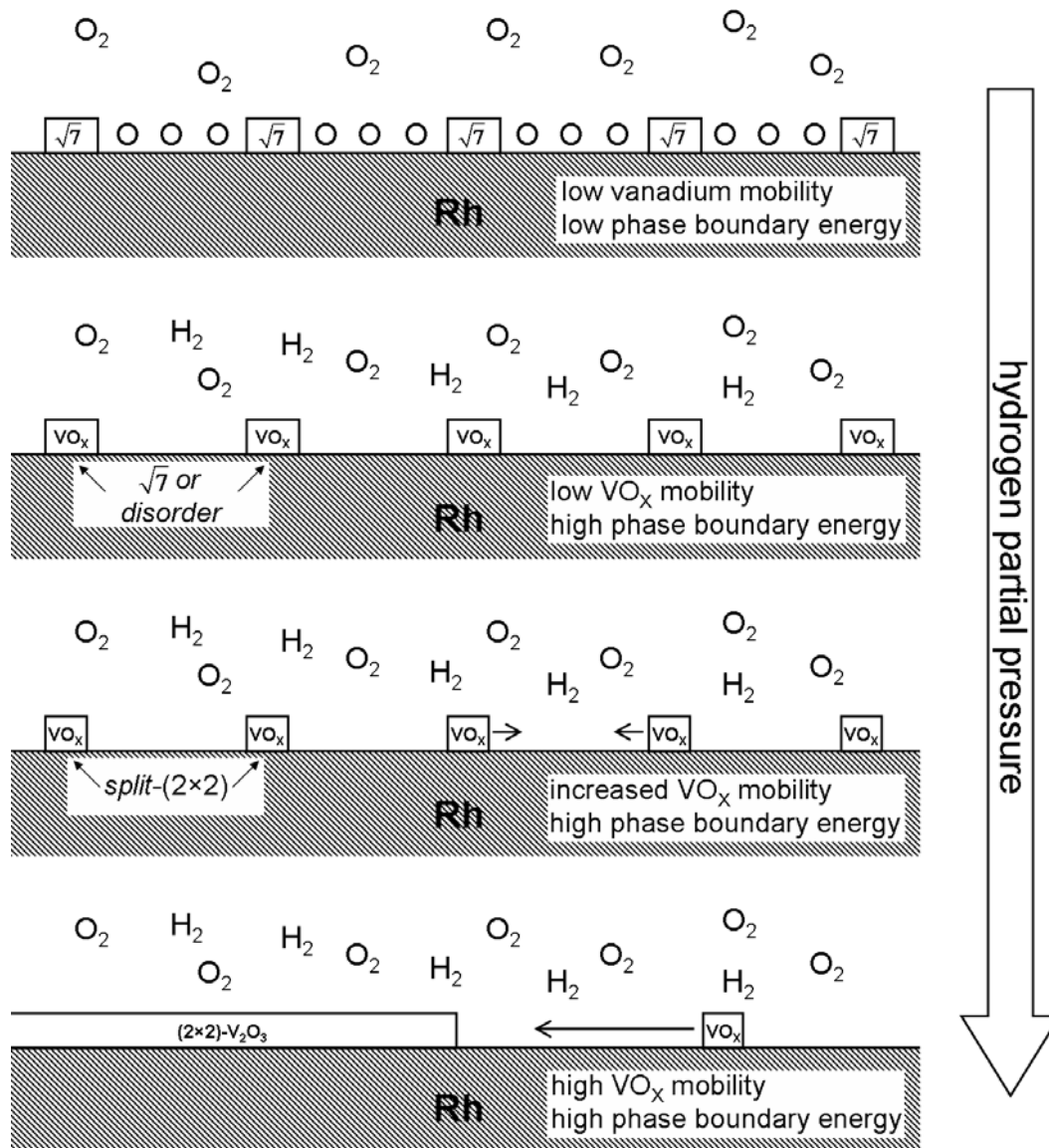

Figure 3.33: Schematic representation of the current hypothesis on the mechanism of stripe pattern formation while increasing the hydrogen partial pressure at a constant oxygen level. Short and long arrows represent low and high lateral mobility, respectively.

The current hypothesis on the morphogenesis of stripe patterns is summarized in figure 3.33. Starting in an oxygen atmosphere, the Rh(111) surface is covered with O_{ad} and VO_x nanoscale islands. Addition of hydrogen removes the oxygen adlayer and starts the reaction on Rh(111). The phase boundary energy is significantly increased, but no

condensation occurs due to low oxide mobility. Additional hydrogen reduces the VO_x, which causes the oxide-covered area to decrease; since the $H_2 + O_2$ reaction proceeds essentially on bare Rh(111), the reaction rate increases (see section 3.3). At high total pressures, favoring fast dynamics, VO_x can already condense into mesoscopic patterns (see figure 3.23), but further addition of hydrogen is required to obtain regular stripe patterns. Apparently only the (2×2)-oxide, which is formed at high $p(H_2)$, is mobile enough to reorganize into mesoscopic structures with intrinsic wavelengths. This last step does not affect the activity of the composite catalyst.

The periodic VO_x patterns subsequently coarsen under reaction conditions, obeying a power-law dependence of the average domain size on time. This behavior closely resembles the demixing of a liquid mixture quenched into a miscibility gap via spinodal decomposition [29, 30]. For the coarsening of Rh(111)/VO_x under reaction conditions a scaling exponent of roughly ¼ is found, indicating an island coalescence mechanism [31]. This mechanism can be observed directly with PEEM. Regarding the phenomenon as a 2-dimensional spinodal decomposition, the question remains open whether the influence of the reaction is strong enough to freeze the decomposition to a fixed wavelength, as observed for Rh(110)/Au + Pd [28, 34]. In that case Rh(111)/VO_x would belong to the class of reactive phase separating systems [28, 34, 35, 36]. If, on the other hand, the influence of phase boundary energies prevails on long time scales, an ordinary macroscopic phase separation results. A third possibility is that long-term effects, like contamination or surface roughening under reaction conditions, prevent the formation of a true stationary state, which might be found in an ideal system (see section 3.7).

To sum up, a vast influence of a chemical reaction on an inverted model catalyst system has been demonstrated. The morphology of the system is affected so strongly that application of selected reaction conditions can in principle be used as a microstructuring technique for catalytic surfaces (see section 3.8).

3.11 References

[1]   J. Schoiswohl, M. Sock, S. Eck, S. Surnev, M. G. Ramsey, F. P. Netzer, G. Kresse, *Atomic-level growth study of vanadium oxide nanostructures on Rh(111)*, Phys. Rev. B 69 (2004), 155403.

[2]   J. Schoiswohl, S. Surnev, F. P. Netzer, G. Kresse, *Vanadium oxide nanostructures: from zero- to three-dimensional*, J. Phys. Condens. Matt. 18 (2006), R1.

[3]   J. Schoiswohl, S. Surnev, M. Sock, S. Eck, M. G. Ramsey, F. P. Netzer, G. Kresse, *Reduction of vanadium-oxide monolayer structures*, Phys. Rev. B 71 (2005), 165437.

[4]   J. Schoiswohl, S. Surnev, M. Sock, M. G. Ramsey, G. Kresse, F. P. Netzer, *Thermodynamisch kontrollierte Selbstorganisation von zweidimensionalen Oxid-Nanostrukturen*, Angew. Chem. 116 (2004), 5663;
        Thermodynamically controlled self-assembly of two-dimensional oxide nanostructures, Angew. Chem. Int. Ed. 43 (2004), 5564.

[5]   G. Krenn, J. Schoiswohl, S. Surnev, F. P. Netzer, R. Schennach, *Metal-oxide boundary effects in vanadium oxide – Rh(111) inverse model catalysts: a RAIRS, STM and TPD study*, Top. Catal. 46 (2007), 231.

[6]   J. Schoiswohl, M. Sock, Q. Chen, G. Thornton, G. Kresse, M. G. Ramsey, S. Surnev, F. P. Netzer, *Metal supported oxide nanostructures: model systems for advanced catalysis*, Top. Catal. 46 (2007), 137.

[7]   J. Schoiswohl, G. Kresse, S. Surnev, M. Sock, M. G. Ramsey, F. P. Netzer, *Planar Vanadium Oxide Clusters: Two-Dimensional Evaporation and Diffusion on Rh(111)*, Phys. Rev. Lett. 92 (2004), 206103.

[8]   J. Schoiswohl, S. Surnev, F. P. Netzer, *Vanadium Oxide Overlayers on Vicinal Rh(15 15 13): The Influence of Surface Steps*, J. Phys. Chem. C 111 (2007), 10503.

[9]   D. G. Castner, G. A. Somorjai, *LEED, AES and Thermal Desorption Studies of the Oxidation of the Rhodium(111) Surface*, Applic. Surf. Sci. 6 (1980), 29.

[10]   J. Wintterlin, M.-L. Bocquet, *Graphene on metal surfaces*, Surf. Sci. 603 (2009), 1841.

[11]   S. Surnev, G. Kresse, M. Sock, M. G. Ramsey, F. P. Netzer, *Surface structures of ultrathin vanadium oxide films on Pd(111)*, Surf. Sci. 495 (2001), 91.

[12]   S. Penner, B. Jenewein, D. Wang, R. Schlögl, K. Hayek, *Rh-V alloy formation in Rh-VOx thin films after high-temperature reduction studied by electron microscopy*, Phys. Chem. Chem. Phys. 8 (2006), 1223.

[13]   A. Schaak, R. Imbihl, *Bistability and formation of low work function areas in the $O_2 + H_2$ reaction on a Rh(111) surface*, J. Chem. Phys. 113 (2001), 9822.

[14]   J. Schoiswohl, S. Surnev, F. P. Netzer, *Reactions on inverse model catalyst surfaces: atomic views by STM*, Top. Catal. 36 (2005), 91.

[15]   K. Mori, M. Miura, A. Miyamoto, Y. Murakami, *Catalytic Reactions on Well-Characterized Vanadium Oxide Catalysts. 3. Oxidation of Hydrogen*, J. Phys. Chem. 88 (1984), 5232.

[16]   M. J. Kratzer, J. Stettner, A. Winkler, *Water Formation on Clean and Vanadium Oxide Covered Pd(111) by Permeating Deuterium*, J. Phys. Chem. C 111 (2007), 12723.

[17] S. Surnev, M. G. Ramsey, F. P. Netzer, *Vanadium oxide surface studies*, Prog. Surf. Sci. 73 (2003), 117.

[18] S. Guimond, J. M. Sturm, D. Göbke, Y. Romanyshyn, M. Naschitzki, H. Kuhlenbeck, H.-J. Freund, *Well-Ordered V₂O₅(001) Thin Films on Au(111): Growth and Thermal Stability*, J. Phys. Chem. C 112 (2008), 11835.

[19] G. A. Sawatzky, D. Post, *X-ray photoelectron and Auger spectroscopy study of some vanadium oxides*, Phys. Rev. B 20 (1979), 1546.

[20] G. Krenn, R. Schennach, *Adsorption and reaction of methanol on clean and oxygen modified rhodium/vanadium surface alloys*, J. Chem. Phys. 120 (2003), 5729.

[21] S. Surnev, G. Kresse, M. G. Ramsey, F. P. Netzer, *Novel Interface-Mediated Metastable Oxide Phases: Vanadium Oxides on Pd(111)*, Phys. Rev. Lett. 87 (2001), 086102.

[22] J. Gustafson, A. Resta, A. Mikkelsen, R. Westerström, J. N. Andersen, E. Lundgren, J. Weissenrieder, M. Schmid, P. Varga, N. Kasper, X. Torrelles, S. Ferrer, F. Mittendorfer, G. Kresse, *Oxygen-induced step bunching and faceting of Rh(553): Experiment and ab initio calculations*, Phys. Rev. B 74 (2006), 035401.

[23] J. J. Yeh, I. Lindau, *Atomic Subshell Photoionization Cross Sections and Asymmetry Parameters: 1 ≤ Z ≤ 103*, At. Data Nucl. Data Tables 32 (1985), 1.

[24] S. Surnev, J. Schoiswohl, G. Kresse, M. G. Ramsey, F. P. Netzer, *Reversible Dynamic Behavior in Catalyst Systems: Oscillations of Structure and Morphology*, Phys. Rev. Lett. 89 (2002), 246101.

[25] R. E. Johnson, *Conflicts between Gibbsian Thermodynamics and Recent Treatments of Interfacial Energies in Solid-Liquid-Vapor Systems*, J. Phys. Chem. 63 (1959), 1655.

[26] J. P. Biberian, M. A. van Hove, *A new Model for CO Ordering at High Coverages on Low Index Metal Surfaces: a Correlation between LEED, HREELS and IRS*, Surf. Sci. 138 (1984), 361.

[27] P. A. Thiel, E. D. Williams, J. T. Yates, W. H. Weinberg, *The Chemisorption of CO on Rh(111)*, Surf. Sci. 84 (1979), 54.

[28] A. Locatelli, T. O. Mentes, L. Aballe, A. Mikhailov, M. Kiskinova, *Formation of Regular Surface-Supported Mesostructures with Periodicity Controlled by Chemical Reaction Rate*, J. Phys. Chem. B 110 (2006), 19109.

[29] C. H. P. Lupis, *Chemical Thermodynamics of Materials*, Prentice Hall, Inc., New York 1983.

[30] S. C. Glotzer, E. A. Di Marzio, M. Muthukumar, *Reaction-Controlled Morphology of Phase-Separating Mixtures*, Phys. Rev. Lett. 74 (1995), 2034.

[31] A. Lo, R. T. Skodje, *Kinetic and Monte Carlo models of thin film coarsening: Cross over from diffusion-coalescence to Ostwald growth modes*, J. Chem. Phys. 112 (2000), 1966.

[32] S. V. Khare, N. C. Bartelt, T. L. Einstein, *Diffusion of Monolayer Adatom and Vacancy Clusters: Langevin Analysis and Monte Carlo Simulations of their Brownian Motion*, Phys. Rev. Lett. 75 (1995), 2148.

[33] H.-J. Ernst, F. Fabre, J. Lapujoulade, *Observation of Dynamical Scaling in "Spinodal Decomposition" in Two Dimensions*, Phys. Rev. Lett. 69 (1992), 458.

[34]   A. Locatelli, C. Sbraccia, S. Heun, S. Baroni, M. Kiskinova, *Energetically Driven Reorganization of a Modified Catalytic Surface under Reaction Conditions*, J. Am. Chem. Soc. 127 (2005), 2315.

[35]   Y. De Decker, H. Marbach, M. Hinz, S. Günther, M. Kiskinova, A. S. Mikhailov, R. Imbihl, *Promoter-Induced Reactive Phase Separation in Surface Reactions*, Phys. Rev. Lett. 92 (2004), 198305.

[36]   Y. De Decker, A. S. Mikhailov, *Promoter-Induced Nonlinear Pattern Formation in Surface Chemical Reactions*, J. Phys. Chem. B 108 (2004), 14759.

[37]   N. Hartmann, Y. Kevrekidis, R. Imbihl, *Pattern formation in restricted geometries: The NO+CO reaction on Pt(100)*, J. Chem. Phys. 112 (2000), 6795.

[38]   H. H. Rotermund, J. Lauterbach, G. Haas, *The Formation of Subsurface Oxygen on Pt(100)*, Appl. Phys. A 57 (1993), 507.

[39]   A. von Oertzen, A. Mikhailov, H.-H. Rotermund, G. Ertl, *Subsurface oxygen formation on the Pt(110) surface: experiment and mathematical modelling*, Surf. Sci. 350 (1996), 259.

[40]   R. Imbihl, private communication.

[41]   H. Marbach, S. Günther, B. Luerßen, L. Gregoratti, M. Kiskinova, R. Imbihl, *Selforganization of alkali metal on a catalytic metal surface*, Catal. Lett. 83 (2002), 161.

4. Nickel and nickel oxide on Rh(111)

The addition of nickel to Rh(111) facilitates spatiotemporal pattern formation in the originally bistable system Rh(111)/$H_2 + O_2$ (see sections 1.2, 1.3). The first observations were made with co-deposited vanadium oxide and nickel as contaminant (see figure 3.28), but it soon became clear that the effect is caused by the presence of nickel alone. Under reaction conditions the surface is composed of a bimetallic surface alloy with oxide particles on top, i.e. Rh(111)/Ni/NiO. The first results on this interesting novel reaction-diffusion system are presented and discussed in this chapter.

4.1. Basic observations

Nickel was deposited from the gas phase as $Ni(CO)_4$. The CO supply of the UHV chamber contained a minor fraction of this substance, probably formed by reaction with the stainless steel walls. Chemical vapor deposition was performed exposing the clean sample at 500°C to pressures in the 10^{-4} mbar range for several minutes, in presence of 10^{-6} mbar O_2.

This way of metal deposition is highly convenient, but bears a major disadvantage. The high surface temperature does not only dissociate the carbonyl molecules, but also leads to instant alloying [1]. The resulting surface alloy exhibits a varying stoichiometry normal to the surface; the nickel distribution is unknown. Under these circumstances it is not possible to determine the exact amount of deposited nickel by electron spectroscopic methods, and the precipitation of 3-dimensional nickel oxide particles further complicates the situation. Just a rough estimate of the Ni coverage is given in section 4.2.

Most experiments were started in an oxygen atmosphere; after adjusting the temperature to the desired value the hydrogen partial pressure was increased to enter the excitable regime. A variety of spatiotemporal patterns could be observed, then. Figure 4.1 gives some examples, recorded at 400°C: a target pattern, a spiral wave and a pulse train were observed under the same conditions on different regions on the surface. In addition to the spatiotemporal patterns, stationary structures were present, appearing as

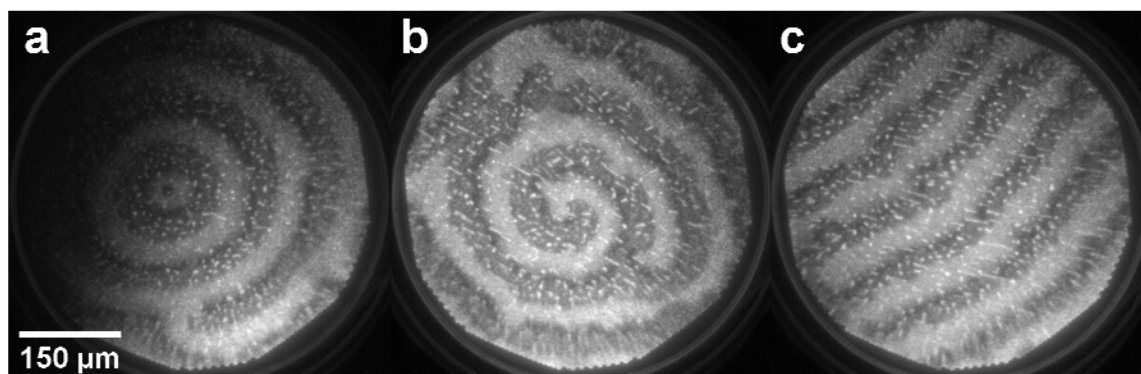bright dots or elongated bars. Those are shown to be nickel oxide particles in the next section.

Figure 4.1: Spatiotemporal pattern formation on Rh(111)/Ni/NiO at 400°C, $p(O_2) = 2 \cdot 10^{-4}$ mbar, $p(H_2) \approx 2 \cdot 10^{-4}$ mbar in PEEM. In different regions of the sample target patterns (a), rotating spiral waves (b) or pulse trains (c) were observed. The waves propagate outwards (a, b), or in the case of (c) from top, left to bottom, right. The bright spots of a few μm size are stationary and consist of nickel oxide.

The chemical waves propagated at a speed of ~40 μm/s, bypassing the oxide particles (details in section 4.3, figure 4.13). The rotation period of the spiral (2.4 s) was almost the same as the trigger period of the target pattern, 2.3 s (see figure 4.1 (b, a)). This is supposedly a random coincidence, since for excitable media such frequencies usually depend on the properties of the pacemaker, i.e. the triggering defect (see section 1.3 and [2]). The pulses in figure 4.1 (c) bypassed a selected spot with a period of 2.1 s, and in another region a target was observed emitting waves every 2.7 s (not shown). This deviation suggests excitable rather than oscillatory behavior, the latter being characterized by constant eigenfrequencies (see section 1.3).
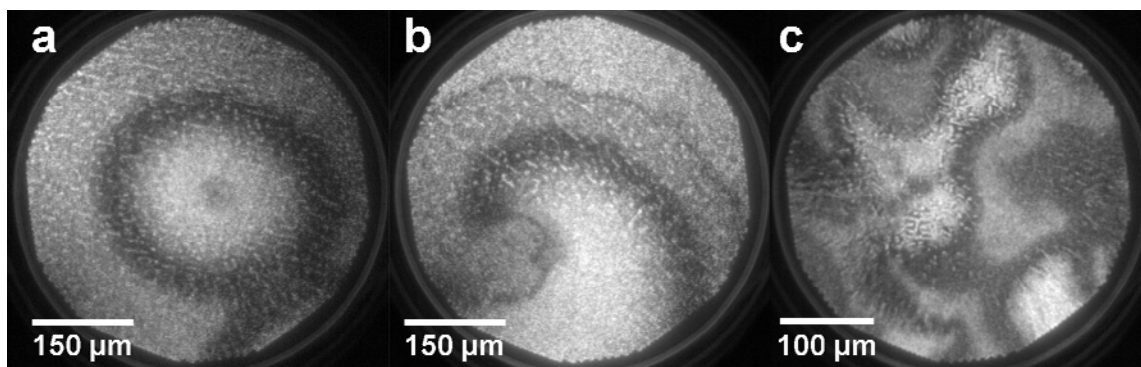
Figure 4.2: PEEM images of spatiotemporal pattern formation on Rh(111)/Ni/NiO at 500°C. (a) Target pattern at $p(O_2) = 5 \cdot 10^{-5}$ mbar, $p(H_2) = 2.8 \cdot 10^{-5}$ mbar. (b) Rotating spiral wave at $p(O_2) = 1 \cdot 10^{-4}$ mbar, $p(H_2) = 1 \cdot 10^{-4}$ mbar. (c) Irregular pulses at $p(O_2) = 5 \cdot 10^{-5}$ mbar, $p(H_2) = 2.6 \cdot 10^{-5}$ mbar.

The PEEM images in figure 4.2 were recorded at 500°C. The basic phenomenology remained unchanged, as target patterns (a) and spiral waves (b) formed. Also irregularly shaped pulses were observed (c), directly after entering the excitable regime by quickly changing the hydrogen partial pressure. The main changes compared to 400°C were higher propagation velocities of about ~60 μm/s and longer triggering periods, 12.5 s for (a) and 4.2 s for (b). This resulted in much broader pulses, i.e. increased wavelengths. The structure of the pulses is revealed by figure 4.2 (b): the surface cycles trough four different states, characterized by different PEEM intensities. The bright surface changes into a dark grey state, which appears as a thin boundary line since it is transformed quickly to a medium grey state. The latter changes into a dark state which itself gives way to the initial bright surface. The whole cycle is plotted in figure 4.3 (a). The dark grey state (thin line) does not appear in figure 4.2 (a) because the field of view is too small to show the whole sequence; it is also not visible at 400°C in figure 4.1, probably remaining unresolved there due to a too small wavelength.
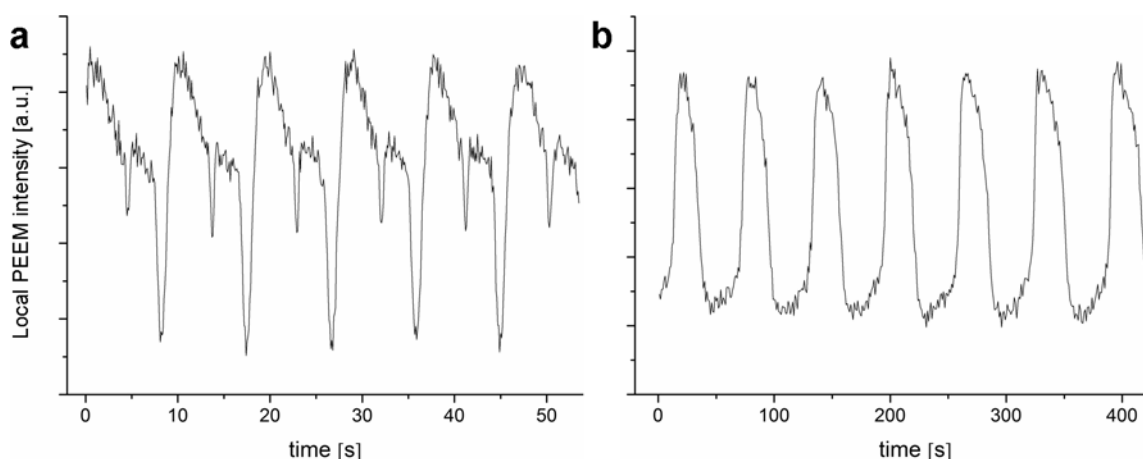
Figure 4.3: Time series of the PEEM intensity at 500°C and a fixed O_2:H_2 ratio of 1.5:1. The total pressure is $p = 8.2 \times 10^{-5}$ mbar (a) and $p = 1.7 \times 10^{-6}$ mbar (b), respectively. Both graphs represent scans of a small section (~1000 μm^2) of the field of view.

At significantly lower total pressure the structure of the pulses changes. Figure 4.3 (a) shows a PEEM brightness trace representing the temporal structure of a typical pulse train at ~10^{-4} mbar and 500°C. As described above, the scanned surface area alternates between four brightness levels/states which are clearly defined in (a). At roughly 50 times lower total pressure the picture is drastically altered, as displayed in (b). The surface oscillates much slower, alternating between just two brightness levels via diffuse, front-like transitions. Those propagate at roughly ~60 μm/s and exhibit a

period of 62.5 s. A wavelength of 3.7 mm can be estimated, which is in the order of magnitude of the sample diameter (~10 mm). PEEM images of such transitions are included in figure 4.5.

The altered behavior at lower pressures could be interpreted as consequence of a different excitation mechanism with only two states, but another explanation is favored, suggested by comparison with the $CO + O_2$ reaction on Pt(110). That system exhibits a broad variety of spatiotemporal phenomena [2]. At high pressure ($p(O_2) = 4 \cdot 10^{-4}$ mbar), instead of true bistable behavior a phenomenon termed *double metastability* was found [2, 3, 4]: front-induced kinetic phase transitions between an active and a poisoned state occur, but both states become unstable after some time and are replaced by the other via a reaction front. This behavior was traced back to destabilization of the stationary states of a bistable system by surface imperfections. This phenomenon is probably also observed here at lower pressures, rather than a second excitation mechanism.

So chemical waves of macroscopic dimensions were observed at lower pressures; the surface periodically alternated between two states (see figure 4.3 (b)). Provided that the two states exhibit different reactivities, macroscopic rate oscillations are to be expected. Those were indeed found, as shown by QMS in figure 4.4. Oxygen and hydrogen oscillate in phase, and water, as the reaction product, in antiphase. Hence, the two states do exhibit different reactivities.
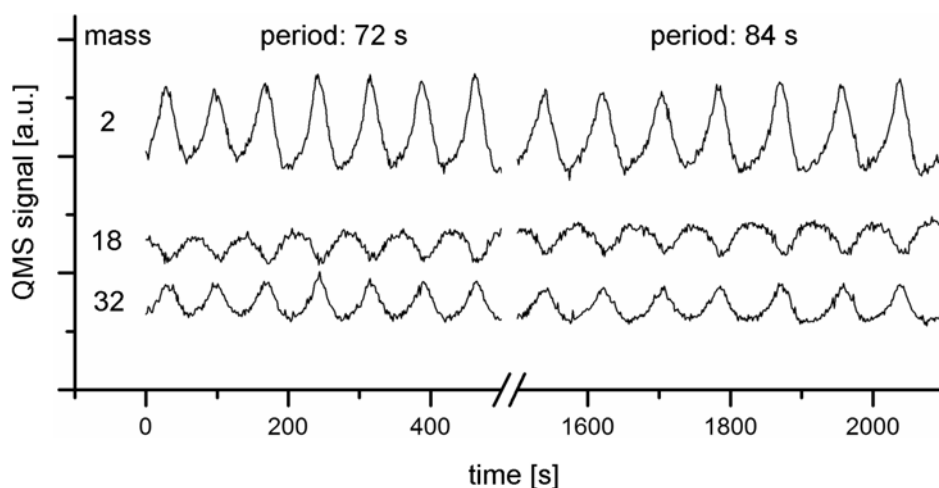

Figure 4.4: Rate oscillations at 500°C, $p(O_2) = 2 \cdot 10^{-6}$ mbar, $p(H_2) = 1 \cdot 10^{-6}$ mbar. The product trace (water, mass 18) oscillates in antiphase to the reactants. The oscillation period increases throughout the experiment. It might be recognized that the hydrogen trace appears at a higher level than oxygen, in contrast to the given values; that is due to different detection efficiency and mass-dependent differential pumping. The mass 2 signal was already scaled down for display reasons.

One further detail is visible in figure 4.4: the oscillation period significantly increased within the experiment at constant conditions. This was probably caused by a change of the pacemaker. One could alternatively think that the surface changed throughout the reaction, causing the period to elongate, but that explanation can be ruled out: not only increasing oscillation periods at constant conditions were observed as in figure 4.4, but also the opposite phenomenon, i.e. decreasing periods. The latter could be clearly associated with changing pacemakers in PEEM. In figure 4.5 a plot as in figure 4.3 is displayed, with oscillations changing their frequency at ~400 s. The PEEM images before and after this frequency change show diffuse fronts propagating in completely different directions (indicated), which therefore have to originate from different pacemakers. The latter could not be observed directly under these conditions. A possible explanation would be that the edges of the specimen (which cannot be observed in PEEM) can serve as pacemakers. However, figure 4.5 clearly points out the high significance of the pacemakers for the frequencies.
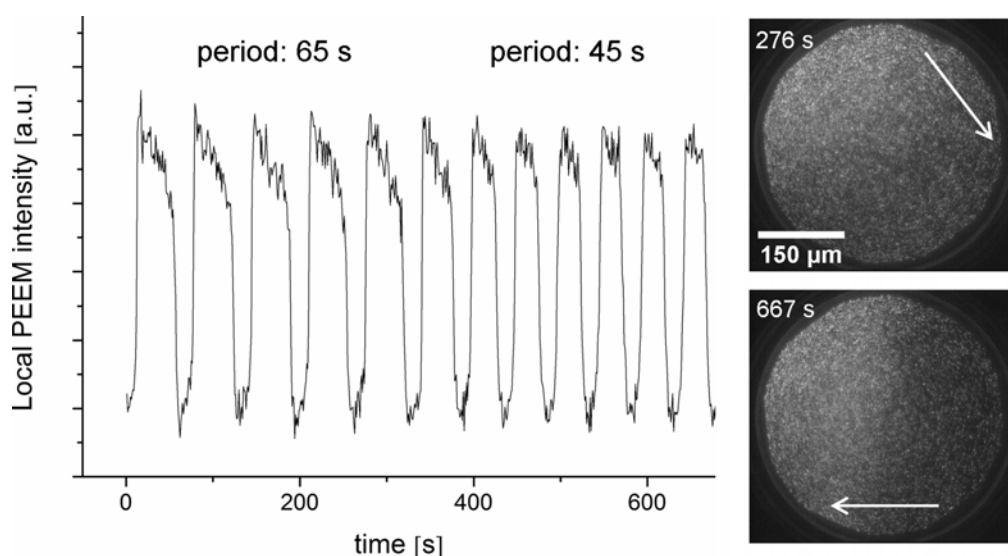

Figure 4.5: PEEM brightness trace illustrating a frequency change at 500°C, $2 \cdot 10^{-6}$ mbar O_2, $1 \cdot 10^{-6}$ mbar H_2. The change was caused by a changing pacemaker, as demonstrated by the PEEM images before and after; the propagation direction (arrows) was different. The granular structure of the images is due to noise, oxide particles are not visible here.

4.2 Catalyst composition

For surface chemical analysis and high resolution imaging a sample prepared with nickel was taken to the synchrotron source *Elettra*. The sample was cleaned by

hours of oxygen treatments, yielding a carbon-free surface which exhibited chemical wave propagation when exposed to the $H_2 + O_2$ reaction. After the beamtime it was recognized in PEEM that the probed surface showed indications of an alkali metal contamination. Formation of low-Φ areas was recognized in the collision area of pulses, similar to what is discussed in section 3.9 (figure 3.32). Furthermore, it was observed that dark pulses, traveling into a supposedly contaminated area, were transformed into bright ones [5]. This effect can be explained by an uptake of alkali metal into an oxygen-rich pulse, as it is known that potassium can be transported on Rh(110) in form of K + O pulses appearing bright in PEEM [6].

The presence of an electronic promoter like potassium would affect the quantitative aspects of wave propagation, but not change the system qualitatively. This can be stated from comparison with data for which no indication of a contamination exists, e.g. all data presented in the previous section. Therefore, only those data were discarded which would have probably been altered by the influence of an alkali metal.

Surface characterization with synchrotron radiation was performed *in situ* at about 10^{-6} mbar and 500°C, where macroscopic chemical waves (supposedly due to double metastability, see figure 4.3) were observed. Due to the limited field of view (up to 60 μm) in LEEM/MEM, reaction fronts were not visible, since those are diffuse and propagate quite fast (see figure 4.5). The waves appeared as temporal brightness oscillations. XPEEM images and μ-XP spectra were acquired integrating over several periods.

The LEEM image in figure 4.6 (a) shows a surface composed of two domains of different brightness. Those are identified with μ-XPS as being covered essentially by metallic (Me) and oxidic (Ox) nickel, respectively (b, c). The insets in (a) are images of the regions selected for μ-XPS, displayed on the same scale.

The spectra in figure 4.6 (b, c) reveal the metallic/oxidic state of the corresponding areas, as the binding energies of the main peaks are typical for metallic/oxidic nickel [7–11]. Further analysis is difficult, since the XP-spectra of nickel and its oxides exhibit satellites beyond 858 eV [7, 9–11] which were not recorded here. The satellite of metallic Ni is located at the very end of the available energy region (858.5 – 859.0 eV, not recognizable in figure 5.6 (b)), making it impossible to define an adequate background. Therefore a fit cannot yield reliable results and is not shown. In case of the oxide spectrum (c) the high energy satellites have a smaller impact, since

metallic nickel contributes just minor intensity (859 eV), and the satellites of NiO are further off (> 861 eV [7, 9–11]). The spectrum (c) can be fitted reasonably with three components, though the background is supposedly not very accurate. The fit results are therefore not reliable quantitatively, but at least number and binding energies of the components should be correct.
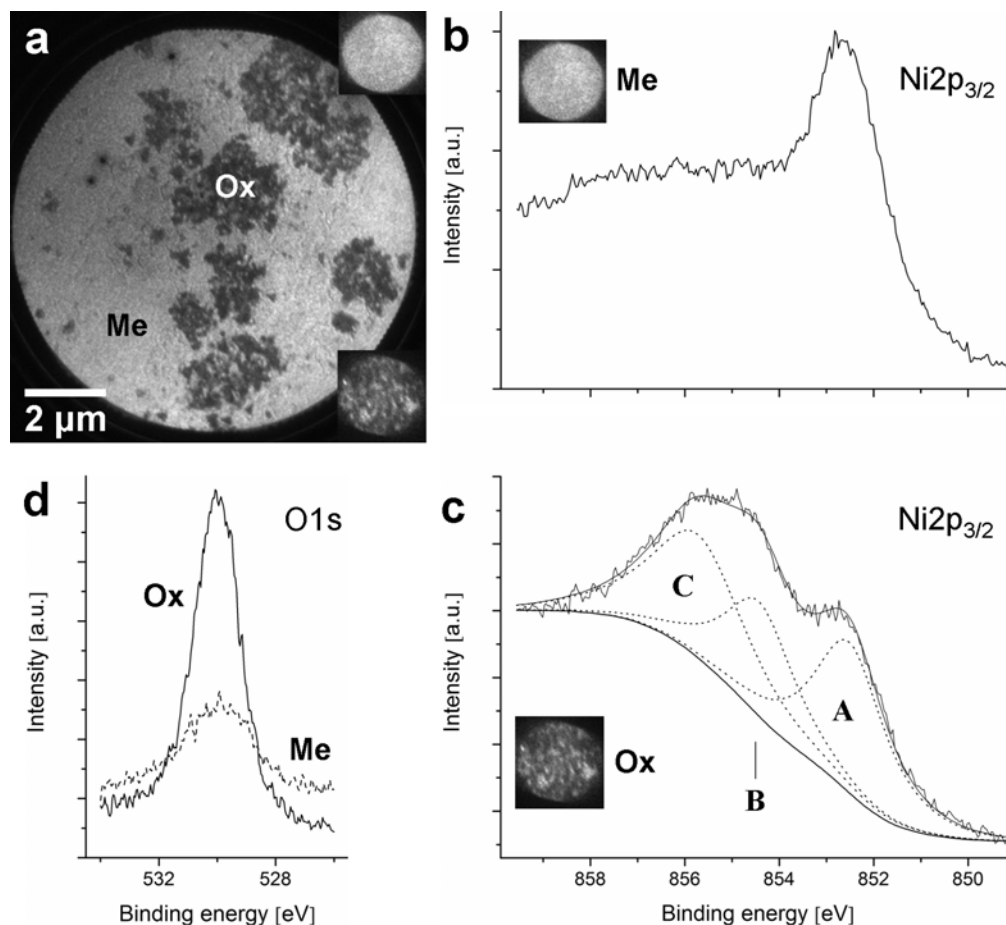

Figure 4.6: (a) LEEM image (19 eV) of the Rh(111)/Ni/NiO catalyst surface under reaction conditions at 502°C, ~1·10^{-6} mbar O$_2$, 7·10^{-7} mbar H$_2$. The dark parts of the surface are covered with oxide particles. The insets show the areas selected for μ-XPS. (b, c) Ni2p$_{3/2}$ photoemission spectra of the metallic/oxidic areas, recorded under the same conditions at 982 eV incident beam energy. The acquisition time was 128 s, which equals about three oscillation periods. The energy scale refers to the Rh3d$_{5/2}$ bulk line set to BE = 307.2 eV [8]. For details on the fitting procedure see text; the three Ni components are indicated as A, B and C. The Ni2p$_{3/2}$-region was not recorded completely; additional satellites should be present at higher binding energy. (d) O1s spectra recorded under the same conditions.

The metallic spectrum (b) is composed of a main peak at 852.5 eV and additional intensity on the high binding energy side. It is unclear whether the intensity above 854 eV arises from oxidized Ni components or from the satellite structure of metallic Ni alone [11]. Also the O1s spectrum (see figure 4.6 (d)) does not give an answer: the single

feature at 530.0 eV could either originate from NiO (529 – 530 eV [7, 9, 10]) or O_{ad} on rhodium (529.4 eV [12]).

Component A in figure 4.6 (c) is located at 852.5 eV, a typical binding energy for metallic nickel [7−11]. The value is in satisfactory agreement with the 852.2 eV found for nickel adsorption at the step edges of Rh(553) [13], considering that here a surface alloy is analyzed. The intensity originates supposedly from the bright (metallic) parts of the probed area (see inset in figure 4.6 (c)).

The oxidic part ($E_B > 853$ eV) of the spectrum in figure 4.6 (c) requires two components to be fitted. One is assumed to be NiO, which is chemically shifted versus metallic Ni by +1.9 eV according to [7, 14] (also lower values were reported [9, 10]). So component B is fixed to 854.4 eV and the width of A (FWHM = 1.78 eV), while those parameters are left open for C. The fit yields a broader (FWHM = 2.36 eV) peak C at $E_B = 855.7$ eV.

The latter component is well known from XPS on the nickel-oxygen system, but its origin is a subject of discussion since decades [7, 9–11, 14–18]. According to [7] the chemical shift of 3.2 eV (component C vs. the metallic peak) matches exactly the one found for hydratized Ni^{2+}-oxide, but this assignment can be ruled out because of the thermal stability of such compounds: $Ni(OH)_2$ already decomposes between 200 and 300°C [19], while component C is obviously stable at 500°C. Furthermore, a second O1s component should be present ($E_B \sim 532$ eV, [7, 11]), which is not the case (see figure 4.6 (d)); the single O1s peak at 530.0 eV is assigned to NiO [7, 9, 10, 14, 15, 18].

Assignment of component C to Ni_2O_3 [9, 10] can be ruled out for similar reasons. The anhydrous compound is unlikely to even exist [20] and much less to be stable at 500°C. Moreover, for hydrates an additional O1s compound is to be expected, but not observed.

Two possibilities for component C remain. Such peaks were often assigned to Ni^{3+} point defects in the surface region of NiO [14, 18]. Since it was claimed that in presence of such defects no corresponding additional oxygen compound is required [14, 18], component C could be assigned to Ni^{3+}; also an increase of Ni^{3+}-defects with temperature was reported [18], explaining the high intensity of component C compared to B (NiO). This assignment is probably wrong. It was suggested [9, 15] and demonstrated by cluster calculations [16, 17] that there are intrinsic intensity contributions of NiO at the relevant binding energies. A *nonlocal screening satellite* [16] was shown to exist, and additionally it was demonstrated that the ground state of

unsaturated Ni^{2+} ions at the surface shifts about 1 eV to higher binding energy [17]. The latter effect obviously produces high intensities at a high surface/volume ratio; interestingly this is also true for the *nonlocal screening satellite*, as demonstrated in [16]. Since the spectrum in figure 4.6 (c) stems from NiO nanoparticles (see below), a high surface/volume ratio is given, potentially explaining why the satellite component C is so strongly pronounced. The increased width of the feature probably arises from its two origins, which lead to slightly shifted intensities.

So the spectrum in figure 4.6 (c) can be explained by NiO nanoparticles on a rhodium substrate alone, corresponding to the dark regions in (a). The bright regions contain metallic Ni and possibly a small fraction of NiO. The latter would not be not too surprising: the dark oxide nanoparticles (see figure 4.8) exhibit a broad size distribution, and so it might very well be that particles which remain unresolved due to their small size, are present on the probed area.

As stated above, electron spectroscopy cannot be used to determine the precise amount of nickel, because in the present case the lateral distribution is inhomogeneous (NiO particles), and there is partial mixing normal to the surface (surface alloying). The NiO particles can be excluded by performing μ-XPS on the metallic area, but the vertical distribution of nickel in the substrate is unknown. Only a rough estimate can be given, using assumptions.

The Rh(111)/Ni surface can supposedly be described as an intermediate between a homogeneous alloy and an adsorption system. It was shown that above 600 K adsorbed nickel is rapidly lost to the bulk of Rh(111) on a timescale of minutes, forming an alloy [1]. Here, on the other hand, excitable behavior is still observed after 50 and more hours of reaction experiments at even higher temperatures, indicating that significant amounts of Ni remain at the surface. Evidently, the alloying process is substantially slowed down under reaction conditions; presumably the presence of oxygen traps nickel at the surface, fixing the nickel content. Two limit cases are considered: firstly, nickel is assumed to be homogeneously distributed within the detection depth (~10 atomic layers), and then it is treated as an adsorbate, i.e. all Ni atoms are assumed to be present on top of the surface.

Figure 4.7 shows the relative photoemission intensity from $Ni2p_{3/2}$ and Rh3d core levels; the data is already corrected for the energy dependence of the spectrometer transmission. The ratio of detected photoelectrons (integrals) is ~8:1, but still some

corrections have to be applied. It is mentioned above that the Ni2p$_{3/2}$ region was not recorded completely, which also affects the background subtraction; both influences add up to an underestimation of approximately (15 ± 10) %. This amount is therefore added to the Ni2p$_{3/2}$ integral for compensation. Further 50 % have to be added to the result, in order to take into account the Ni2p$_{1/2}$ level (degeneracy $= (2j+1)$), which gives a relative photoelectron emission flux of ~5:1 (4.8 ± 0.5) $(I_{Rh3d}:I_{Ni2p})$.
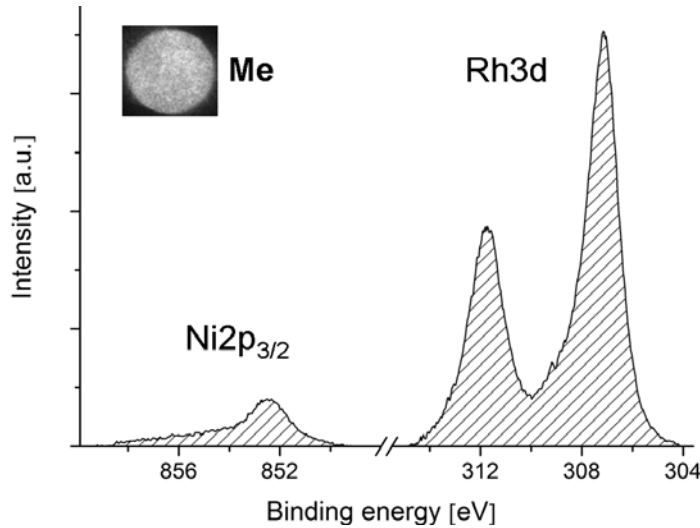
Figure 4.7: µ-XP spectra representing the relative photoelectron emission intensity of Rh and Ni from the metallic region of Rh(111)/Ni. Acquisition details are as in the previous image; the raw data was corrected with the transmission function of the analyzer, and Shirley backgrounds were subtracted. The integrated area is indicated. The nickel spectrum is the same as in figure 4.6 (b).

Assuming homogeneous distribution, the relative number of atoms, N_{Rh}/N_{Ni}, can be calculated according to [21].

$$\frac{I_{Rh3d}}{I_{Ni2p}} = \left(4.8 \pm 0.5\right) = \frac{I_{Rh3d}^{\infty} \cdot \left(N/V\right)_{Ni}^{\infty} \cdot \lambda_{Alloy, E'(Rh)} \cdot \lambda_{Ni, E'(Ni)}}{I_{Ni2p}^{\infty} \cdot \left(N/V\right)_{Rh}^{\infty} \cdot \lambda_{Alloy, E'(Ni)} \cdot \lambda_{Rh, E'(Rh)}} \cdot \frac{N_{Rh}}{N_{Ni}} \qquad (4\text{-}1)$$

The attenuation length $\lambda_{Me, E'(Me')}$ refers to photoelectrons emitted from a metal Me' at a kinetic energy E' traveling though a metal Me. Raw intensities are usually scaled to reference intensities I^{∞}, recorded from the pure metals (with atom densities $(N/V)^{\infty}$) under the same conditions. Those are not available, but the ratio can be substituted using a general expression for the intensity [22].

$$\frac{I_{Rh3d}^{\infty}}{I_{Ni2p}^{\infty}} = \frac{\chi_{Rh3d} \cdot \left(N/V\right)_{Rh}^{\infty} \cdot \lambda_{Rh, E'(Rh)}}{\chi_{Ni2p} \cdot \left(N/V\right)_{Ni}^{\infty} \cdot \lambda_{Ni, E'(Ni)}} \qquad (4\text{-}2)$$

For equation (4-2) it is assumed that the intensities are recorded under the same conditions and already corrected for the spectrometer transmission. χ is an angle-dependent subshell photoemission cross section. Substitution into equation (4-1) yields:

$$\frac{I_{Rh3d}}{I_{Ni2p}} = \left(4.8 \pm 0.5 \right) = \frac{\chi_{Rh3d} \cdot \lambda_{Rh,\,E'(Rh)}}{\chi_{Ni2p} \cdot \lambda_{Rh,\,E'(Ni)}} \cdot \frac{N_{Rh}}{N_{Ni}} \tag{4-3}$$

setting $\lambda_{Alloy,\,E'(Me')} = \lambda_{Rh,\,E'(Me')}$ since the bulk essentially consists of rhodium. Before evaluating equation (4-3) some parameters have to be calculated, starting with λ [23].

$$\lambda_{Me,\,E'(Me')} = 0.41 b_{Me}^{3/2} \cdot E'\left(Me' \right)^{1/2}$$
$$E'\left(Ni \right) = 130 \text{ eV} \Rightarrow \lambda_{Ni,\,E'(Ni)} = 0.48 \text{ nm}, \ \lambda_{Rh,\,E'(Ni)} = 0.55 \text{ nm} \tag{4-4}$$
$$E'\left(Rh \right) = 670 \text{ eV} \Rightarrow \lambda_{Ni,\,E'(Rh)} = 1.10 \text{ nm}, \ \lambda_{Rh,\,E'(Rh)} = 1.25 \text{ nm}$$

$$b_{Me} = \sqrt[3]{\frac{M_{Me}}{\rho_{Me} \cdot N_A}}; \ b_{Ni} = 0.22 \text{ nm}, \ b_{Rh} = 0.24 \text{ nm} \tag{4-5}$$

The quantity b_{Me} is an effective atom size for a metal, calculated from its density ρ and molar mass M, as done in equation (4-5), with values from [24]. The empirical formula (4-4) describes the so-called *universal curve* of attenuation lengths and requires input in nm and eV [23]. The cross sections χ can be calculated according to [25]:

$$\frac{\chi_{Rh3d}}{\chi_{Ni2p}} = \frac{\dfrac{\sigma_{Rh3d}}{4\pi} \cdot \left(1 + \dfrac{\beta_{Rh3d}}{2} \left(3\cos^2 \delta - 1 \right) \right)}{\dfrac{\sigma_{Ni2p}}{4\pi} \cdot \left(1 + \dfrac{\beta_{Ni2p}}{2} \left(3\cos^2 \delta - 1 \right) \right)}$$
$$= \frac{0.64 \cdot \left(1 + \dfrac{1.18}{2} \left(3\cos^2 16° - 1 \right) \right)}{0.87 \cdot \left(1 + \dfrac{1.09}{2} \left(3\cos^2 16° - 1 \right) \right)} = \frac{1.31}{1.71} \tag{5-6}$$

with σ representing the (angle independent) photoionization cross section, β the so-called asymmetry parameter (both taken from [25]), and δ the angle enclosed by the emission direction (surface normal) and the photon polarization vector. Putting the results from the equations (4-4) and (4-6) into (4-3) finally yields $N_{Rh}/N_{Ni} = 2.8 \pm 0.3$. The given error originates from the flawed Ni2p$_{3/2}$-spectrum alone, but further contributions might be introduced by the equations (5-4) – (5-6). Those are assumed to be small, since

consequently ratios were used and systematic errors probably cancel each other. But it has to be kept in mind that the applied XPS theory neglects elastic scattering effects. However, according to the calculation within the assumption of homogeneous distribution the ratio of rhodium and nickel atoms is ~3:1, i.e. the surface region of the Rh(111) sample contains about 25 % nickel.

Assuming that the complete amount of nickel is located on top of the surface, the coverage Θ_{Ni} can be calculated according to [23]:

$$\frac{I_{Rh}}{I_{Ni}} = \left(4.8 \pm 0.5\right) = \frac{I_{Rh}^{\infty}}{I_{Ni}^{\infty}} \cdot \frac{1 - \Theta_{Ni}\left(1 - \exp\left(-\frac{b_{Ni}}{\lambda_{Ni,\,E'(Rh)}} \cdot \cos\theta\right)\right)}{\Theta_{Ni}\left(1 - \exp\left(-\frac{b_{Ni}}{\lambda_{Ni,\,E'(Ni)}} \cdot \cos\theta\right)\right)} \tag{4-7}$$

The angle θ is enclosed by emission direction and surface normal and hence 0° (normal emission). All other parameters are available from the equations (4-4) – (4-6); equation (4-2) is calculated directly, taking the volume of elementary cells from [24]. Evaluation of equation (4-7) finally yields $\Theta_{Ni} = 0.8 \pm 0.1$ MLE, so the surface is covered to about 80 % since a pseudomorphic arrangement of atoms can be assumed [1].
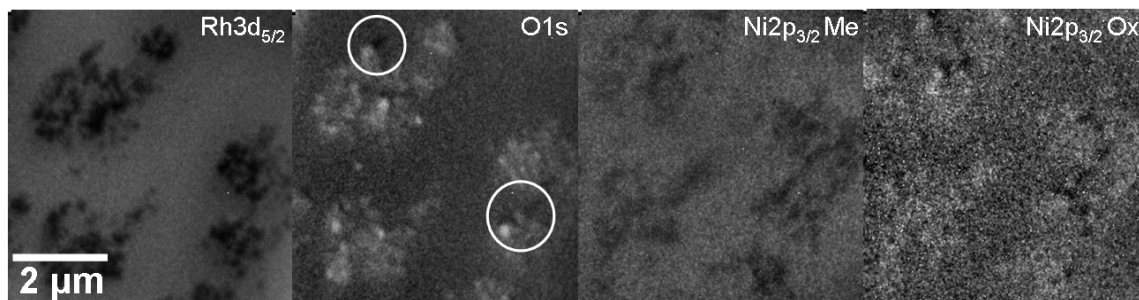
Figure 4.8: XPEEM images of the indicated photoelectron lines, recorded at $hv = 480$ eV (Rh), 655 eV (O), 982 eV (Ni). The surface was exposed to reaction conditions (502°C, ~$1 \cdot 10^{-6}$ mbar O_2, $7 \cdot 10^{-7}$ mbar H_2). In the O1s-image beam shadows are indicated; more are present in the Ni-Ox image.

The qualitative results of the μ-XPS data presented in figure 4.6 are confirmed by XPEEM imaging of the surface components in figure 4.8. Metallic nickel is enriched on regions with high rhodium intensity, and there are regions where the latter is screened by accumulations of oxidic nickel and oxygen (NiO). An interesting detail is revealed in the O1s image. The two circles are placed at positions where 3D-particles cast shadows by

screening the adjacent area from the photon beam. Knowing its incidence angle (16°), the particle height can be estimated from the length of the shadow; for the upper one ~100 nm are found. The assignment of the dark areas as shadows is regarded to be safe, since the $Ni2p_{3/2}$-Ox image exhibits many more, all pointing in the same direction. From the PEEM measurements (section 4.1) it is already assumed that the surface is covered with nickel oxide particles, which is proven here by XPEEM.

An interesting observation about the NiO particles is illustrated in figure 4.9. The micrographs depicted there are arranged in chronological order and originate from the same surface preparation with nickel. Apparently the size of the oxide particles depends on the applied conditions.
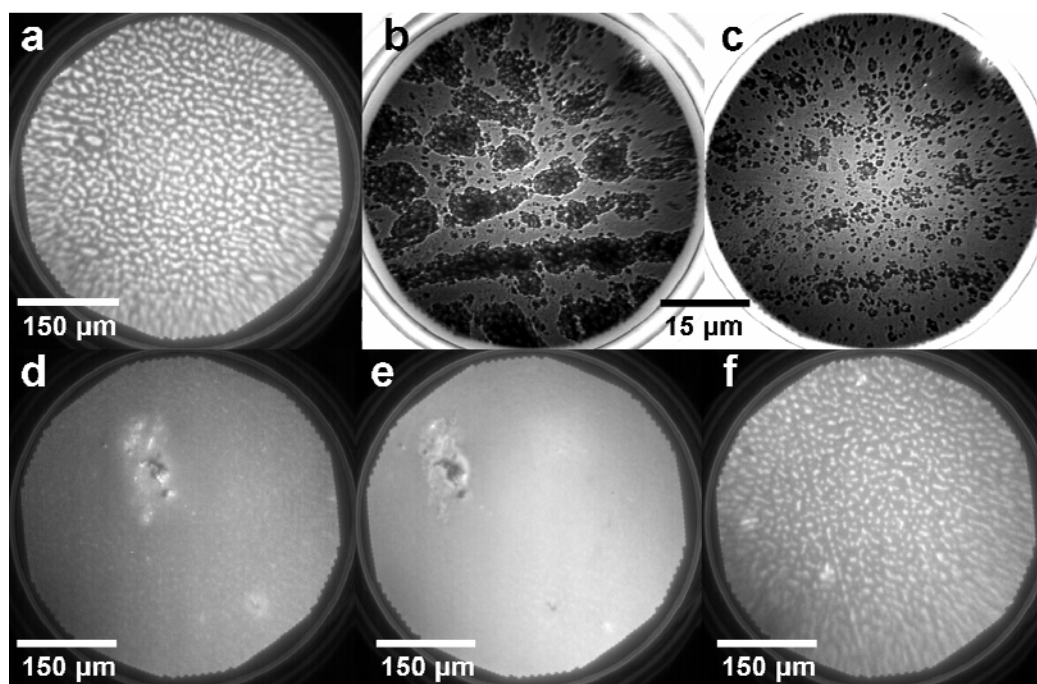
Figure 4.9: Chronological series of micrographs illustrating the evolution of NiO-particles under various conditions. (a) PEEM image of the surface exposed to the $H_2 + O_2$ reaction at 300°C, $3 \cdot 10^{-4}$ mbar. (b) MEM image (0.9 eV) after transport to *Elettra* and an oxidation treatment (500°C, $2 \cdot 10^{-5}$ mbar). (c) MEM image (1.3 eV) of the same area under reaction conditions (500°C, $\sim 10^{-6}$ mbar). (d) PEEM image after transportation back to Hannover and an oxidation treatment (500°C, $2 \cdot 10^{-5}$ mbar/30 min, $1 \cdot 10^{-6}$ mbar/70 min). (e) Same region under reaction conditions ($\sim 3 \cdot 10^{-6}$ mbar, 500°C). (f) 11 days later under reaction conditions, 500°C, $8 \cdot 10^{-5}$ mbar; reaction dynamics (pulses) are averaged out.

The PEEM image in figure 4.9 (a) shows a typical Rh(111)/Ni/NiO surface under $H_2 + O_2$ reaction conditions at high pressure, with a high density of large oxide particles (bright, several μm in size). Those were preserved during transportation trough air to

Italy, as shown in (b), though it looks like the large particles are agglomerates of smaller ones. Upon applying low-pressure reaction conditions ($\sim 10^{-6}$ mbar, 500°C) the large structures decomposed into smaller particles (c); higher densities of those were still visible at the former locations of the large particles. (d) and (e) show the surface back in the PEEM chamber; first under oxygen after an oxidation treatment (d) and then under reaction conditions at low pressure ($\sim 10^{-6}$ mbar, 500°C). Apart from the macroscopic defect (not of interest here) large structures were hardly visible. The large oxide agglomerates finally returned after exposing the sample to higher pressures, as visible in (f), at 500°C and $8 \cdot 10^{-5}$ mbar.

It is not clear if the formation of the large oxide agglomerates was caused by the reaction at high pressures, or by exposition to high pressures of oxygen alone at 500-600°C. However, the large structures were favored under the reaction conditions at high pressure (excitable regime), while at lower pressure (range of double metastability, see section 4.1) smaller NiO particles were formed.

Comparing the oxide particles in figure 4.9 (b) and (c), the amount of NiO present on the surface appears to be reduced; this is not necessarily true, though, because the particle height might have been different in both cases. The transition between the two states is illustrated in detail in figure 4.10. The change was induced by exposing the sample to excess hydrogen, where the oxide structures were barely visible. Returning to oxygen-rich conditions, the oxide distribution was changed drastically. It is concluded that with excess hydrogen the NiO particles were reduced, and grew again upon reoxidation, adapting to changed conditions. Apparently some nickel was transferred into the Rh(111)/Ni phase.

Having reached the NiO distribution shown in figure 4.9 (c), the system started to exhibit intensity oscillations in MEM, which it did not do before. One might speculate that in figure 4.9 (b) the nickel fraction in the Rh(111)/Ni phase was too small to allow oscillating behavior in the range of double metastability. The excitable behavior at high pressure and the double metastability at low pressure might require different Ni fractions in the surface region of the metallic phase. The different amount of NiO on the surface might simply be a consequence of that: the system adapts to different conditions by storing excess nickel in form of NiO particles on the surface. Whether that is true or not, the figures 4.9 and 4.10 demonstrate that the NiO particles are indirectly involved in the reaction dynamics.
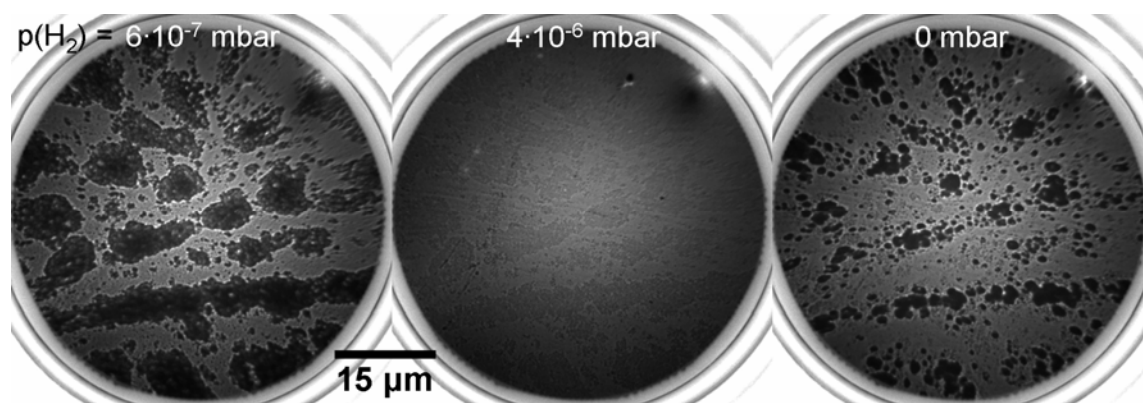
Figure 4.10: MEM images illustrating the reduction of NiO particles and their regeneration by oxidation at ~500°C and $p(O_2) \approx 1.5 \cdot 10^{-6}$ mbar. The reduction started at $p(H_2) = 2 \cdot 10^{-7}$ mbar. The first two images were recorded at 1.0 eV, the third one at 1.3 eV.

4.3 Nature of the chemical waves

The system Rh(111)/Ni/NiO supposedly exhibits double metastability exposed to the $H_2 + O_2$ reaction at pressures about 10^{-6} mbar and 500°C (see section 4.1, discussion of figure 4.3). In that case the surface is expected to alternate between an oxygen-rich and an oxygen-poor state, as confirmed with µ-XPS and shown in figure 4.11.
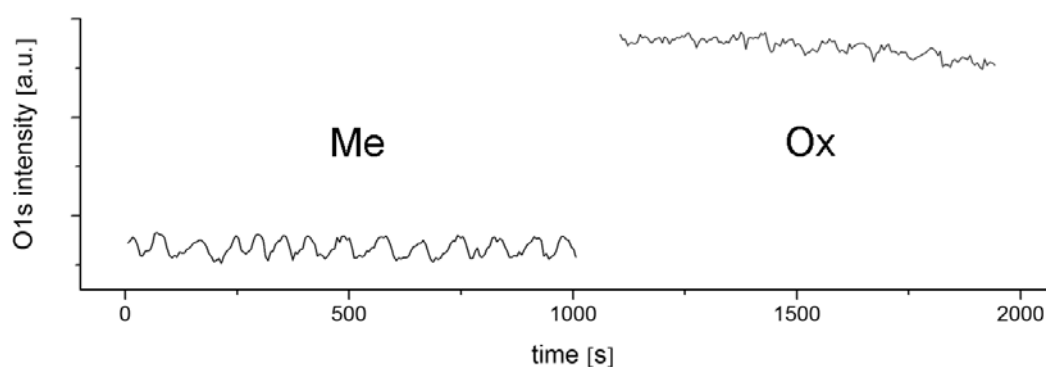
Figure 4.11: µ-XPS time series of the O1s intensity, recorded on the metallic and oxidic part of the surface with $hv = 655$ eV. The conditions are 502°C, ~$1 \cdot 10^{-6}$ mbar O_2 and $7 \cdot 10^{-7}$ mbar H_2; backgrounds had to be subtracted, since those oscillate due to the oscillating work function.

To monitor oscillations of the oxygen coverage, again small areas are selected which are oxide-covered or -free, respectively (as in figure 4.6). The metallic area has a smaller O1s signal (see figure 4.6 (d)), exhibiting clear oscillations. The period is about 70 s and appears somehow irregular, which is supposedly due to adjusting the partial

pressures directly before 0 s; the system is not yet synchronized. The amplitude is rather small: evaluating the peak areas corresponding to a maximum and a minimum, variation of about 10 % of the maximum intensity is found. The O1s binding energy remains constant at 530 eV during a period.

The O1s signal of the NiO-covered area also exhibits a small modulation, which is supposedly caused by an uncovered fraction of the selected area. The continuous decay of the intensity is due to a slow beam-damage effect on the NiO particles, which can also be observed in LEEM.

The excitable regime could not be investigated with XPS or LEEM because the required pressures ($> 10^{-5}$) exceed the instrumental limits; all information currently available is presented in section 4.1 (figures 4.1 – 4.3). A model for the excitation mechanism is proposed in figure 4.12. It is based on a couple of considerations and some findings from this and other studies:

- Nickel is a more electropositive metal than rhodium and thus has a higher affinity to oxygen.

- Nickel migrates from the surface into the bulk of Rh(111) at elevated temperatures [1]. This behavior is apparently changed by the presence of oxygen, as after many hours of reaction experiments nickel is still present at the surface.

- Oxygen adsorbed on Rh(111) exerts a site-blocking effect, inhibiting hydrogen adsorption [26].

- The oscillating surface cycles trough four different states (see figure 4.3 (a)).

- The reaction dynamics is located on the metallic part of the surface; at constant conditions the NiO particles are probably just obstacles for pulse propagation (see figures 4.1, 4.2, 4.13). They are hence treated as inactive.

Starting with an oxygen-covered surface featuring mostly Rh atoms in the topmost layer (top left, figure 4.12), hydrogen adsorption and thus water formation are inhibited. Due to the presence of O_{ad} diffusing Ni atoms are trapped at the surface (segregation), forming some kind of mixed adlayer. It is assumed that the incorporation of nickel into the topmost layer lifts the site blocking effect of O_{ad}. In the next step the adlayer is hence reduced by hydrogen, yielding water which desorbs immediately, leaving metallic nickel on top of the surface. Proceeding in the sequence, the nickel atoms migrate beneath the

topmost layer and leave a rhodium surface. Completing the cycle, oxygen can readsorb to form again the initial state, an O-covered rhodium surface.

In terms of an activator-inhibitor model (see figure 1.2) O_{ad} is regarded as the activator, since a high surface concentration can build up quickly, which, in turn, causes the surface concentration Ni to increase slowly via segregation. Nickel is the inhibitor, which facilitates the activator O_{ad} to be removed from the surface. Here, the terms "activator" and "inhibitor" point out the role of the corresponding species in the excitation mechanism, and not their effect on the actual reaction rate, which is vice versa.
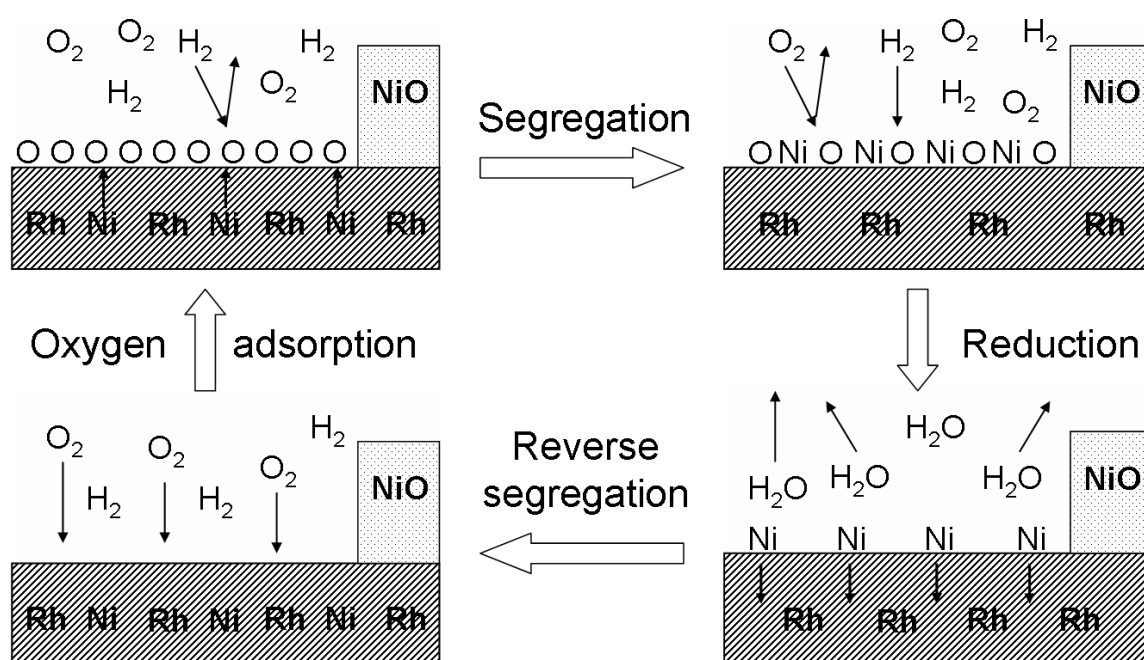
Figure 4.12: Sketch of a proposed excitation mechanism, based on reversible nickel segregation/anti-segregation, driven by oxygen adsorption.

The proposed mechanism is hypothetical in large parts, but matches with the observed behavior and known facts noted above. It is similar to classical oscillation mechanisms of surface reactions, where often a reversible surface reconstruction plays the key role of modulating sticking coefficients [27]. This is attributed here to the reversible incorporation of nickel into the topmost layer.

A mixed nickel-oxygen adlayer is of crucial importance for the model. As possible candidates, (2×1) and (6×1) Ni−O monolayer structures were observed on the (111)-terraces of Rh(15 15 13) [28]. The chemical nature of such adlayers is, however, unclear. Considering the high affinity of nickel towards oxygen, a 2-dimensional oxide

is likely, possibly similar to one of the open, and hence reactive structures known from Rh(111)/VO$_x$ (see section 3.1).

Considering the mixed Ni−O adlayer (figure 4.12, top left) as a 2-dimensional oxide, the water formation mechanism would be different from the Langmuir-Hinshelwood scheme (see section 1.2). One could rather speak of a Mars-van Krevelen mechanism. This term describes the reaction of an adsorbate with a part of the crystal lattice of the catalyst [29], in this case with the oxide ions of the 2-dimensional Ni−O lattice. The involvement of a reversible oxide formation/reduction step in an oscillation mechanism was already proposed for several systems, but experimental proof was only provided at high pressures (> 10^{-3} mbar) [27, 30].

In order to explain the chemical wave propagation, lateral diffusion of mobile adsorbates has to be added to the scheme in figure 4.12 (see section 1.3). Diffusion is actually observed in the experiment: oxide particles can act as diffusion barriers, as shown in figure 4.13.
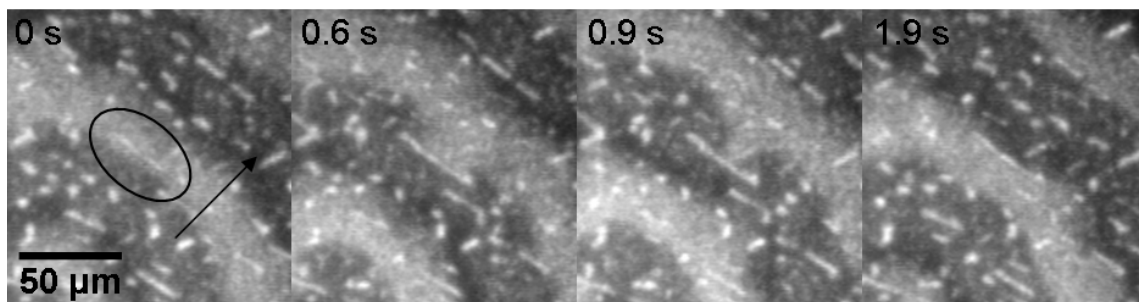
Figure 4.13: Series of PEEM images illustrating that NiO particles act as diffusion barriers on pulse propagation. Conditions: 400°C, p(O$_2$) = 2·10^{-4} mbar, p(H$_2$) ≈ 2·10^{-4} mbar. The NiO "wall"-particle is encircled; the arrow indicates the pulse propagation direction.

Observing the pulse propagation in PEEM, one usually gets the impression that the pulses bypass the NiO particles without interaction. In contrast to that, it is expected that even inert particles perturb the propagation by blocking lateral diffusion. To observe such interactions, one has to look at a special situation, as in figure 4.13. The rather low temperature of 400°C slows down diffusion, and one large, elongated particle (encircled) is aligned perpendicularly to the propagation direction. This "wall"-particle is apparently large enough to temporarily screen the area behind from being covered with a species causing a dark PEEM appearance. The dark area (high work function) is thus associated with a laterally diffusing species; O$_{ad}$ is a likely candidate.

4.4 Summary

The composite surface Rh(111)/Ni/NiO exhibits various self-organization phenomena when exposed to the $H_2 + O_2$ reaction at temperatures between 400 and 600°C and pressures in the $10^{-7} - 10^{-4}$ mbar range.

Nickel and rhodium form a surface alloy decorated with NiO particles. The size distribution of these particles, and probably also the nickel fraction bound as NiO, varies with the total pressure. At high pressures ($> 10^{-5}$ mbar) large particles or agglomerates are favored, partially in form of rods up to 30 μm long. At lower pressures smaller particles and agglomerates are formed (tens of nm up to few μm), the highest being about 100 nm tall. Supposedly much less nickel is bound in the small oxide particles at low pressure. The experiments suggest that the NiO on top of the surface might act as a dynamic nickel storage capacity, allowing the surface alloy to adjust its Ni-content to particular reaction conditions.

The Rh(111)/Ni surface alloy exhibits periodic pulse propagation at high pressures ($> 10^{-5}$ mbar). Observation of rotating spiral waves, target patterns and irregular pulses is reported, with velocities between 40 and 60 μm/s and periods between 1 and 15 s. Frequency differences under constant conditions indicate excitable rather than oscillatory behavior. During one excitation period the surface cycles trough four different states whose chemical nature still needs to be determined. It is shown that one laterally diffusing species, possibly O_{ad}, is accumulated in a state with high work function. A hypothetic excitation mechanism is proposed, based on periodic nickel segregation and formation/reduction of a mixed Ni−O monolayer. To the authors knowledge, it is reported here for the first time that an originally bistable system can be converted into an excitable one by addition of an element, i.e. by alloying.

Also at lower pressures ($< 10^{-5}$ mbar) periodic propagation of chemical waves occurs. The velocity is similar to higher pressures, but periods (> 40 s) and hence wavelengths (several mm) are much longer. The surface cycles between only two different states, which is associated with rate oscillations. The rate oscillations are explained by different reactivities of the two states and the macroscopic dimensions of the chemical waves. The dynamic behavior is tentatively assigned to double metastability [2]. As expected, the oxygen coverage varies during the oscillations on the metallic part of the surface, while the NiO particles are essentially unaffected. Assuming a homogeneous Rh/Ni distribution in the surface region, the nickel fraction of the alloy

under reaction conditions is about 25 %; this is supposedly more than at higher pressures, when some nickel is transferred onto the surface to be stored as NiO.

4.5 References

[1]   A. Wander, C. J. Barnes, L. D. Mapledoram, D. A. King, *Structural transitions in ultra-thin nickel films on Rh(111)*, Surf. Sci. 281 (1993), 42.

[2]   R. Imbihl, *Oscillatory Reactions on Single Crystal Surfaces*, Prog. Surf. Sci. 44 (1993), 185.

[3]   S. Nettesheim, A. von Oertzen, H. H. Rotermund, G. Ertl, *Reaction diffusion patterns in the catalytic CO-oxidation on Pt(110): Front propagation and spiral waves*, J. Chem. Phys. 98 (1993), 9977.

[4]   M. Falcke, M. Bär, H. Engel, M. Eiswirth, *Traveling waves in the CO oxidation on Pt(110): Theory*, J. Chern. Phys. 97 (1992), 4555.

[5]   T. Smolinsky, *Ratenoszillationen und Musterbildung bei der $H_2 + O_2$ -Reaktion auf dem bimetallischen Katalysator Rh(111)/Ni*, Diploma Thesis, Hannover 2010.

[6]   H. Marbach, S. Günther, T. Neubrand, R. Imbihl, *Mass transport of alkali metal with pulses: catalytic NO reduction with hydrogen on Rh(1 1 0)/K*, Chem. Phys. Lett. 395 (2004), 64.

[7]   P. R. Norton, R. L. Tapping, J. W. Goodale, *A Photoemission Study of the Interaction of Ni(100), (110) and (111) Surfaces with Oxygen*, Surf. Sci. 65 (1977), 13.

[8]   S. Hüfner, G. K. Wertheim J. H. Wernick, *XPS Core Line Asymmetries in Metals*, Solid State Commun. 17 (1975), 417.

[9]   K. S. Kim, R. E. Davis, *Electron Spectroscopy of the Nickel-Oxygen System*, J. Electron Spectrosc. Relat. Phenom. 1 (1972), 251.

[10]   K. S. Kim, N. Winograd, *X-ray Photoelectron Spectroscopic Studies of Nickel-Oxygen Surfaces using Oxygen and Argon Ion-Bombardment*, Surf. Sci. 43 (1974), 625.

[11]   A. P. Grosvenor, M. C. Biesinger, R. S. C. Smart, N. S. McIntyre, *New interpretations of XPS spectra of nickel metal and oxides*, Surf. Sci. 600 (2006), 1771.

[12]   A. J. Jaworowski, A. Beutler, F. Strisland, R. Nyholm, B. Setlik, D. Heskett, J. N. Andersen, *Adsorption sites in O and CO coadsorption phases on Rh(111) investigated by high-resolution core-level photoemission*, Surf. Sci. 431 (1999), 33.

[13]   J. Schoiswohl, F. Mittendorfer, S. Surnev, M. G. Ramsey, J. N. Andersen, F. P. Netzer, *Chemical Reactivity of Ni-Rh Nanowires*, Phys. Rev. Lett. 97 (2006), 126102.

[14]   S. Uhlenbrock, C. Scharfschwerdt, M. Neumann, G Illing, H.-J. Freund, *The influence of defects on the Ni 2p and 0 1s XPS of NiO*, J. Phys.: Condens. Matter 4 (1992), 7973.

[15]   M. Oku, H. Tokuda, K. Hirokawa, *Final States after Ni2p Photoemission in the Nickel-Oxygen System*, J. Electron Spectrosc. Relat. Phenom. 53 (1991), 201.

[16]   M. A. van Veenendaal, G. A. Sawatzky, *Nonlocal Screening Effects in 2p X-Ray Photoemission Spectroscopy Core Level Line Shapes of Transition Metal Compounds*, Phys. Rev. Lett. 70 (1993), 2459.

[17]   L. Soriano, I. Preda, A. Gutiérrez, S. Palacín, M. Abbate, A. Vollmer, *Surface effects in the Ni 2p x-ray photoemission spectra of NiO*, Phys. Rev. B 75 (2007), 233417.

[18]   G. Tyuliev, M. Sokolova, *Temperature dependence of Ni^{3+} quantity in the surface layer of NiO*, Appl. Surf. Sci. 52 (1991), 343.

[19]   S. Le Bihan, M. Figlarz, *Involution Thermique d-un Hydroxyde de Nickel Lamelaire mal Organize avec des Molécules d'Eau en Insertion entre les Feuillets; Comparisation avec l'Hydroxide de Nickel Cristallizé $Ni(OH)_2$*, Thermochim. Acta 6 (1973), 319.

[20]   W. Levason, C. A. McAuliffe, *Higher Oxidation State Chemistry of Iron, Cobalt and Nickel*, Coordinat. Chem. Rev. 12 (1974), 151.

[21]   G. Ertl, J. Küppers, *Low Energy Electrons and Surface Chemistry*, VCH, Weinheim 1985.

[22]   A. Jablonski, *Quantification of surface-sensitive electron spectroscopies*, Surf. Sci. 603 (2009), 1342.

[23]   D. Briggs, M. P. Seah, *Practical Surface Analysis*, John Wiley & Sons Ltd, Chichester 1994.

[24]   N. W. Ashcroft, N. D. Mermin, *Festkörperpysik*, Oldenbourg, München 2005.

[25]   J. J. Yeh, I. Lindau, *Atomic Subshell Photoionization Cross Sections and Asymmetry Parameters: $1 \le Z \le 103$*, At. Data Nucl. Data Tables 32 (1985), 1.

[26]   A. Schaak, R. Imbihl, *Bistability and formation of low work function areas in the $O_2 + H_2$ reaction on a Rh(111) surface*, J. Chem. Phys. 113 (2001), 9822.

[27]   R. Imbihl, *Nonlinear dynamics on catalytic surfaces*, Catal. Today 105 (2005), 206.

[28]   G. Parteder, F. Allegretti, M. Wagner, M. G. Ramsey, S. Surnev, F. P. Netzer, *Growth and Oxidation of Ni Nanostructures on Stepped Rh Surfaces*, J. Phys. Chem. C 112 (2008), 19272.

[29]   C. Doornkamp, V. Ponec, *The universal character of the Mars and Van Krevelen mechanism*, J. Mol. Catal. A: Chem. 162 (2000), 19.

[30]   N. Hartmann, R. Imbihl and W. Vogel, *Experimental evidence for an oxidation/reduction mechanism in rate oscillations of catalytic CO oxidation on Pt / SiO_2*, Catal. Lett. 28 (1994), 373.

5. Synopsis

In this study it was investigated how the addition of oxides affects the $H_2 + O_2$ reaction on Rh(111). The oxides of vanadium and nickel were deposited in small amounts on the substrate, constituting two different inverted model catalyst systems. Those shall be compared in the following, concluding this thesis.

Vanadium can easily switch between different oxidation states. This is the main reason why vanadium oxides find applications as versatile oxidic catalysts themselves. Significant catalytic activity of thick VO_x films was not found in this study, though, probably due to low-pressure conditions. The activity of sub-monolayer VO_x films is small, compared to the rhodium support. Vanadium always exists as an oxide under reaction conditions, i.e. in presence of oxygen reduction of to the metallic state was not found, regardless of high hydrogen excess. Oxygen acts as an anchor, preventing alloy formation and keeping the vanadium on top of the surface.

That is completely different with nickel as second component. Nickel oxide particles on the surface maintain oxidation state +2 under oxygen-rich conditions, but with hydrogen in excess NiO is reduced to metallic nickel. The latter forms a surface alloy with the substrate; under not too reductive reaction conditions the nickel is partially located on top of the surface in form of oxide particles, and partially in the surface region, alloyed with the rhodium support.

Oxide redistribution under reaction conditions occurs in both systems, in case of VO_x exclusively lateral. In an oxygen atmosphere vanadium usually exists in form of V^{5+}-oxide nanoscale islands; adding hydrogen causes reduction to V^{3+}-oxide, which condenses into mesoscopic stripe patterns surrounded by essentially bare Rh(111). These patterns coarsen with time by a coalescence mechanism. Two driving forces are presumably responsible for condensation and coarsening: the chemical affinity of vanadium and oxygen, as required for reactive phase separation, and minimization of the phase boundary energy.

In contrast to vanadium, nickel migrates predominantly normal to the surface. At high partial pressures of hydrogen 3-dimensional NiO particles are reduced to metallic nickel, which alloys with the rhodium support at least partially; upon returning to more

oxidative conditions nickel is drawn back onto the surface, forming NiO particles again. The size of those particles, and probably also the amount of nickel contained therein varies, depending on the total pressure at the time of formation.

The reaction dynamics on the Rh(111)/VO$_x$ catalyst remains basically unchanged on the surface areas not covered by the oxide. As on pure Rh(111) the reaction is bistable: in the active stationary state an essentially adsorbate-free rhodium surface catalyses the reaction at a constant rate.

If the rhodium catalyst is modified by nickel on the other hand, metallic Ni is directly incorporated in the Rh(111) surface. This changes the reaction dynamics drastically. Instead of the stationary states of a bistable system, formation of chemical wave patterns and rate oscillations are observed.

Self-organized material distribution phenomena on composite catalyst surfaces are now known to occur with very different materials added onto a substrate. Reactive phase separation was observed on Rh(110) for such different additional components as alkali metals or gold, with electronegativities of < 1 or 2.4, respectively. In the present work typical d-band metals with medium values of 1.6 (V) and 1.9 (Ni) are shown to get redistributed on Rh(111) under $H_2 + O_2$ reaction conditions. With vanadium, (quasi-) stationary, 2-dimensional patterns of VO$_x$ are formed, while in the case of nickel 3-dimensional oxide particles probably play a role of a dynamic Ni storage capacity, allowing the alloy support to adjust its nickel content to particular reaction conditions.

It is pure coincidence that in all examples rhodium substrates were used. There is no apparent reason why rhodium should be predisposed for such material redistribution phenomena. The basic requirement to the substrate is simply that its chemical affinity to oxygen (in case of the $H_2 + O_2$ reaction) differs from that of the added component. Hence it would be interesting to investigate different substrates in future studies, and to utilize chemical affinities to adsorbates other than oxygen.

The most promising perspective to continue the present work lies in the "inversion" of the inverted model catalyst system, although oxide-supported noble metal catalysts have already been studied intensively. Redistribution of thin noble metal films on oxidic substrates by a chemical reaction might be feasible for selected systems. This would open up a pathway to tailor efficient supported catalysts for other reactions which do not affect the morphology. Noble metal redistribution on oxides could be studied on

metallic substrates that allow growing thin, smooth oxide films on the surface. Sub-monolayer amounts of noble metals would be deposited on top, and methods like PEEM or LEEM could be conveniently applied to study redistribution under reaction conditions. The experience gained for $Rh(111)/VO_x$ and the $H_2 + O_2$ reaction provides a suitable starting point for such investigations.

Acknowledgements

Curriculum Vitae

Personal

Name:	Florian Lovis
Nationality:	German
Birth:	27.09.1978 in Bremen
Residence:	Hannover

School

1985−1989	Ludwig-Ralfs-Schule Düshorn
1989−1991	OS Walsrode
1991−1998	Gymnasium Walsrode, graduation with Abitur
1998−1999	Community service in the hospital Walsrode

Academics

1999−2005	Studies in chemistry at the Freie Universität Berlin, graduation with diploma
2005−2010	Doctoral course of studies at the Gottfried Willhelm Leibniz Universität Hannover
2005−2008	Support by the state of Niedersachsen with a scholarship, within the program *New materials with tailored properties*
End of 2008	Three month as visiting scientist in Trieste/Italy at the *Instituto Nazionale per la Fisica della Materia (INFM)*

Publications

F. Lovis, M. Hesse, R. Imbihl, *Redistribution of Supported Vanadium Oxide Catalysts by Pattern Formation*, Catal. Lett. 136 (2010), 171.

M. Rafti, F. Lovis, Y. Zheng, R. Imbihl, *Homogeneous and front-induced surface transformations during catalytic oxidation of ammonia over Pt(100)*, Chem. Phys. Lett. 446 (2007), 323.

Erklärung zur Dissertation

gemäß §6(1) der Promotionsordnung der Naturwissenschaftlichen Fakultät der Gottfried Wilhelm Leibniz Universität Hannover für die Promotion zum Dr. rer. nat.

Hierdurch erkläre ich, dass ich die vorliegende Dissertation selbständig verfasst und die benutzten Hilfsmittel und Quellen sowie gegebenenfalls die zu Hilfeleistungen herangezogenen Institutionen vollständig angegeben habe.

Die Dissertation wurde nicht schon als Masterarbeit, Diplomarbeit oder andere Prüfungsarbeit verwendet.